STRUCTURAL CHARACTERIZATION OF RARE-

EARTH DOPED SODA MAGNESIA ALUMINA

SILICA GLASSES FOR HOLOGRAPHIC

STORAGE: BRILLOUIN, RAMAN
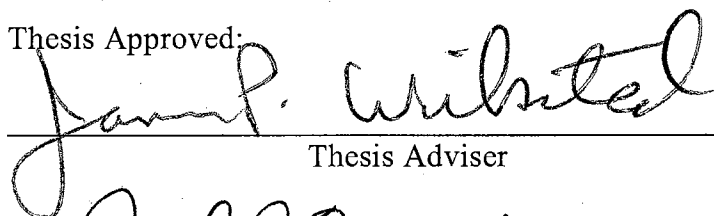
AND NMR SPECTROSCOPY

STUDIES

By

ZHANDOS UTEGULOV

Bachelor of Science
Kazakh National University
Almaty, Kazakhstan
1996

Master of Science
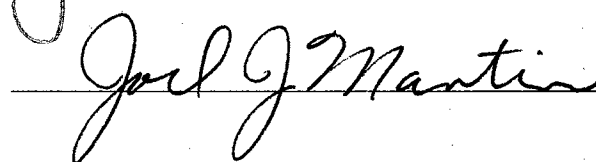Oklahoma State University,
Stillwater, Oklahoma
1999

Submitted to the Faculty of the
Graduate College of the
Oklahoma State University
in partial fulfillment of
the requirements for
the Degree of
DOCTOR OF PHILOSOPHY
August, 2003

STRUCTURAL CHARACTERIZATION OF RARE-

EARTH DOPED SODA MAGNESIA ALUMINA

SILICA GLASSES FOR HOLOGRAPHIC

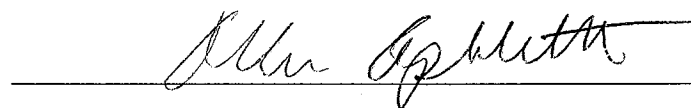STORAGE: BRILLOUIN, RAMAN

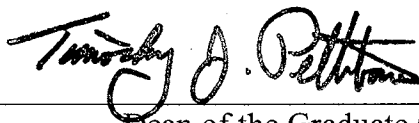AND NMR SPECTROSCOPY

STUDIES

Thesis Approved:

_____
Thesis Adviser

_____

_____

_____

_____
Dean of the Graduate College

ii

ACKNOWLEDGMENTS

This is rather important section in this work and I want to express my deep and sincere thanks to my research mentor Dr. James Wicksted for his advice, constructive guidance, inspiration and support throughout this research project and study. I want to acknowledge Dr. George Dixon, Dr. Abdulatif Hamad, Dr. Margaret Eastman and Dr. Paul Shen for their fruitful scientific discussions and great assistance in the lab. I also wish to thank Dr. Albert Rosenberger, Dr. Joel Martin and Dr. Allen Apblett for serving in my dissertation committee. My sincere appreciation goes to Dr. Westhaus and many other OSU faculty, staff, postdoctoral scientists and fellow graduate students for their help, cooperation, wise advice, constructive criticism and sincere friendship.

TABLE OF CONTENT

LIST OF TABLES

LIST OF FIGURES

NOMENCLATURE

EDSMAS glass	europium doped soda magnesia alumina silica glass
NBO	non-bridging oxygen
BO	bridging oxygen
BLS	Brillouin light scattering
RLS	Raman light scattering
NMR	Nuclear magnetic resonance
MAS	magic angle ($\beta = 54.74°$) spinning
FWM	four-wave mixing
C_{11}	compressional modulus
C_{44}	shear modulus
E	Young modulus
B	adiabatic bulk modulus
σ	Poisson ratio
LA	longitudinal acoustic
TA	transverse acoustic
P_{12}	photoelastic constant for LA wave
P_{44}	photoelastic constant for TA wave
ppm	parts per million
$Q^n(m\text{Al})$	SiO_4 tetrahedron with ($n = 1 - 4$) number of bridging oxygens and ($m = 1 - 4$) number of neighboring AlO_4 tetrahedra
cm^{-1}	wave-number, a unit of energy equal to 0.12399 meV and corresponding to the frequency of 29.979 GHz

CHAPTER I

INTRODUCTION

Glass has a number of structural and practical advantages over crystalline materials, including excellent homogeneity, variety of form and size and the potential for doping with a variety of dopant materials, which makes the glass medium excellent for photonic applications. Rare-earth doped aluminosilicate glasses have been shown to be great candidates for holographic storage medium [1-9], new room temperature hole-burning materials [10], strong visible light luminescence materials [11], Faraday rotators [12, 13], infrared window materials [14] and radiation delivery vehicles in human body [15, 16], etc. Besides, aluminosilicate melts are the most important constituents of Earth magmas [17], so the knowledge of the structure of aluminosilicate melts and glasses for geological applications is important as well. Many characterization techniques, such as Brillouin light spectroscopy (BLS) [18], Raman light spectroscopy (RLS) [2, 19], solid-state nuclear magnetic resonance (NMR) [19, 20-22], ionic conductivity measurement [6, 7, 23], absorption spectroscopy [24,25], Mossbauer spectroscopy [26] etc., have been utilized to study the structure of rare-earth doped oxide glasses. In general these glass materials show interesting properties, such as high elastic moduli [27] and large paramagnetic susceptibilities [28]. However, a detailed understanding of the optical properties and atomic structures in rare-earth doped glass is still unclear because amorphous materials do not have long range order and the environment of atoms and ions is not well defined.

Laser-induced persistent and transient refractive index gratings in Eu^{3+} silicate, phosphate and germinate glasses have been previously reported [1-7]. Rare-earth

activated silicate glasses with stable photorefractive gratings have recently been realized as the materials for holographic media [3, 8]. The great stability of the persistent gratings in these glasses makes them competitive candidates for optical demultiplexers, filters and ROM-memories. There is also great potential for forming these glass-based materials as integrated fiber optic devices.

The optical technique used to form the gratings is called the non-degenerate four-wave mixing (FWM). Its nature is in nonlinear mixing of two laser "write" beams and laser "read" beam to produce a fourth "signal" beam. This effect can be treated theoretically as a third order nonlinear optical process or, alternatively as Bragg scattering from a laser induced refractive index grating. The experimental setup involves crossing of two Ar^+ write laser beams in the sample (Fig. 1) at $2\theta_\omega$ crossing angle to form a constructive interference pattern in the form of sine wave [6]. The light intensity in the peak regions of the pattern modulates the complex refractive index of the material compared to its value in the valley regions of the pattern. This creates a laser induced refractive index pattern. A probe (or read) He-Ne laser beam passing through the sample in the presence of a refractive index grating is diffracted by the grating at θ_r angle between the diffracted direction and the normal to the plane of the glass sample. By measuring the properties of the diffracted (signal) beam using a photo multiplier tube (PMT), all of the information about the physical properties of the grating can be determined.

Laser-induced changes in the refractive index are used to create superimposed transient population gratings and permanent structural gratings in Eu^{3+}-doped soda magnesium aluminosilicate (EDSMAS) glasses [6,7]. The grating strengths in these
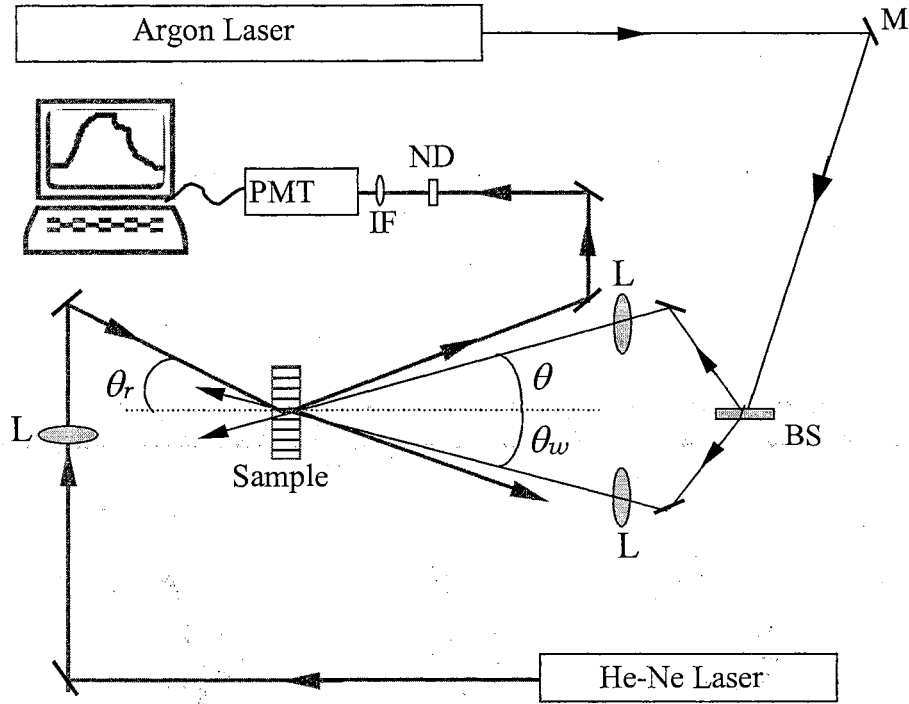
Fig.1. FWM experimental setup (Courtesy of A. Hamad).

glasses were improved by optimization of the composition and processing parameters.

It was found that the change in nonlinear index of refraction Δn (the signature of the

FWM signal strength) in these glasses was proportional to the number of the high

energy phonons [1,29], the population of the excited Eu^{3+} ions [7] and Al atoms

present in the glass [6]. The results of this work in the form of dependence of

permanent change in the nonlinear index of refraction Δn versus different individual

components: Eu_2O_3 and Al_2O_3 in EDSMAS glasses are presented on Fig.2 and Fig.3,

respectively. The write and read beam laser powers (wavelengths) (waist) were kept

at 30 mW (465.8 nm) (70 μm) and 3.5 mW (632.8 nm) (95 μm), respectively, and the

crossing angle was fixed at 5.0°. During FWM experiment, Eu^{3+} ions of EDSMAS

glass are excited by the laser write beam to the $^5D_2$ energy level. Radiationless

relaxation from this excited state to the $^5D_0$ metastable level causes the multi-phonon

emission, i.e. several high energy vibrational excitations (phonons) on the order of 1000 cm^{-1} (Fig. 4).
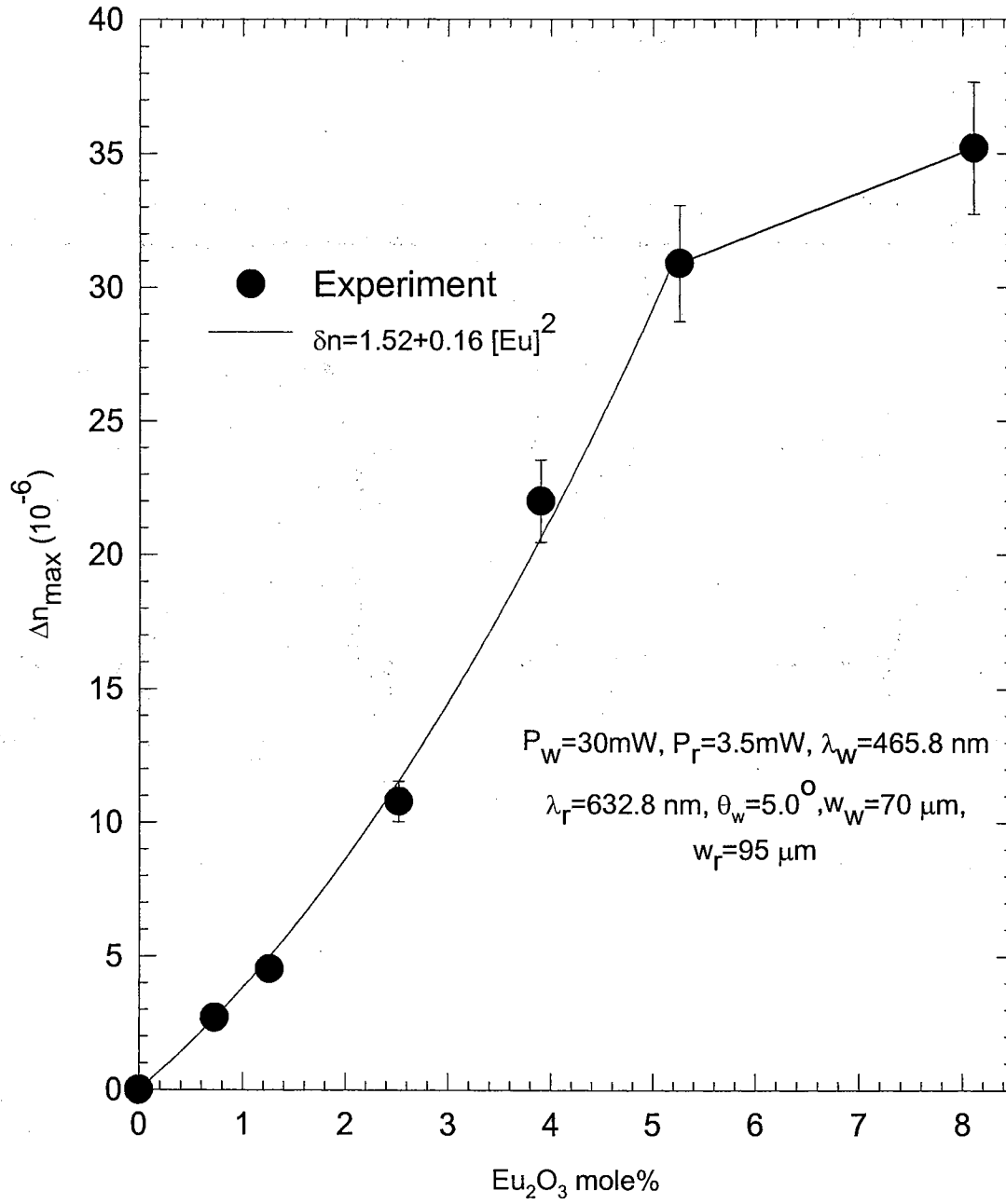
Fig. 2.   FWM strength signal in EDSMAS glasses vs. Eu_2O_3 mole%.

Data is taken from Ref. 7.
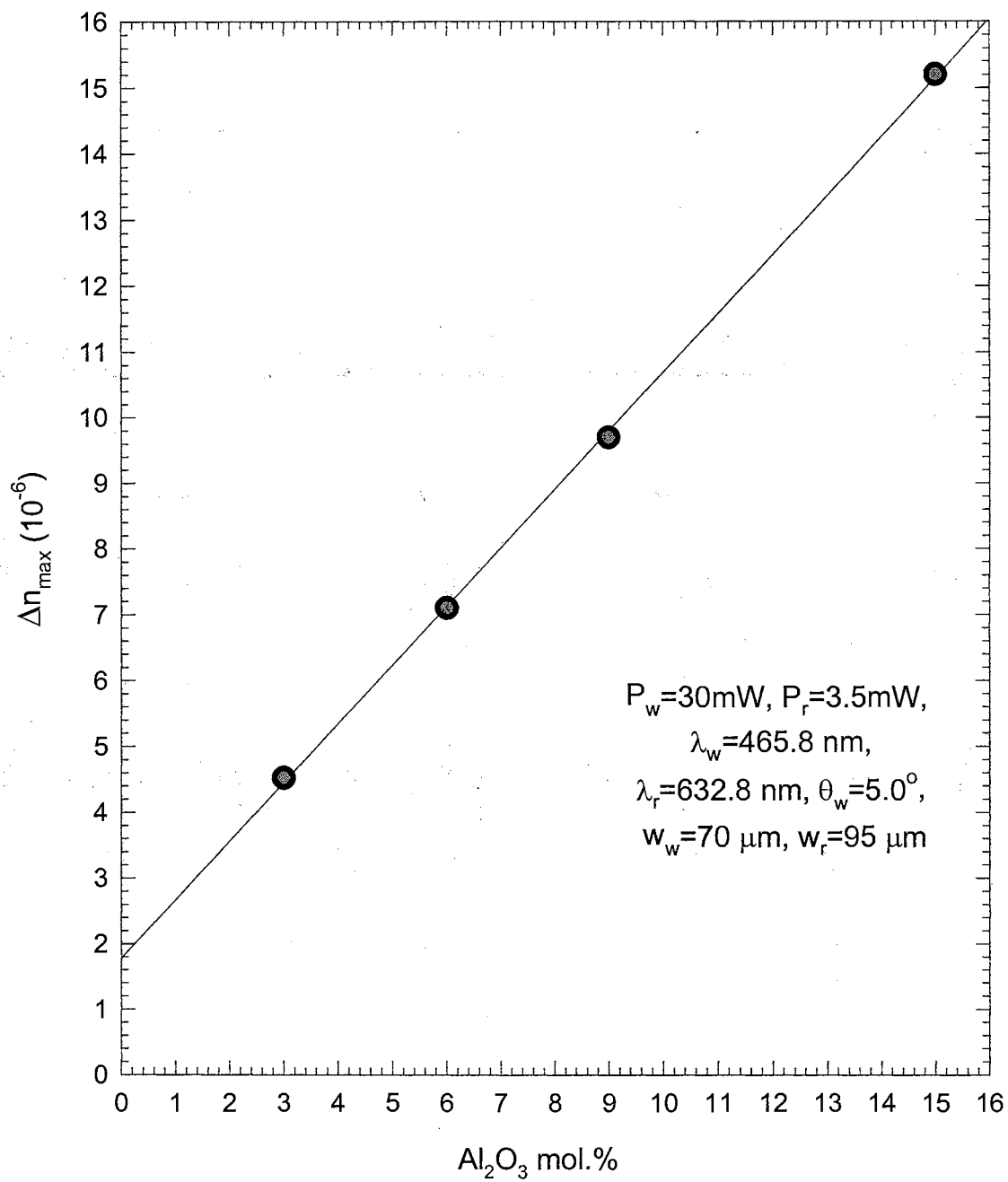
Fig. 3. FWM strength signal in EDSMAS glasses vs. Al_2O_3 mole %.

Data is taken from Ref [6].
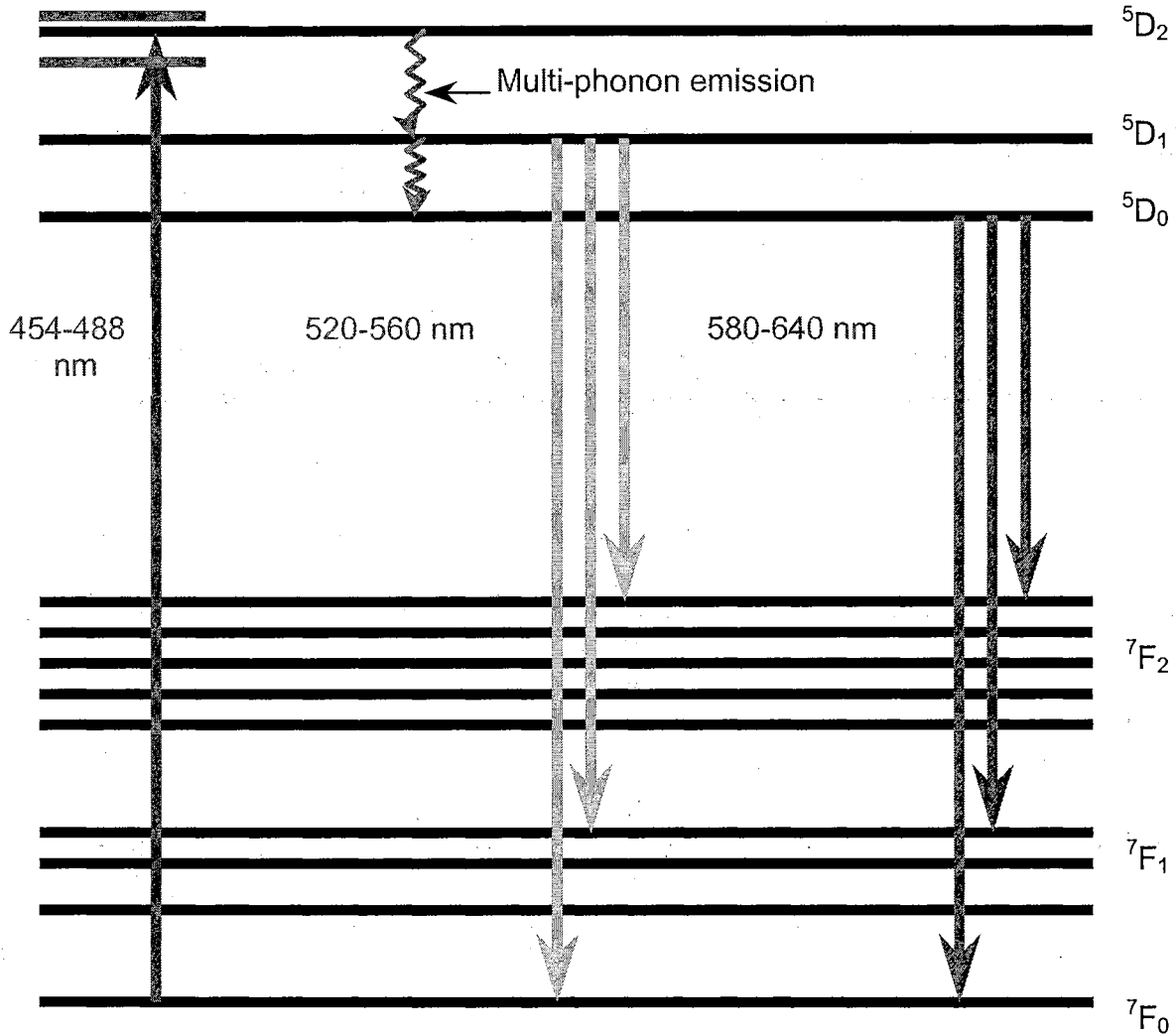
Fig. 4. Eu^{3+} energy level diagram

This produces local structural changes leaving the Eu^{3+} ions in a different configuration having a different index of refraction [1]. In this sense, the role of high energy phonons (~ 1000 cm^{-1}) is believed to be crucial, since they fill the energy gap between the excited level and metastable $^5D_1$ as well as $^5D_0$ levels and provide the activation energy for some light modifiers to migrate in the glass network during FWM experiments. Thus, the permanent grating is formed due to the migration of light modifiers (e.g. Na^+ and Mg^{2+}) from the bright towards the dark regions of the

grating. G.S. Dixon and co-workers [9] attributed the kinetics of the persistent gratings in rare-earth doped silicate glasses by the long range diffusion of small modifiers mediated by the hot-phonon field resulting from non-radiative decay of the rare-earth sensitizers. They suggested that the photorefractive efficiencies of these glasses might be improved through the increase of weakly bound modifiers or by the introduction of larger modifiers that tend to stretch the glass network.

Earlier investigations of aluminosilicate glasses were limited to the structure of either glasses containing trivalent modifier ions [20-22, 27, 30, 31] or glasses containing divalent and/or monovalent ions only [32-35]. The structure of Eu^{3+} doped soda magnesia alumina silica (EDSMAS) glass is expected to be more complicated than that of binary, ternary and quaternary glasses. The 2-dimensional schematics of EDSMAS system is shown in Fig.5. In the present dissertation we used Brillouin light scattering (BLS), Raman light scattering (RLS) and solid-state nuclear magnetic resonance (NMR) spectroscopies to study the structure of EDSMAS glasses, i.e. aluminosilicate disordered materials containing trivalent modifier (Eu^{3+}) ions, divalent (Mg^{2+}), and monovalent (Na^+) ions. Using RLS, we investigated the local structure of the glass by probing high-, mid- and low- frequency optical phonons. ^{27}Al, ^{29}Si and ^{23}Na NMR spectroscopies will be used to provide information about Al, Si and Na^+ coordination sites, respectively. The disappearance of the NMR signals with increasing Eu content will be shown for ^{27}Al and ^{29}Si. The ultimate goal of this comprehensive characterization study is to better understand the physical nature of holographic grating formation in EDSMAS glasses Conclusions as well as recommendations on improving holographic grating formation in these materials
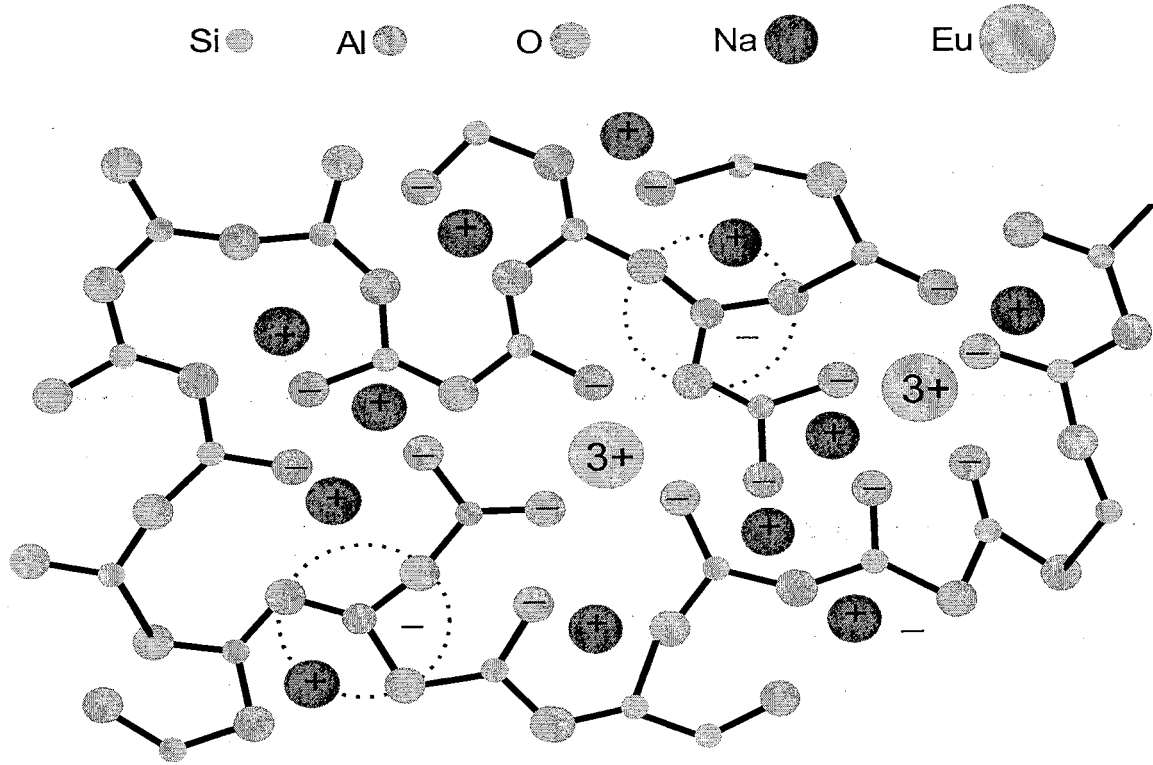
Fig. 5. Two-dimensional schematic of EDSMAS glass.

versus concentration changes of different individual components (Eu_2O_3, Al_2O_3 and Na_2O) in EDSMAS glasses were presented. The composition of these three glass families of Eu-, Al and Na- series under study are given in Table 1. In the estimation of the relative NBO amounts given in Table 1 it was assumed that Na^+, Mg^{2+} and Eu^{3+} ions in EDSMAS glass create one, two and three NBOs, respectively, and one Na^+ ion is needed to compensate the charge of one $[AlO_4]^-$ complex [36]. With the help of BLS we will research elastic and photoelastic properties of these non-crystalline materials and will discuss the implications of these studies on improvement of FWM signal. The photoelastic (or elasto-optic) effect, being the coupling of the index of refraction to the mechanical strain in the material [37], plays an important role in a

number of optical devices such as acousto-optic modulators [38], photo-optical switches, opto-optical deflectors etc. The mechanical strain can be introduced in a number of ways. It can be permanently frozen-in at the time of formation of the glass or it can be caused by the acoustic phonons propagating in the material which are induced by a transducer or laser light.

Sample ID	Eu_2O_3	MgO	Na_2O	SiO_2	Al_2O_3	R_{Na+Mg}	R_{Eu}	R_{Total} NBO
Eu0	0.00	12.00	15.00	70.00	3.00	0.273	0	0.273
Eu0.73	0.73	11.91	14.89	69.49	2.98	0.269	0.025	0.294
Eu1.26	1.26	11.85	14.81	69.12	2.96	0.267	0.043	0.310
Eu3.90	3.90	11.53	14.42	67.27	2.88	0.255	0.130	0.385
Eu5.26	5.26	11.37	14.21	66.32	2.84	0.249	0.173	0.422
Eu8.11	8.11	11.03	13.78	64.32	2.76	0.237	0.262	0.499

Table 1. The EDSMAS glasses composition (in mole %) of (a) Eu-series with the fraction of NBOs due to: Na^+ and Mg^{2+} (R_{Na+Mg}), rare earth ions (R_{Eu}) and the total number of modifier ions ($R_{Total\ NBO}$);

Sample ID	Al_2O_3	SiO_2	MgO	Eu_2O_3	Na_2O	$R_{Total\ NBO}$
Al 0	0	72.08	11.85	1.26	14.81	0.348
Al 2.96	2.96	69.12	11.85	1.26	14.81	0.310
Al 5.92	5.92	66.16	11.85	1.26	14.81	0.271
Al 8.88	8.88	63.20	11.85	1.26	14.81	0.235
Al14.81	14.81	57.27	11.85	1.26	14.81	0.165

(b) Al-series with the fraction of NBOs ($R_{Total\ NBO}$)

Sample ID	Na_2O	SiO_2	MgO	Eu_2O_3	Al_2O_3	$R_{Total\ NBO}$
Na9.86	9.86	73.12	11.85	1.26	2.96	0.247
Na14.81	14.81	69.12	11.85	1.26	2.96	0.310
Na19.73	19.73	64.20	11.85	1.26	2.96	0.375
Na24.67	24.67	59.26	11.85	1.26	2.96	0.456

(c) Na-series with the fraction of NBOs ($R_{Total\ NBO}$)

CHAPTER II

THEORY

2.1. BRILLOUIN LIGHT SCATTERING (BLS)

BLS being the physical process of light scattering by the propagating fluctuations in the dielectric constant of the material was first predicted by Leon Brillouin [39] who suggested that light should be inelastically scattered by the acoustic (Debye) modes of insulating media. Mandelshtamm independently predicted the same effect in 1926. Among the techniques used for testing of variety of materials, optical methods such as BLS and RLS play an important role since they are non-destructive. The most significant advantage of BLS over ultrasonic techniques is that it requires only very small samples and that it is mechanically non-contacting. BLS can be simply imagined as the diffraction of the incident light by the "gratings" formed by the sound waves (acoustic phonons). These gratings are moving with the speed of sound, causing the scattered light to be Doppler shifted.

The principle of light scattering can be described by either a classical or quantum mechanical point of view. Generally, BLS is produced by the creation (Stokes event) or annihilation (anti-Stokes event) of a phonon as indicated in Fig. 6. An incident photon of wavevector $\vec{k_i}$ and frequency ω_i is scattered with wavevector $\vec{k_S}$ and frequency ω_S during the interaction a phonon of wavevector $\vec{q}$ and frequency ω_B (also known as Brillouin shift) created or annihilated. In case of no phonon involvement we deal with Rayleigh (elastic) scattering. Typically, Brillouin shifts ω_B are on the order of $1 \mathrm{cm}^{-1}$ or smaller. It is generally accepted that the BLS is due to propagating fluctuations in the

dielectric constant of the material under study, while the Rayleigh scattering is due to existence of non-propagating diffusive fluctuations.

(a)

Phonon creation (Stokes event)

(b)

Phonon annihilation (anti-Stokes event)
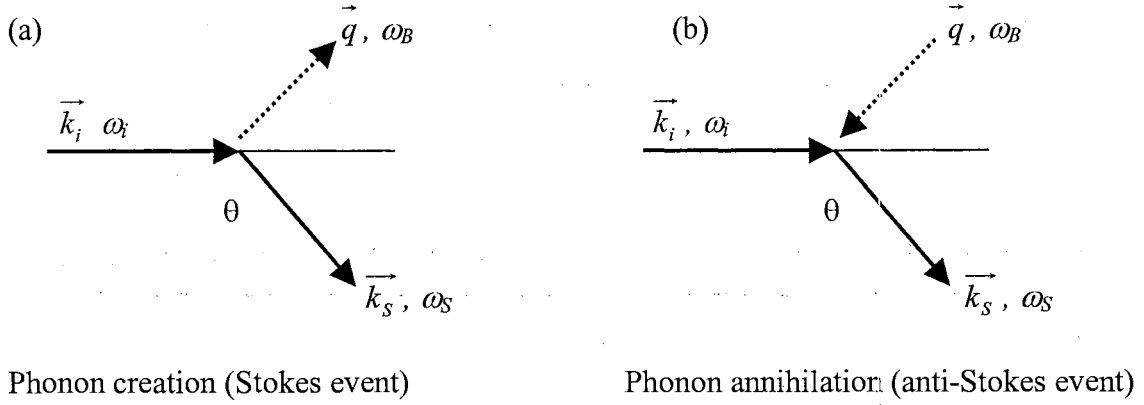
Figure 6. Stokes and anti-Stokes events of BLS

The conservation of energy and momentum requires:

$$\omega_s = \omega_i \pm \omega_B \qquad (2.1.1a)$$

$$\vec{k_s} = \vec{k_i} \pm \vec{q} \qquad (2.1.1b)$$

Since the energies of acoustic phonons is small compared to the energies of the incident and scattered lights, i.e. $\omega_B \approx 10^{10} Hz \ll \omega_i(\omega_s) \approx 10^{14} Hz$, then $|\vec{k_s}| = |\vec{k_i}|$ and a light scattering experiment selects those modes for which

$$q = 2n|\vec{k_i}|\,sin(\theta/2) \qquad (2.1.2)$$

where θ and n are the scattering angle and the refractive index of the scattering medium, respectively. Sound velocity will be defined combining (2.1.1) and (2.1.2.) as follows:

$$V = \frac{\omega_B}{q} = \frac{\omega_B}{2n|\vec{k_i}|\sin\left(\dfrac{\theta}{2}\right)} = \frac{\omega_B \lambda_i}{4\pi n \sin\left(\dfrac{\theta}{2}\right)} \qquad (2.1.3)$$

12

where ω_B is the Brillouin shift in cm^{-1} units to be measured by BLS experiment. Typical value for the sound velocity is $V \sim 10^5$ cm/s.

Crystal lattice dynamics can be analyzed using the familiar harmonic approximation. The stress is given by:

$$S_{ik} = C_{iklm} \frac{\partial u_m}{\partial x_l} \qquad (2.1.4)$$

where C_{iklm} is the elastic stiffness tensor. The equation of motion in harmonic approximation is:

$$\rho \frac{\partial^2 u_i}{\partial t^2} = \frac{\partial S_{ik}}{\partial x_k} = C_{iklm} \frac{\partial^2 u_m}{\partial x_k \partial x_l} \qquad (2.1.5)$$

Here ρ is the density, u is the displacement vector and x is the location of the equilibrium point that is being displaced

Assuming the plane-wave solution:

$$u_m = u_m^0 e^{i(\vec{q}\,\vec{r} - \omega t)} \qquad (2.1.6)$$

Substituting (2.1.6) into (2.1.5) we have

$$\rho \omega^2 u_i^0 = C_{iklm} q_k q_l u_m^0 \qquad (2.1.7)$$

For the long wavelength acoustic modes $\omega_B = Vq$, where V is the appropriate sound velocity. Thus, $\sum_{kl} \left[C_{iklm} \hat{q}_k \hat{q}_l - \rho V^2 \delta_{im} \right] u_m^0 = 0 \qquad (2.1.8)$

where $\hat{q}_k = \frac{q_k}{|q|}$ is the k-component of unit vector $\hat{q}$. Equation (2.1.8) has non-trivial solutions only if the secular determinant vanishes. The number of non-zero elastic constants depends on the symmetry of the material. Elasticity is a centrosymmetric property. This means that if the reference axes are transformed by the operation of a

center of symmetry the C_{ijkl} components remain unaltered. From this, for isotropic medium like glass, the form of the elastic constant $\left(C_{mn}\right)$ matrix is given by [37]:

$$\left(C_{mn}\right) = \begin{pmatrix} C_{11} & C_{12} & C_{12} & 0 & 0 & 0 \\ C_{12} & C_{11} & C_{12} & 0 & 0 & 0 \\ C_{12} & C_{12} & C_{11} & 0 & 0 & 0 \\ 0 & 0 & 0 & \frac{1}{2}(C_{11} - C_{12}) & 0 & 0 \\ 0 & 0 & 0 & 0 & \frac{1}{2}(C_{11} - C_{12}) & 0 \\ 0 & 0 & 0 & 0 & 0 & \frac{1}{2}(C_{11} - C_{12}) \end{pmatrix} \quad (2.1.9)$$

Thus, glasses, being isotropic media, as a result of the stress produced by a small strain can be described by just two independent elastic constants C_{11} and C_{44}. The third elastic constant is related to the first two through the Cauchy relation $C_{12} = C_{11} - 2C_{44}$ [40]. Using (2.1.9) and if $\hat{q}$ is propagating along an arbitrary $\hat{q} = [1,0,0]$ direction, then in six-component notation equation (2.1.8) results in the following eigenvalues and eigenvectors:

$$(\rho V^2)_1 = \rho V_L^2 = C_{11}, \qquad \hat{u} = (1,0,0) \qquad\qquad\qquad (2.1.10a)$$

$$(\rho V^2)_2 = \rho V_T^2 = C_{44}, \qquad \hat{u} = (0,1,0) \text{ and } (0,0,1) \qquad\qquad (2.1.10b)$$

Where $\hat{u}$ is the unit vector of the displacement direction (oscillation) and $\hat{q}$ is the direction of sound wave propagation. The first solution corresponds to the pure *longitudinal* acoustic mode and the second solution corresponds to one degenerate pure *transverse* acoustic modes. Thus, the typical Brillouin spectrum of glass consists of two sets of doublets symmetrically shifted from the incident frequency. They are longitudinal and transverse modes. The longitudinal BLS (corresponding to vibrations of $\hat{u}$ parallel to the sound wave vector $\hat{q}$) has been explained by adiabatic pressure fluctuations

propagating as a longitudinal (*compressional*) sound wave [41]. It corresponds to light scattering with the same polarization as the incident light. The transverse BLS (corresponding to vibrations $\hat{u}$ perpendicular to the sound wave vector $\hat{q}$) is related to the existence of anisotropic fluctuations associated with transverse (*shear*) deformation [42]. It contributes to the depolarized scattered light, i.e. light scattered with a change of polarization with respect to the incident light. The observed Brillouin splitting can simply be related to the sound velocity of the particular mode responsible for the scattering and the widths of the shifted lines are related to acoustic attenuation (phonon lifetimes) [43]. With $V_q = 6 \times 10^5$ cm/sec and $\omega_B = 0.8$ cm^{-1} the wavelength of the acoustic phonon vibrations is about 2000 Å, which is much larger than inter-atomic distance (~ 1Å). Therefore, BLS probes the scattering medium as a continuous one.

The elastic constants for the longitudinal (C_{11}) and transverse (C_{44}) acoustic waves can be determined from Brillouin shifts directly using (2.1.3) and (2.1.10) by

$$C_{11} = \rho V_L^2 = \frac{\rho \omega_L^2 \lambda_i^2}{4n^2 \sin^2\left(\dfrac{\theta}{2}\right)} \qquad (2.1.11a)$$

$$C_{44} = \rho V_T^2 = \frac{\rho \omega_T^2 \lambda_i^2}{4n^2 \sin^2\left(\dfrac{\theta}{2}\right)} \qquad (2.1.11b)$$

Some other important elastic parameters characterizing the strength of materials such as the Young modulus (E), Poisson's ratio (σ), and adiabatic bulk modulus (B) based on the elastic constants, can be calculated as follows [40]:

$$E = \frac{C_{44}(3C_{11} - 4C_{44})}{(C_{11} - C_{44})} \qquad (2.1.12a)$$

15

$$B = C_{11} - \frac{4}{3}C_{44}$$

(2.1.12b)

$$\sigma = \frac{C_{11} - 2C_{44}}{2(C_{11} - C_{44})}$$

(2.1.12c)

The intensity of the Brillouin peak is another important parameter in BLS spectroscopy and is related to the Rayleigh ratio, i.e. flux scattered into a unit solid angle per unit volume per unit incident light intensity. To obtain the Rayleigh ratio, we need to consider a propagating sound wave in the material. This wave produces a local strain in the material which in turn perturbs the local dielectric constant ε by an increment $\delta\varepsilon$. This perturbation will induce an additional polarization $\delta P = E_0 \delta\varepsilon / 4\pi$ due to a plane monochromatic wave traversing through the medium, and will scatter light at shifted frequencies corresponding to the acoustic modes. For incident light polarized in the j-th direction and scattered light polarized in the i-th direction, the Rayleigh ratio, or differential cross-section per unit volume of the glass, is defined as

$$R_{ij} = \frac{r^2 I_s^i}{\Delta\Omega \cdot \Lambda I_i^j} = \frac{r^2 I_s^i}{\Delta\Omega \cdot LP_i^j}$$

(2.1.13)

where r^2 is the squared distance from the scattering volume to the detector, Λ is the scattering volume from which light is being collected, $\Delta\Omega$ is the solid angle (in the air) at which the scattered volume is collected, I_s and I_i are the scattering and incident intensities, respectively. Since in laser scattering experiments the scattering volume almost always has the form of a thin column, it is frequently more useful to replace ΛI_i^j by LP_i^j where P_i^j is the measurable incident power and L is the length of the scattering column from which light is being collected. The relation between the change in the

reciprocal dielectric constant $\Delta\ (\epsilon^{-1})_{ij}$ and induced local strain tensor x_{kl} is governed by the

photoelastic constants (Pockel's coefficients) p_{ijkl} through the following linear relation:

$$\Delta\ (\epsilon^{-1})_{ij} = \sum_{kl} p_{ijkl} x_{kl} \qquad\qquad (2.1.14)$$

If we assume that the excitation of each acoustic mode is on an average in thermal

equilibrium at temperature T, then the Rayleigh ratio is given as follows [44]:

$$R^j = \frac{k_B T \omega_s^4}{32\pi^2 c^4 \rho V_j^2} \left[\hat{e}_s \bullet \vec{T}^j \bullet \hat{e}_i \right]^2 \frac{n_s}{n_i} \qquad\qquad (2.1.15)$$

where ω_s is the frequency of the scattered light, V_j is the velocity of the j_{th} acoustic mode,

$\hat{e}_s$ and $\hat{e}_i$ are the polarizations directions of the scattered and incident light, $\vec{T}_j$ is the

Brillouin tensor for the j_{th} direction. The factor $\left[\hat{e}_s \cdot \vec{T}^j \cdot \hat{e}_i \right]$ defines polarization selection

rules and allows one to determine which *photoelastic constants* are contributing to the

spectra under study; n_s and n_i define the refraction indices of the propagation of scattered

and incident light, respectively. For isotropic glasses, these two quantities are identical.

Equation (2.1.13) gives the scattering cross section for each acoustic mode in terms of the

$\vec{T}$ - tensors. Cummins and Schoen [44] tabulated Brillouin tensors according to phonon

propagation for numerous crystal classes including an isotropic glass. The geometry of

right-angle Brillouin scattering along with the formation of Bragg grating by sound

waves in the glass are depicted in fig. 7. For this case the eigenvalues (sound velocities

V), eigenvectors (displacement $\hat{u}$ -vectors) defined by (2.1.10) along with Brillouin $\vec{T}$ -

tensors for acoustic phonon propagation in x-direction ($q = (1,0,0)$) are given in Table 2.

For the sake of convenience, one can assign vertical (V) and horizontal (H) polarizations

for propagating light.
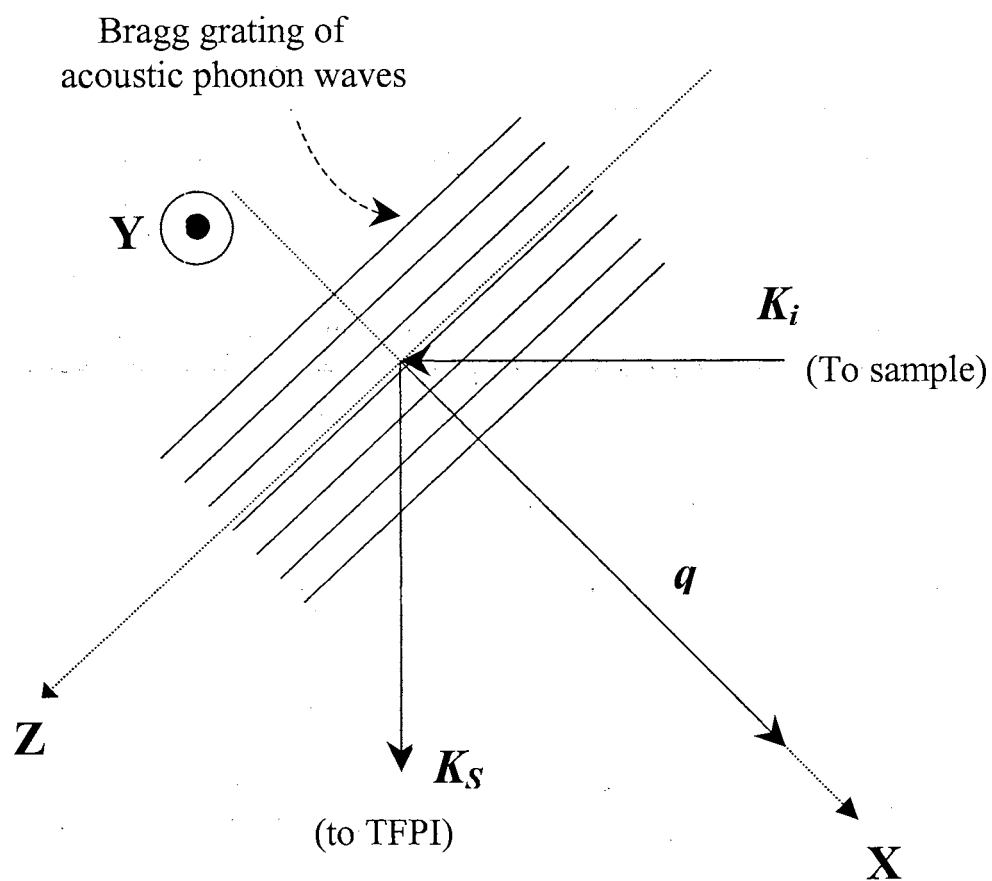
Fig.7. Right-angle BLS along with the formation of Bragg grating by sound waves in the

glass. Scattering light is monitored by TFPI.

$$\rho V^2 = C_{11}$$

$$\hat{u} = (1,0,0) \quad \text{Longitudinal}$$

$$\bar{\bar{T}} = \varepsilon^2 \begin{pmatrix} P_{11} & 0 & 0 \\ 0 & P_{12} & 0 \\ 0 & 0 & P_{12} \end{pmatrix}$$

$$\rho V^2 = \frac{1}{2}(C_{11} - C_{12}) = C_{44}$$

$$\hat{u} = (0,1,0) \quad \text{Transverse}$$

$$\bar{\bar{T}} = \varepsilon^2 \begin{pmatrix} 0 & \frac{1}{2}(P_{11} - P_{12}) & 0 \\ \frac{1}{2}(P_{11} - P_{12}) & 0 & 0 \\ 0 & 0 & 0 \end{pmatrix}$$

$$\rho V^2 = \frac{1}{2}(C_{11} - C_{12}) = C_{44}$$

$$\hat{u} = (0,0,1) \quad \text{Transverse}$$

$$\bar{\bar{T}} = \varepsilon^2 \begin{pmatrix} 0 & 0 & \frac{1}{2}(P_{11} - P_{12}) \\ 0 & 0 & 0 \\ \frac{1}{2}(P_{11} - P_{12}) & 0 & 0 \end{pmatrix}$$

Table 2. Acoustic phonon velocities, polarizations and BLS tensors for glasses

19

Therefore, for the incident and scattered light there are total of four possible polarization directions. Assuming that vertical polarization is in y-direction and horizontal polarization is in xz - plane, then we have for vertically polarized incident light $\hat{e}_i = \begin{pmatrix} 0 \\ 1 \\ 0 \end{pmatrix}$,

horizontally polarized incident light $\hat{e}_i = \dfrac{1}{\sqrt{2}} \begin{pmatrix} 1 \\ 0 \\ 1 \end{pmatrix}$, vertically polarized scattered light

$\hat{e}_s = (010)$ and horizontally polarized scattered light $\hat{e}_s = \dfrac{1}{\sqrt{2}}(10\bar{1})$.

The four combinations of polarization for incident and scattered light yield the following values for $\left[\hat{e}_s \cdot \vec{T}^j \cdot \hat{e}_i\right]$:

$$\underline{VV}:\ (0 \quad 1 \quad 0)\varepsilon^2 \begin{pmatrix} P_{11} & 0 & 0 \\ 0 & P_{12} & 0 \\ 0 & 0 & P_{12} \end{pmatrix} \begin{pmatrix} 0 \\ 1 \\ 0 \end{pmatrix} = \varepsilon^2 P_{12}$$

$$\underline{HH}:\ (1 \quad 0 \quad \bar{1})\frac{1}{\sqrt{2}}\varepsilon^2 \begin{pmatrix} P_{11} & 0 & 0 \\ 0 & P_{12} & 0 \\ 0 & 0 & P_{12} \end{pmatrix} \frac{1}{\sqrt{2}}\begin{pmatrix} 1 \\ 0 \\ 1 \end{pmatrix} = \frac{1}{2}\varepsilon^2(P_{11}-P_{12}) = \frac{1}{2}\varepsilon^2 P_{44} \qquad (2.1.16)$$

$$\underline{VH}:\ (1 \quad 0 \quad \bar{1})\frac{1}{\sqrt{2}}\varepsilon^2 \begin{pmatrix} 0 & \frac{1}{2}(P_{11}-P_{12}) & 0 \\ \frac{1}{2}(P_{11}-P_{12}) & 0 & 0 \\ 0 & 0 & 0 \end{pmatrix} \begin{pmatrix} 0 \\ 1 \\ 0 \end{pmatrix} = \frac{\varepsilon^2}{2\sqrt{2}}(P_{11}-P_{12}) = \frac{1}{\sqrt{2}}\varepsilon^2 P_{44}$$

$$\underline{HV}:\ (0 \quad 1 \quad 0)\frac{\varepsilon^2}{\sqrt{2}} \begin{pmatrix} 0 & \frac{1}{2}(P_{11}-P_{12}) & 0 \\ \frac{1}{2}(P_{11}-P_{12}) & 0 & 0 \\ 0 & 0 & 0 \end{pmatrix} \begin{pmatrix} 1 \\ 0 \\ 1 \end{pmatrix} = \frac{\varepsilon^2}{2\sqrt{2}}(P_{11}-P_{12}) = \frac{1}{\sqrt{2}}\varepsilon^2 P_{44}$$

Using a polarization rotator mounted to the laser head we can set the direction of the incident polarization (V or H) while the analyzer placed before the Fabry-Perot Interferometer selects V- or H-polarization for the Brillouin scattered light. In this way we can make sure that all four polarization arrangements listed in (2.1.16) are verifiable experimentally. We used BLS from the Eu1.26 glass sample and checked that within relative units of the Brillouin intensities we would match the resultant spectrum to the theoretical results of Equation (2.1.16). The results are shown in Fig 8. It is seen that VV and HH polarizations represents pure longitudinal acoustic phonons, while VH and HV polarizations define pure transverse acoustic phonons. Mixed $VV+VH$ and $HV+HH$ polarizations in Figs. 8 and Fig. 9 represent the superposition of VV plus VH modes, and HV plus HH modes, respectively. Under ideal experimental conditions VH and HV spectra are expected to be identical.

Substituting the polarization selection $\left[\hat{e}_s \cdot \vec{T}^j \cdot \hat{e}_i\right]$-values from (2.1.16) into the Rayleigh ratio (2.1.15), taking into account Eq. (2.1.11), right angle scattering geometry ($\theta = 90°$), $\omega_s \approx \omega_i$, $\varepsilon = n^2$, transmission factor of $\dfrac{16n^2}{(n+1)^2}$ due to normal incidence of the laser beam on a sample of finite thickness having two parallel surfaces, effective solid angle $\dfrac{\Delta\Omega}{n^2}$ correction inside the medium [45, 46], we will get the following relations for the absorption-free integrated Brillouin scattering intensities (2.1.13):

$$I_{VV} = \frac{\Delta\Omega}{r^2} P_i L_{eff} \left(\frac{\omega_i}{c}\right)^6 \frac{k_B T}{\pi^2} \frac{n^{10}}{\rho\omega_L^2 (n+1)^4} P_{12}^2 \qquad (2.1.17a)$$

21
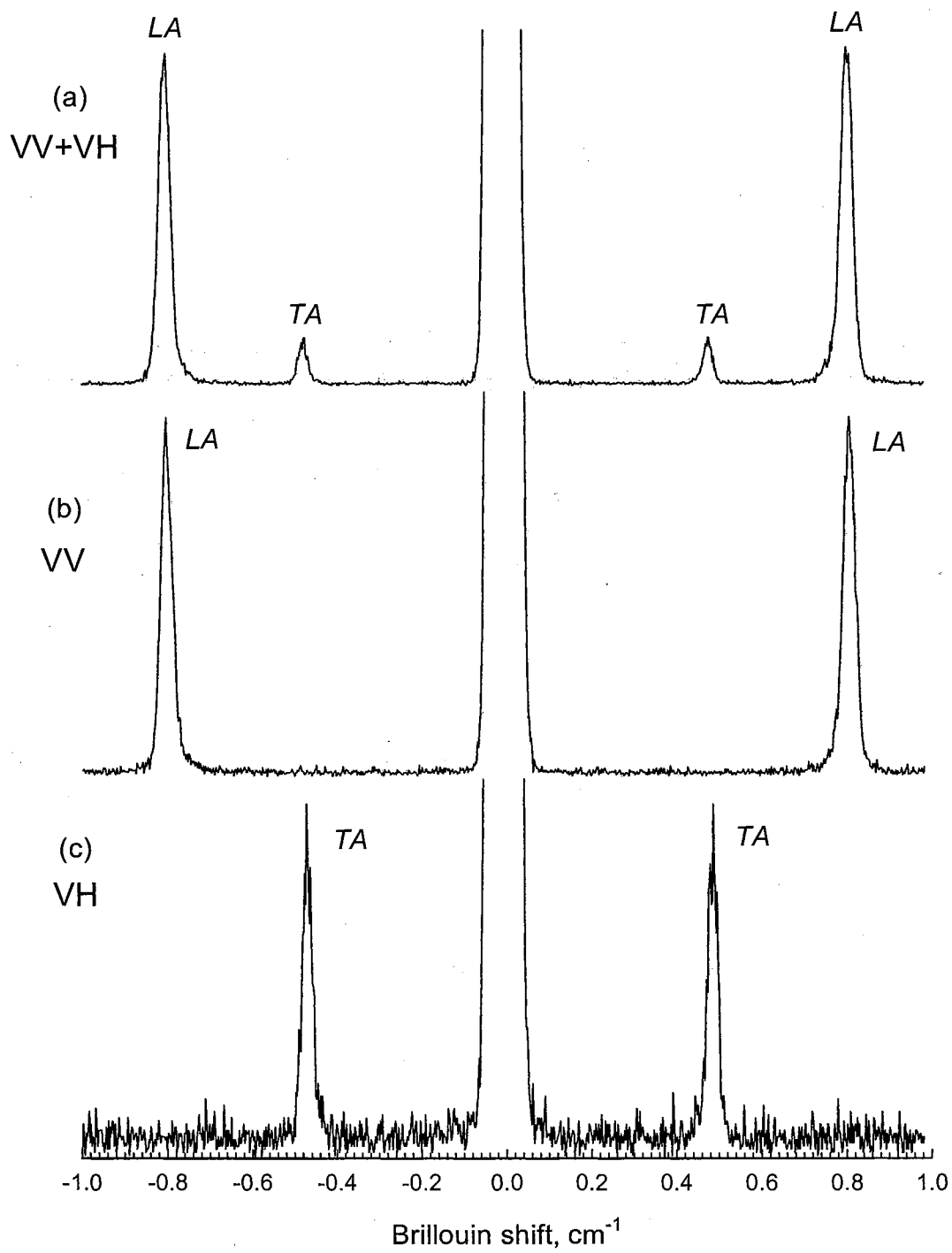
Fig.8. Polarized BLS spectra of Eu1.26 glass: (a) Vertical-Nonpolarized (or VV+VH)

(b) Vertical-Vertical (VV); (c) Vertical-Horizontal (VH)
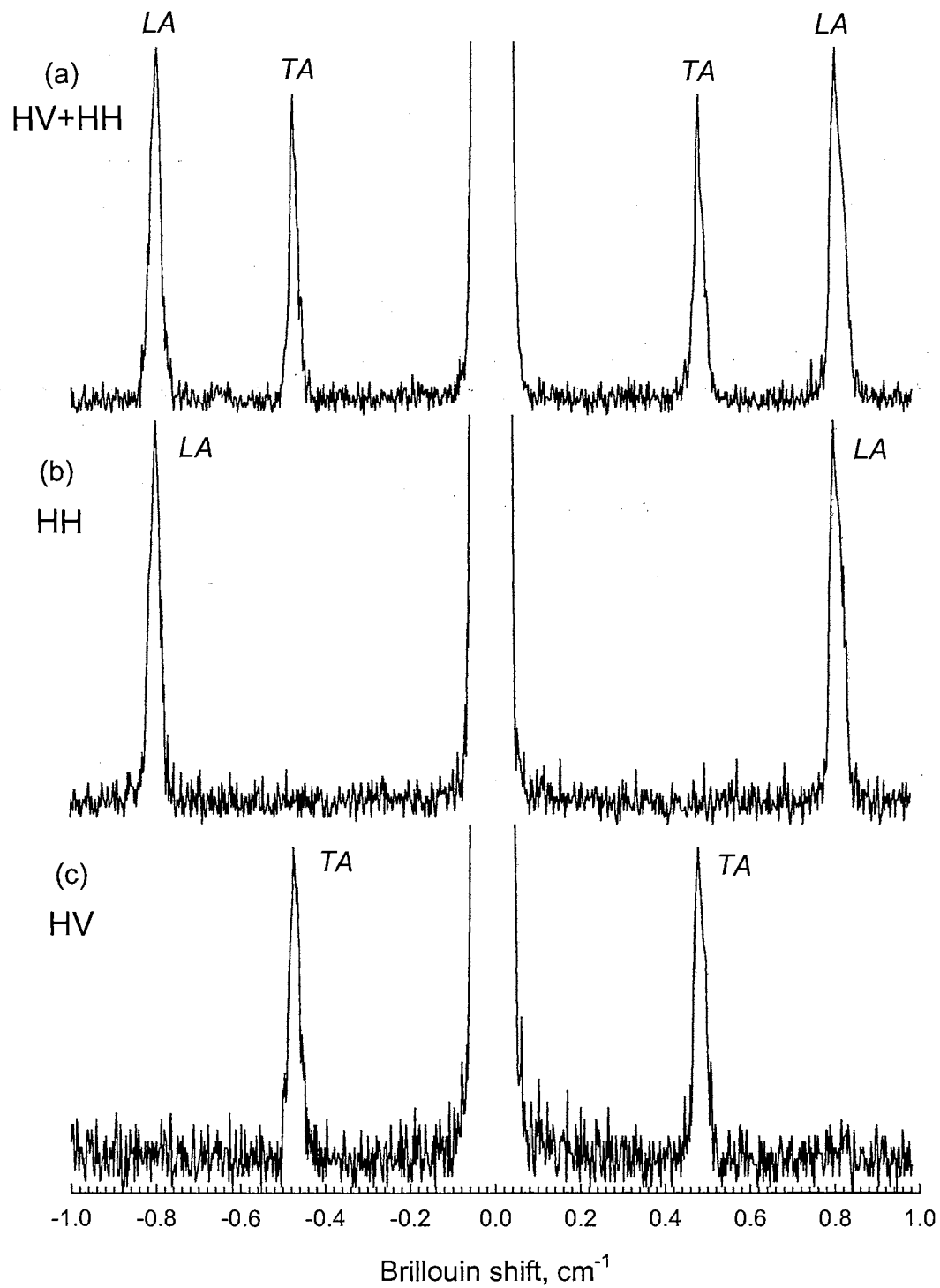
Fig.9. Polarized BLS spectra of Eu1.26 glass: (a) Horizontal-Nonpolarized (or

HV+HH) (b) Horizontal-Horizontal (HH); (c) Horizontal-Vertical (HV)

$$I_{HH} = \frac{\Delta\Omega}{2r^2} P_i L_{eff} \left(\frac{\omega_i}{c}\right)^6 \frac{k_B T}{\pi^2} \frac{n^{10}}{\rho \omega_L^2 (n+1)^4} (P_{11} - P_{12})^2 \qquad (2.1.17b)$$

$$I_{VH} = I_{HV} = \frac{\Delta\Omega}{2r^2} P_i L_{eff} \left(\frac{\omega_i}{c}\right)^6 \frac{k_B T}{\pi^2} \frac{n^{10}}{\rho \omega_T^2 (n+1)^4} P_{44}^2 \qquad (2.1.17c)$$

It is usually very difficult to measure directly photoelastic constants using (2.1.17) since they involve the *absolute measurement* of the scattering intensities, collection angles and the distances from scattering columns to the PMT. For practical convenience one can measure Pockel's photoelastic constants P_{12} and P_{44} using the ratio of the measured absorption-free integrated Brillouin scattering intensities for the longitudinal and transverse Brillouin components of the glass under study, respectively, to that of the etalon glassy material [45, 47, 48]:

$$P_{12} = \pm \left(\frac{\rho I_L(VV)}{\rho^0 I_L^0(VV)}\right)^{1/2} \frac{\omega_L}{\omega_L^0} \left(\frac{n^0}{n}\right)^5 \left(\frac{n+1}{n^0+1}\right)^2 P_{12}^0 \qquad (2.1.19a)$$

$$P_{44} = \pm \left(\frac{\rho I_T(VH)}{\rho^0 I_T^0(VH)}\right)^{1/2} \frac{\omega_T}{\omega_T^0} \left(\frac{n^0}{n}\right)^5 \left(\frac{n+1}{n^0+1}\right)^2 P_{44}^0 \qquad (2.1.19b)$$

for longitudinal (*VV*) and transverse (*VH*) acoustic modes, respectively. The measured values for the etalon glassy sample are labeled with superscript "0". These formulas are valid as long as the BLS measurements for all glass samples and etalon are performed at the following fixed parameters: air temperature T, laser frequency ω_i, laser power P_i, collection solid angle $\Delta\Omega$, fixed scattering angle ($\theta = 90°$), effective scattering column length L_{eff} defined by the spectrometer exit pinhole diameter D, ($L_{eff} = D < L$) and the distance r from the sample's scattering column to the PMT.

A theoretical treatment of the Pockels elasto-optic constants P_{12} and P_{44} for amorphous solids was proposed by Carleton [49] and Matusita [50] as follows:

$$P_{12} = \frac{(n^2-1)^2}{n^4}\left(\frac{M}{4\pi\alpha\rho N_A} - \frac{2}{15} - \frac{8}{15}*3\alpha G\right) = LLE + LE + AE \qquad (2.1.20)$$

$$P_{44} = \frac{(n^2-1)^2}{5n^4}(1-3\alpha G) = -\frac{2}{3}LE + \frac{8}{3}AE \qquad (2.1.21)$$

where n is the index of refraction, α is the glass average polarization, ρ is the particle density, M is the molecular weight of the glass, N_A is the Avogadro's number and the correlation integral G is given by

$$G = \int_0^\infty g_{12}(r)\frac{dr}{r^4} \qquad (2.1.22)$$

where $g_{12}(r)$ is a two-particle radial distribution function. As seen from equation (2.1.21) P_{44} does not have a direct density dependence. This is because an average displacement between neighboring atoms in the direction perpendicular to the direction of the compressional sound wave is negligible compared to that in the direction collinear with the propagating sound wave. The photoelastic constant P_{12} displays the contribution of three terms: (i) the change of refractive index due to local density changes accompanied by a light induced strain (Lorentz – Lorentz effect (LLE)), (ii) anisotropic correction to the refractive index as a result of the elliptical distortion of the Lorentz cavity by the light induced strain resulting in the deformation of the lattice with no changes at the individual atomic sites (lattice effect (LE)), (iii) correlation term, reflecting an additional polarizing effect of neighboring atoms on each other yielding the deformation of an individual atomic sites with no changes in the lattice (atomic effect (AE)).

To discuss the significance of variations in the measured photoelastic constants P_{12} and P_{44} in the light of Carleton-Matusita theory, we can solve the system of two linear equations (2.1.20) and (2.1.21) to get two variables: polarizability α and correlation

integral G using measured values of P_{12} and P_{44}, the refractive index n, density ρ, and the

calculated glass molar mass M based on the glass composition (Table 1):

$$\alpha = \frac{M}{4\pi\rho N_A\left[\dfrac{n^4}{(n^2-1)^2}(P_{12} - \dfrac{8}{3}P_{44}) + \dfrac{2}{3}\right]} \qquad (2.1.23)$$

$$G = \frac{4\pi\rho N_A}{3M}\left(1 - \frac{5n^4 P_{44}}{(n^2-1)^2}\right)\left(\frac{n^4}{(n^2-1)^2}\left(P_{12} - \frac{8}{3}P_{44}\right) + \frac{2}{3}\right) \qquad (2.1.24)$$

2.2. RAMAN LIGHT SCATTERING (RLS)

Contrary to BLS where *acoustic phonons* are involved, RLS is the scattering of the

incident light by the *optical phonons* (atomic or molecular oscillations with vibrational

energy on the order of $(10^0\text{-}10^3)$ cm^{-1}) occurring in the material under laser light

exposure. Raman effect is the inelastic scattering of light caused by the modulation of the

polarizability of the medium by the vibrations (and other excitations in solids, including

plasmons, excitons, magnons). This effect was first observed in Raman laboratory in

1928 [51]. The vibrational Raman effect was well documented and well understood by

Placzek in 1934 [52]. The development of laser, the improved optical spectrometer and

detection techniques have given a new impetus to RLS in the past 40 years. According to

classical treatment of the Raman effect, we assume that the electric field of the

electromagnetic radiation incident on the material is an oscillating function:

$$E = E_0 \cos(\omega_i t) \qquad (2.2.1)$$

The induced dipole moment caused by the external electric field in the first-order

approximation is

$$\mu = \alpha E = \alpha E_0 \cos(\omega_i t) \qquad (2.2.2)$$

26

For small displacements of the electron cloud a change in polarizability yields:

$$\alpha = \alpha_0 + \left(\frac{\partial \alpha}{\partial Q}\right) Q + \ldots \tag{2.2.3}$$

where Q is the normal coordinate. Assuming the harmonic approximation for the normal coordinate Q of oscillating atoms:

$$Q = Q_0 \cos(\omega_n t) \tag{2.2.4}$$

Then, the polarizability (2.2.3) becomes:

$$\alpha = \alpha_0 + \left(\frac{\partial \alpha}{\partial Q}\right) Q_0 \cos(\omega_n t) + \ldots \tag{2.2.5}$$

The corresponding dipole moment is given by sum of three terms:

$$\mu = E_0 \cos(\omega_i t)[\alpha_0 + \left(\frac{\partial \alpha}{\partial Q}\right) Q_0 \cos(\omega_n t)] =$$

$$\alpha_0 E_0 \cos(\omega_i t) + \left(\frac{\partial \alpha}{\partial Q}\right)\left(\frac{Q_0 E_0}{2}\right) \cos((\omega_i - \omega_n)t) + \left(\frac{\partial \alpha}{\partial Q}\right)\left(\frac{Q_0 E_0}{2}\right) \cos((\omega_i + \omega_n)t) \tag{2.2.6}$$

where the first, second and third terms stand for the Rayleigh (no phonon involvement), Stokes (phonon creation) and anti-Stokes (phonon annihilation) RLS, respectively.

In the quantum mechanical treatment of the RLS, the populations of atoms at higher and lower states are not the same and they obey the Boltzman distribution, such that anti-Stokes to Stokes intensity ratio is given by the ratio:

$$\frac{I_{AS}}{I_S} = \left[\left(\frac{\omega_i + \omega_n}{\omega_i - \omega_n}\right)\right]^4 \exp\left(\frac{-\hbar \omega_n}{kT}\right) \tag{2.2.7}$$

The induced transition probability matrix P_{nm} between m_{th} and n_{th} levels is:

$$P_{nm} = \int \Psi_m \alpha \Psi_n dQ \tag{2.2.8}$$

where n and m are the ground state and excited states. In general, RLS intensity I_{nm} is given by

$$I_{nm} = c(v_0 + v_{nm})^4 P_{nm}^2 \qquad (2.2.9)$$

The disordered structure of glasses causes the network vibrations to have a short coherence length compared to the optical wavelength. This causes a beak-down of the wave-vector selection rule which is present for crystalline Raman spectra and results in the Raman spectra for glasses which are directly related to the vibrational density of states [53]. In addition, the vibrational modes of a glass are more localized than those of a crystal due to the lack of translational symmetry. This Stokes Raman scattering intensity from glasses is given by [54]:

$$I(\omega, \omega_0) = (h\upsilon E_0^2/4\pi^2 c^3)\{(\omega_0 + \omega)^4 *\{n(\omega, T)+1\}/\omega\} * \sum C_b(\omega, \omega_0) \, g_b(\omega) \qquad (2.2.10)$$

where b refers to the different bands, E_0 and ω_0 are the incident light's electric field and frequency, respectively, ω is the frequency of the Raman shift, $g_b(\omega)$ is the vibrational density of states for b-band, $n(\omega, T) = 1/[exp(h\omega/kT)-1]$ is Bose-Einstein phonon population factor and $C_b(\omega, \omega_0) = /\sum_l P^l u_l^b(\omega)/^2$ is the coupling constant for the b-band. Here P^l is the electronic polarizability and u_l^b is the normal displacement coordinate, where l refers to the 3N Cartesian coordinates of the atoms.

The Raman effect is a form of electronic (more accurately vibronic) spectroscopy, although the spectrum contains vibrational frequencies. In classical terms, the interaction can be viewed as a perturbation of the molecule's electric field. In quantum mechanics the scattering is described as an excitation to a virtual state lower in energy than a real electronic transition with nearly coincident de-excitation and a

change in vibrational energy. The time scale for the scattering event is on the order of tens of femtoseconds or less. The virtual states description for the RLS of Stokes and anti-Stokes events are shown in Fig. 10:
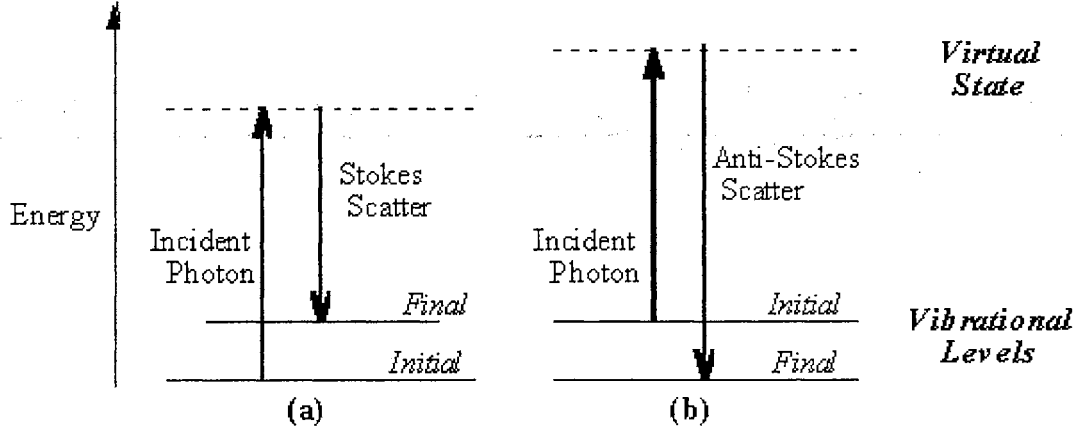
Figure 10. Energy level diagram for: (a) Stokes RLS (b) anti-Stokes RLS

The energy difference between the incident and scattered photons is represented by the arrows of different lengths in Fig. 10. Numerically, the energy difference between the initial and final vibrational levels, $\bar{\nu}$, also known as Raman shift often measured in wave numbers (cm^{-1}) as:

$$\bar{\nu} = \frac{1}{\lambda_{incident}} - \frac{1}{\lambda_{scattered}}$$
(2.2.11)

in which $\lambda_{incident}$ and $\lambda_{scattered}$ are the wavelengths (in cm) of the incident and Raman scattered photons, respectively. The vibrational energy is ultimately dissipated as heat. Because of the low intensity of RLS (10^{-6} or 10^{-7} times intensity of the incident beam), the heat dissipation does not cause a measurable temperature rise in a material. At room

29

temperature the thermal population of vibrational excited states is low, although not zero. Therefore, the initial state is the ground state, and the scattered photon will have lower energy (longer wavelength) than the exciting photon. This Stokes shifted scatter is what is usually observed in Raman spectroscopy. Figure 10(a) depicts Raman Stokes scattering. A small fraction of the molecules are in vibrationally excited states. RLS from vibrationally excited atoms leaves an atom in the ground state. The scattered photon appears at higher energy, as shown in Figure 10(b). This anti-Stokes-shifted Raman spectrum is always weaker than the Stokes-shifted spectrum at cryogenic temperatures because of (2.2.7), but at room temperature it is strong enough to be useful for vibrational frequencies less than about 1500 cm^{-1}. The Stokes and anti-Stokes spectra contain the same frequency information. The ratio of the anti-Stokes to Stokes intensity (2.2.7) at any vibrational frequency can be used to measure an ambient absolute temperature T.

2.3. SOLID-STATE NUCLEAR MAGNETIC RESONANCE (NMR)

Nuclear magnetic resonance (NMR) spectroscopy has been a standard tool for the characterization of organic molecules in liquid solution since at least the late 1960s. However its application to crystalline and then glassy silicates only began with the development of high-field superconducting magnets, pulsed Fourier transform methods and the application of the Magic Angle Spinning (MAS) technique which dates back to 1980 [55]. In general, in an NMR measurement a signal from a single isotope is observed, and the information content of the signal is usually dominated by the local structure of the element being studied, for example by coordination number, first and second neighbor bond distances, bond angles and connectivity to the first few neighboring atoms.

Magnetic nuclei possess an intrinsic angular momentum known as *spin*, whose magnitude is quantized in units of *(h/2π)* is given by *[I(I+1)]$^{0.5}$(h/2π)*. The spin quantum number *I* of a nucleus may have one of the following values: *I = 0, ½, 1, 3/2, 2, ...* Space quantization of the spin angular momentum provided by $I_z = m(h/2π)$, where *m* is the magnetic quantum number having *2I+1* values in integral steps between *+I* and *–I*: *M = I, I-1, I-2, ... -I+1, -I* with quantum numbers greater than 4 being rare. In the absence of a magnetic field, all *2I + 1* orientations of a spin *– I* nucleus have the same energy. This degeneracy is removed when a magnetic field is applied: the energy of a magnetic moment *μ* in a magnetic field *B* is minus the scalar product of the two vectors:

$$E = - \mu \, B = -\mu_z \, B \qquad\qquad (2.3.1)$$

The magnetic moment of a nucleus is connected with its spin angular momentum:

$$\mu = \gamma I \qquad\qquad (2.3.2)$$

Thus, we have the resonance condition:

$$\Delta E = -\mu_z \, B = -\gamma I_z \, B = -\gamma m (h/2\pi) B = h\nu \qquad\qquad (2.3.3)$$

so that the NMR resonance frequency is given by $\nu = -\gamma B/2\pi$ $\qquad$ (2.3.4)

Typical NMR magnetic strength $B_{NMR} = 9.4T = 94000$ *Gauss which is 10^5* times higher than B_{Earth}. For H_2 we have $\nu = 400$ *MHz*. This falls in the radio-frequency spectral range of the electromagnetic radiation. The radiation required to induce NMR transitions is consequently referred to as the radio-frequency field. In reality the resonance frequency depends not only on magnetic field strength but also on the position of the nucleus in the molecule, or to be more precise, on the local electron distribution. This effect is known as the *chemical shift* [56]. Namely this feature of NMR makes it so

attractive for scientists. It allows one to distinguish, e.g., the three types of hydrogen atom present in ethanol (Fig. 11).

Chemical shifts arise because the field, B, actually experienced by a nucleus in an atom differs slightly from the external field B_0, i.e. the field that would be left by a bare nucleus, stripped of its electrons. In an atom B is slightly smaller than B_0 because the external field causes the electrons to circulate within their atomic orbitals; this induced motion, much like an electric current passing through a coil of wire, generates a small magnetic field B' in the opposite direction to B_0 (Fig. 12). The nucleus is thus shielded from the external field by its surrounding electrons ($B = B_0 - B'$). B' is proportional to B_0 (the stronger the external field, the more it "stirs up" the electrons) and typically 10^4-10^5 times smaller. Thus, the field at the nucleus may be written as

$$B = B_0 - B' = B_0(1 - \sigma) \qquad (2.3.5)$$

where σ, the proportionality constant between B' and B_0, is called the *shielding (screening) constant*. As a result of nuclear shielding, the resonance condition becomes

$$\nu = -\frac{\gamma B_0(1-\sigma)}{2\pi} \qquad (2.3.6)$$

i.e. the resonance frequency of nucleus in an atom is slightly lower than that of a bare nucleus, stripped of all its electrons (Fig. 13). The shielding constant σ is an inconvenient measure of the chemical shift. It is common practice to determine the chemical shift in terms of the difference in resonance frequencies between the nucleus of interest (ν) and a reference nucleus (ν_{ref}), by means of a dimensionless parameter δ:

$$\delta = 10^6 \frac{\nu - \nu_{ref}}{\nu_{ref}} \qquad (2.3.6)$$

OH

CH₂

CH₃

Resonance frequency
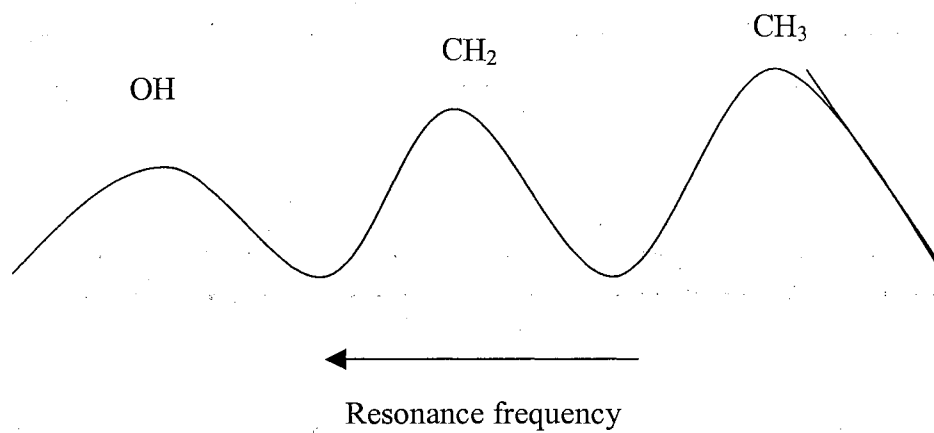
Fig.11. ^{1}H NMR spectrum of liquid ethanol, CH_3CH_2OH
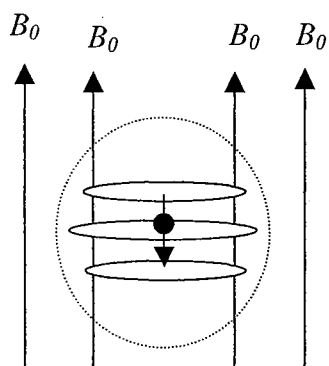
Fig. 12. An applied magnetic field B_0 causes the electrons in an atom to circulate within their orbitals. This motion generates an extra field B' at the nucleus in opposition to B_0
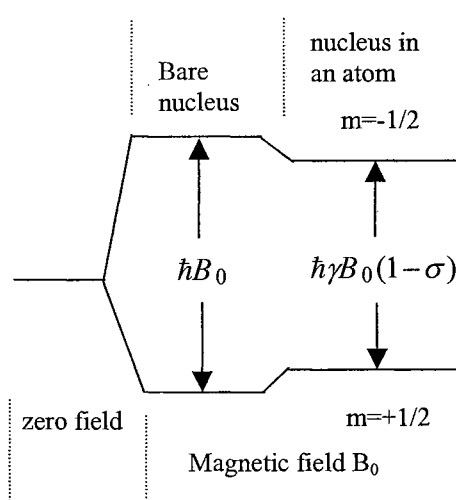
Fig. 13. Energy levels of a spin – ½ nucleus

δ values are quoted in *parts per million*, or *ppm*. The δ value is related to σ as follows:

$$\delta = 10^6 \frac{\sigma_{ref} - \sigma}{1 - \sigma_{ref}} \approx 10^6 (\sigma_{ref} - \sigma) \qquad (2.3.7)$$

where $\sigma_{ref} << 1$ has been used. An increase in σ *(greater shielding)* leads to a decrease in δ. Thus, δ is the *deshielding parameter*.

The use of solid-state NMR spectroscopy to examine the structural nature, reactivity, physical and chemical properties of these materials is based on the ability of NMR to obtain nuclide-specific information about these solids. The most important criterion is the presence of a nucleus that possesses a non-zero nuclear magnetic moment since only such nuclei are observable by NMR spectroscopy. Because nearly all of the stable elements of the Periodic table have at least one isotope with a non-zero magnetic moment, NMR can be used to study a wide variety of inorganic substances. In particular, diamagnetic materials containing the nuclides such as ^{1}H, ^{11}B, ^{13}C, ^{15}N, ^{19}F, ^{23}Na, ^{27}Al, ^{29}Si and ^{31}P have been extensively studied.

In inorganic solids there are usually four types of spin interactions in diamagnetic materials taking place in NMR experiment in addition to main Zeeman interaction (H_Z): *chemical shift (CS) interaction (H_{CS}), direct magnetic dipole-dipole interaction (H_{DDD}), indirect dipole-dipole interaction (H_{IDD})* and *nuclear electric quadrupolar (H_Q) interaction*. The spin interactions can be described quantum mechanically in terms of the appropriate Hamiltonians. The total Hamiltonian H_{Total} for calculating the NMR spectra of a diamagnetic non-conducting solid is given by:

$$H_{Total} = H_Z + H_{CS} + H_{DDD} + H_{IDD} + H_Q \qquad (2.3.8)$$

CS interaction is due to the screening of the applied magnetic field at a given nuclear magnetic moment by surrounding electrons. The additional, internal magnetic field at the

nucleus opposes the external magnetic field B_0 and has strength proportional to B_0. It is also spatially anisotropic, known as *chemical shift anisotropy (CSA)*. To account for this, we include in the nuclear Zeeman Hamiltonian

$$H_Z = -\gamma \hbar I B_0 \tag{2.3.9}$$

the term $H_{CS} = -\gamma \hbar I \sigma B_0$, where σ is the second rank chemical shift tensor. Secular part of the Hamiltonian is:

$$H_{CS} = \gamma \hbar \sigma_{zz} I_z B_0 \tag{2.3.10}$$

Where $\sigma_{zz} = \sigma + (-\delta_{CS})[3\cos^2\theta - 1 + \eta_{CS} \sin^2\theta \cos^2 2\phi] \tag{2.3.11}$

and σ is the isotropic shielding, δ_{CS} is the anisotropy parameter and η is the asymmetry parameter. At large magnetic fields, σ is symmetric and can be described by three principal values, σ_{11}, σ_{22}, σ_{33}, and the angles which define the orientation of the principal axis. It has been shown that when the sample is spun at *magic angle $\beta = 54.74°$* to the magnetic field B_0 the time-averaged value of the tensor component along B_0 is given [57]

by: $\overline{\sigma_{zz}} = 1.5\ \sigma \sin^2\beta + 0.5\ (3\cos^2\beta - 1) \sum_{j}^{3} \sigma_{jj} \cos^2 \chi_j \tag{2.3.12}$

where $\sigma = (1/3)(\sigma_{11} + \sigma_{22} + \sigma_{33})$ and χ_j is the angle between the spinning axis and each of the thee principal axes. The overall effect is the reduction of σ_{ZZ} to the scalar isotropic value σ, and the shift anisotropy is removed from the NMR spectrum for every nucleus in the sample.

The *direct dipole-dipole interaction* is a consequence of direct through-space interaction between the magnetic moments $\gamma_i \hbar I^i$ and $\gamma_j \hbar I^j$ of two nuclei. The corresponding interaction Hamiltonian is:

$$H_{DDD} = \frac{\gamma_i \gamma_j h^2}{r_{ij}^3} [I^i \cdot I^j - 3\frac{(I^i \cdot r_{ij})(I^j \cdot r_{ij})}{r_{ij}^2}] \qquad (2.3.13)$$

where γ_i, γ_j are gyromagnetic ratio of each nucleus, r_{ij} is the inter-nuclear vector. For the

homonuclear case ($\gamma_i = \gamma_j = \gamma$), the secular dipolar Hamiltonian is given by:

$$H_{D,II}^{sec} = \sum \frac{\gamma_i^2 h \mu_0}{4\pi r_{ij}^3}(3\cos^2\theta_{ij} - 1)(3I_z^i I_z^j - I^i \bullet I^j) \qquad (2.3.14)$$

For the *heteronuclear* case ($\gamma_i = \gamma_I \neq \gamma_j = \gamma_S$), the secular Hamiltonian is:

$$H_{D,IS}^{sec} = \sum \frac{\gamma_I \gamma_S h \mu_0}{4\pi r_{IS}^3}(3\cos^2\theta_{ij} - 1)I_Z S_Z \qquad (2.3.15)$$

where θ_{ij} is the angle between r_{ij} and the Zeeman field B_0, which is directed along the z - axis in the laboratory frame of reference. I_z and S_z refer to the nuclei spin operators. It should be noted that this type of interaction vanishes at *magic angle* $\theta_{ij} = 54.7°$.

The *indirect dipole-dipole (scalar* coupling*)*, or *J*-coupling, arises from indirect spin-spin coupling between two spins via the electronic surroundings [91]:

$$H_{IDD} = \sum_{ij} I_i J_{ij} I_j \qquad (2.3.16)$$

where J_{ij} is the coupling tensor for the two spins *i* and *j*. The scalar coupling occurs because a bonding electron's spin tends to correlate with the spin of its neighboring nucleus. The electron has been influenced, and will thus influence other neighboring spins. This type of interaction is very important in solution-state spectroscopy where the motional averaging removes the effects of direct dipolar interaction on the positions of the resonance. In solids the *J*-coupling is often neglected since it is typically much weaker than *direct dipole-dipole* coupling, but it can be significant in highly crystalline samples.

Nuclei with a spin quantum number $I = \frac{1}{2}$ treated as two-level system with states $m = -\frac{1}{2}$ and $m = +\frac{1}{2}$, have been extensively studied by NMR. Some of the most widely examined *spin-½* nuclides in inorganic materials are ^{29}Si, ^{1}H, ^{13}C, ^{15}N, ^{31}P, ^{19}F, ^{113}Cd, ^{119}Sn. The most important interactions for spin-½ nuclei in solids include *Zeeman*, the *dipole-dipole* and *chemical shift* interactions. Over two thirds of the NMR active nuclei in the periodic table have spin quantum number $I \geq 1/2$ and are called *quadrupolar* nuclei. Among them are ^{2}H (spin 1), ^{6}Li (spin 1), ^{14}N (spin 1), ^{17}O (spin 5/2), ^{23}Na (spin 3/2), ^{25}Mg (spin 5/2), ^{27}Al (spin 5/2), ^{39}K (spin 3/2), ^{93}Nb (spin 9/2), ^{133}Cs (spin 7/2), etc. Both types, *spin-1/2* and *quadrupolar* nuclei are listed in [58] together with some other relevant parameters including natural abundances, receptivities (relative to ^{1}H), Larmor frequencies (in MHz) at 11.7 T and examples of some important materials containing these nuclides. As in case of *spin-1/2* nuclei, splittings of the *quadrupolar* nucleus levels are largest for *Zeeman* interaction, while *chemical shift, direct dipole-dipole* coupling and *indirect dipole-dipole* coupling are treated as perturbation. Since there are now more than two energy levels, multiple transitions [58], and hence multiple resonances for a single nucleus are possible. A nucleus with $I > 1/2$ also has a non-spherically symmetric charge distribution and hence a non-zero nuclear electric *quadrupole* moment (*eQ*). Such a moment will interact with an electric field gradient present in the sample due to an asymmetric distribution of electrons around the nucleus. This interaction is known as the *nuclear electric quadrupolar* interaction. As in case of chemical shift and direct dipolar couplings, it is anisotropic, i.e. orientation-dependent. Electric field gradient is described by the traceless symmetric tensor:

$$V_{ij} = \frac{\partial^2 V}{\partial x_i \partial x_j}$$

(2.3.17)

where V is the electric potential and x_I and x_j are Cartesian coordinates. In the principal axis system of V_{ij}, in which the tensor is diagonal, the quadrupolar Hamiltonian for a single spin is

$$H_Q = \frac{e^2 qQ}{4I(2I-1)}[3I_z^2 - I^2 + \eta(I_x^2 - I_y^2)] \qquad (2.3.18)$$

In the case of ^{27}Al in aluminosilicate glasses the magnitude of $H_Q \ll H_Z$, i.e. H_Q can be treated as perturbation on the Zeeman levels. For ^{27}Al which has a non-integral spin, I = 5/2, only the central $-1/2 \leftrightarrow 1/2$ transition is generally observed in single pulse experiments, as the other transitions are spread over too wide a frequency range. If the electric field gradient is axially symmetric ($\eta_Q = 0$), the expressions for the first- and second-order frequency shifts, are [59]:

$$\omega_m^{(1)} = -(1/2)\omega_Q (m - 1/2)(3\cos^2 \theta - 1), \qquad (2.3.19) \text{ and}$$

$$\omega_{1/2}^{(2)} = -(\omega_Q^2/16\omega_L)(a - 3/4)(1 - \cos^2 \theta)(9\cos^2 \theta - 1) \qquad (2.3.20)$$

where $\omega_Q = 3e^2 qQ/2hI(2I-1)$, $\omega_L = \gamma B_0 (1-\sigma)/2\pi$ and $a=I(I-1)$.

We can see that the rapid sample spinning at the *magic angle* eliminates the first-order quadrupolar anisotropy. However, even at fast speeds, magic-angle spinning alone does not average out the second-order quadrupolar effects, so that there is still a strong orientation-dependence. From (2.3.20) second-order shift is inversely proportional to B_0 (through ω_L), therefore, we need to work at high magnetic fields to minimize second-order effects. However, like the other anisotropic interactions, it also further complicates the solid-state NMR spectrum, and special techniques must be used to isolate its effects. In general, the *quadrupolar* interaction provides information about bond strengths, bond angles and site symmetry in the vicinity of the quadrupolar nucleus.

All techniques allowing studying NMR of inorganic solids are based on pulsed Fourier transform spectroscopy. That is, a sequence of RF-pulses is applied to the sample to manipulate the spins in the desired manner. The response of the spin system as a function of time is then recorded. This time-domain signal is known as free induction decay with the decay being caused by the relaxation of the perturbed spin-system back toward equilibrium. In NMR, relaxation of magnetization can be described by two parameters: the *spin-lattice relaxation time constant* (T_1), which is a measure of the rate of recovery of magnetization back to its equilibrium state (parallel to the B_0 field), and the *spin-spin relaxation time constant* (T_2), which is a measure of the decay of magnetization in the plane perpendicular to the B_0 field. Studies of NMR relaxation rates can provide much physical insight and are rich subject in their own right. Performing a Fourier transformation on the free-induction decay leads to a frequency spectrum. The dependence of some relaxation parameters on nuclear-nuclear separations (bond lengths) allows one to use these parameters to assist in the determination of atomic structure. In crystalline and glassy solids and in liquids, NMR can provide what is often unique information on the dynamics of atomic or molecular motion that occur on time scales ranging from seconds to nanoseconds or shorter. These time scales are much larger than those of interatomic vibrations and are often of great interest in defining mechanisms of displacive phase transitions, ionic conductivity, diffusion and viscous flow.

Suppose a group of nuclear spins are immersed in the static magnetic field B_0, so that a small but measurable magnetization M_z develops along the direction of B_0 from a net alignment of the individual nuclear magnetic moments. At equilibrium, when the

populations of the spin-energy levels are given by the Boltzman distribution, the net

magnetization in the z - direction M_0 is given by the Curie law:

$$M_0 = \frac{N\gamma^2\hbar^2 I(I+1)}{3kT} B_0 \qquad (2.3.21)$$

where N is the number of spins; γ is the gyromagnetic ratio; $\hbar$ is the Plank's constant

divided by 2π; k is the Boltzman constant; and T is the absolute temperature. The rate at

which M_z approaches M_0 is generally given by a first-order differential equation:

$$\frac{\partial M_z}{\partial t} = \frac{-1}{T_1}(M_z - M_0) \qquad (2.3.22)$$

where T_1 is the *spin-lattice relaxation time*. Integration of (3.2.2) yields

$$M_0 - M_z = Ce^{-t/T_1} \qquad (2.3.23)$$

where C depends on the initial conditions. If, initially, the macroscopic magnetization is

zero, $C = M_0$ and at $5T_1$, then $M_z = 0.9933M_0$. Taking the natural logarithm of both sides

of (3.2.3) gives

$$ln(M_0 - M_z) = \frac{-t}{T_1} + lnC \qquad (2.3.24)$$

where T_1 is, thus, a first-order time constant that characterizes the behavior of the z -

component of the macroscopic nuclear magnetization M_z in a static magnetic field B_0.

The rate at which the spin system gives up energy in the establishment of spin

equilibrium, $R_1 = 1/T_1$, depends on the rate at which it can transfer energy to its

surroundings, historically referred to as the lattice. The process by which spin energy

is transferred to other modes of energy is referred to as a relaxation mechanism.

Spin-lattice relaxation process is often characterized by a single exponential

constant T_1, although in solids this may often be only a rough approximation [60].

NMR spectra are usually acquired by averaging data from many separate pulses in order to increase signal-to-noise ratio. If pulses are given too rapidly relative to the relaxation rate, the spin system will saturate and the signal will disappear. Different sites in a material may have different relaxation rates, leading to non-quantitative spectra. In contrast, very rapid relaxation can lead to peak broadening, which in extreme cases can lead to unobservable NMR spectra.

On the other hand, measurements of spin-lattice relaxation can yield important data on dynamical processes, as well as on short-range to intermediate-range structure. Because the energies of nuclear spin transitions are relatively low, relaxation must be stimulated by fluctuations in the local magnetic field at the Larmor frequency, or by fluctuations in the electric field gradient for quadrupolar nuclides. These fluctuations may in turn be caused by motion of the atoms of the element of interest, or of those around it, or, in some cases, by fluctuations in the state of unpaired electrons on *paramagnetic ions* such as *transition metals* and *rare-earth elements*. If the relaxation process can be understood, then information on diffusion, polyhedral motion, site exchange etc., may be obtainable.

When an isolated spin system is at equilibrium in a static magnetic field B_0, there is no net magnetization in the xy plane [91]. If the spins are subjected to a $(\pi/2)_x$ RF pulse B_1, the net z magnetization is rotated into the xy plane along the positive y axis. In perfectly homogeneous magnetic field B_0, the decay of magnetization in the xy plane is governed by the spin – spin or transverse relaxation time (T_2), thus

$$\frac{\partial M_x}{\partial t} = -\frac{M_x}{T_2} ; \quad \frac{\partial M_y}{\partial t} = -\frac{M_y}{T_2} ; \qquad (2.3.25)$$

and $M_t^{x,y} = M_0 e^{-t/T_2}$

$\qquad\qquad\qquad\qquad\qquad\qquad\qquad\qquad\qquad\qquad$ (2.3.26)

Under these conditions, the rate of spin-spin relaxation, $R_2 \equiv 1/T_2$, is related to the full width at half-maximum $v_{1/2}$. For a Lorentzian line,

$$v_{1/2} = \frac{1}{\pi T_2} = \frac{R_2}{\pi} \qquad (2.3.27)$$

in practice, the magnetic field is not perfectly homogeneous; nuclei in different regions of the sample experience slightly different applied fields, causing them to precess at slightly different frequencies. This results in an enhanced dephasing of the spins in the xy – plane, and thus an effectively shorter spin-pin relaxation time T_2. The observed line width results from both field inhomogeneity and the natural T_2 of nuclei. Under these conditions: $v_{1/2} = \frac{1}{\pi T_2^*}$ \qquad (2.3.28)

where T_2^* is sometimes called the effective *spin-spin relaxation time*, and

$$v_{1/2}(\text{obs}) = v_{1/2}(\text{natural}) + v_{1/2}(\text{inhomo})$$

$$\frac{1}{\pi T_2^*} = \frac{1}{\pi T_2} + \frac{\gamma}{2\pi}\Delta B_0 \qquad (2.3.29)$$

where $\frac{\gamma}{2\pi}\Delta B_0$ is the magnetic-field inhomogeneity in Hertz. In practice, one finds $T_2 \leq T_1$ since any mechanism that contributes to T_1 relaxation will also contribute to T_2 relaxation. For many solids, $T_2 << T_1$ [61].

CHAPTER III
REVIEW OF LITERATURE

3.1. General properties of oxide glasses

It is well accepted that the short range order or the large range disorder are inherent for the glass structure which are characterized by three structural parameters: the bond length between the central atom and the nearest neighboring atom, the bond angle and the coordination number [62]. These three structural parameters for different glassy materials are also different from those of the crystalline state. In comparison with the crystalline state, the coordination numbers and the bond lengths are the same, whereas the bond angles have greater variation, which indicates that in the glassy state the presence of distorted tetrahedra takes place. For example, in most multi-component silicate glasses the angle Si-O-Si bridges ranges from 120° to 180°, which provides freedom for the vertex angle rotation and reflects the topological disorder of three dimensional structure in the glassy state.

It is very hard to represent various kinds of glasses with a unique structural model because each glass is different from others in structure and there is great variety of glass forming systems. According to Gan Fuxi [62], the silicate glass systems are described as random polyhedra packing systems. The tetrahedra are connected at the vertex points and form three-dimensional structural networks. Some ions with greater radii, such as Al^{3+} can form tetrahedra and enter the network, or form octahedra outside the network; this is random network model, which can be regarded as the random packing of tetrahedra. The ions with even greater radii, such as alkali metals and rare-earth ions are located at the vacancy of the polyhedron structure. In the study of variation rules of the dependence of

optical and spectroscopic properties on the glass composition and structure, it is believed that the effect of coordination is of utmost importance. In other words, it is of the greatest significance to study in what kind of polyhedra the major ions are located.

In multi-component silica-based glasses, SiO_4 tetrahedra form the backbone of the glass network with Si atoms being the network formers. Variable Si-O-Si combining angles are present with mean values about 145° for fused silica. Alkali ions (M^+) when introduced into the vitreous silica network cause formation of non-bridging oxygens (NBOs) and lead to the weakening of the glass structure. Although alkali earth ions (M^{2+}) incorporated into the fused silica also form weak Si-O-M^{2+}-O-Si bridges, M^{2+}-O bonds are stronger than M^+-O bonds and the M^{2+} ion must have two neighboring NBOs. For soda lime aluminosilicate glasses the large field strength of the calcium ion allows this divalent ion to act more like an intermediate ion and to have a larger effect on the strength of the bonds connecting the vitreous network [63]. Furthermore, the divalent calcium ion acts as a link between neighboring NBO ions, whereas the monovalent sodium ions tend to act simply to balance the charge neighboring NBOs, but also to act as structural links to maintain the connectivity of the network (of course these links are significantly weaker than the Si-O-Si linkages they replace).

Aluminum oxide Al_2O_3 is one of the most used components in many industrial glasses. In pure Al_2O_3, the Al^{3+} ions are adjacent only to O^{2-} ions, through which the O^{2-} ions on different sides are firmly bound and show only a slight polarizability. For this reason, to fill up the coordination, six O^{2-} ions are necessary. Then, the mutual combining of the polyhedrons only at the corners is no longer possible, so that pure Al_2O_3 occurs

only in crystalline modifications normally as corundum. The relationships are similar if Al_2O_3 is introduced into pure SiO_2 glass. The slightly polarizable O^{2-} ions that are present there force the Al^{3+} ion into the $[AlO_6]$ coordination, which can longer be seen as network forming. If Al_2O_3 is introduced into a soda-lime glass, the Al^{3+} ions is given the opportunity to construct $[AlO_4]$ coordinations with the more easily polarizable NBOs through which it becomes a network former. Thus, the effect of cation is very much dependent on the original glass composition. The $[AlO_4]$ coordination resembles the $[SiO_4]$ one, and in fact an Al^{3+} ion can take place of Si^{4+} atom in the glass structure [64]. One should note, however, that they possess different valences. The necessary valence compensation is accomplished through the lower valence modifiers (e.g. alkali ions) which have led to the formation of the NBOs. The replacement of SiO_2 by Al_2O_3, the places of separation due to previously incorporated alkali or alkali earth modifiers are closed through which the glass structure is again strengthened. If however, in alkali aluminosilicate glasses the molar ratio $M_2O:Al_2O_3<1$, then there are no longer enough alkali ions for valence compensation available to the Al^{3+} ions during the construction of the coordination of 4. The excess Al^{3+} ions are then present in the glass as network modifiers in octahedral coordination. Rare-earth ions entering the aluminosilicate glass usually act as network modifiers, causing the formation of a wide distribution of silica-based Q^3, Q^2 and Q^1 tetrahedra [19, 20, 30, 65].

3.2. BLS studies of oxide glasses

Using BLS spectroscopy one can study *elastic* and *photoelastic* properties of oxide glass materials. Elastic moduli such as compressional C_{11}, shear C_{44}, Young's (E), and

adiabatic bulk (B) moduli are particularly helpful in correlating structural changes in glasses which are expected to occur as a function of content and/or composition. Since the strength of materials increases with their elastic parameters, it is therefore possible to evaluate materials strength directly from their elastic properties. Aluminosilicate glasses are characterized by elastic properties in the hypersonic ($V_{L,T} > 10 V_{sound\ in\ air}$, $\omega_B \sim 0.8 cm^{-1}$ = 24GHz) frequency range. Another elastic parameter called Poisson ratio σ is defined as the proportionality constant between tensile and lateral stains. For solid-state materials this parameter depends on the dimensionality of the structure [66, 67] and the cross link density [68]. A three-dimensional network structure has a lower σ value than that of a two dimensional structure, which in turn, is less than that of a one-dimensional structure since the number of bonds resisting a transverse deformation decreases in that order. However, in glasses which are isotropic, the definition of dimensionality becomes less rigorous. Typical three dimensional glasses like SiO_2 or GeO_2 have $\sigma \sim 0.17$, whereas As_2S_3, B_2O_3, P_2O_5 glasses have $\sigma \sim 0.30$ which is an indication of a decrease in dimensionality for the latter systems. Addition of modifier oxides results in an increase of σ due to the creation of NBOs and hence a reduction in dimensionality [66].

The Brillouin spectra of binary and ternary silicate and borate [45, 69-71], calcium aluminosilicate [14, 72] glasses were investigated and absolute values for the elastic and photoelastic constants were calculated from measured spectra. Recently we used BLS to study rare earth (Eu^{3+} and Pr^{3+})-doped soda magnesia aluminosilicate glasses [18] and found that these glasses become more rigid and the bonding structure of the glasses becomes more ionic with increasing of RE concentrations. Because of the larger field strength of Eu^{3+} ions compared to that of Pr^{3+} ions, the elastic constants, Young's

modulus, and bulk modulus of glasses in Eu-series are higher than those of Pr-series. The analysis of photoelastic constants shows that the Lorentz-Lorenz and atomic effects decrease slightly while the lattice effect increases with the increase of RE concentration. Early BLS work on Eu^{3+}-doped alkali silicate glasses [46] revealed that the glass becomes softer as the size and mass of the modifying alkali ion increases by going from Li^+ to Cs^+. E.G. Behrens and co-workers [73] attributed the decrease of the grating strength in these glasses to the decreasing stability of the equilibrium configurations for migrating alkali ions. Photoelastic constants for both LA (P_{12}) and TA (P_{44}) modes increased which is partly due to the dilated distance in the M-O bond length, where M is an alkali modifying ion [46].

3.3. RLS studies of oxide glasses

In crystals the atoms form lattices with definite symmetry, so the lattice vibrations can be treated with group theory. Glass, however, has short-range order, so that its vibrational properties have their own features; however the remnants of translational symmetry always exist even in highly disordered solids, so some elements of crystal structure can also be observed in glasses with similar compositions. In particular, high wave-number modes arising from short distance scale structures which appear as sharp bands in crystals are broadened into density of states distributions in glasses [74]. Among the important features of the Raman spectra of glass we need to list the following: (i) independence of the RLS intensity on the sample orientation to the incident light direction due to the isotropy of the medium, (ii) disorder-induced broadened RLS peaks ~ (50-150) cm^{-1} for glass compared to ~ (5-10) cm^{-1} of crystals; (iii) break-down of the

wave-vector selection rule because the coherence length of the normal modes is much shorter than the light wavelength, normal vibrations are classified into various bands, such as stretching bands, breathing, bending, rocking etc.; (iv) the presence of the low frequency Boson peak typically at (40-130) cm^{-1}, attributed to the intermediate range order and the increase in the vibrational density of state caused by localized excitations [75]. This band appears as a result of the breakdown of the translational symmetry or from vibrations of structure within the glass larger than the polyhedra.

There have been several Raman investigations of structural changes in silica-based glasses containing various rare-earth ions. Raman spectral studies indicate that the structure of rare-earth aluminosilicate glass is more disordered than that of alkali or alkaline earth aluminosilicate glasses due to the broader distribution of various types of SiO_4 tetrahedra present in the glass [19, 20, 76]. These structural units are commonly denoted as Q^n, with n being the number of bridging oxygens (BO) per tetrahedron. Si-NBO vibrations with NBO coordinated to lanthanide lie at lower wave-numbers in the Raman spectrum than those with NBO coordinated to ions of lower valence [77, 78]. The high field strength of rare-earth ions has been proposed to be responsible for the reduced force constant of the Si-NBO bond with NBO coordinated to rare-earths [79].

3.4. Solid-State NMR studies of oxide glasses

In an NMR experiment, the chemical shift of a nucleus is affected by the screening of the applied field at the nucleus by surrounding electrons. The distribution of the electrons around the nucleus of interest, and hence the chemical shift, depends mainly on the position and composition of neighboring atoms [80]. Interpretation of

the MAS-NMR results for glasses is based primarily on comparison with crystal data from which empirical relationships between chemical shift and structure have been established.

^{27}Al NMR spectra of glasses give, in general, broad signals with chemical shifts in the approximate range 50-75 ppm relative to $Al(H_2O)_6^{3+}$ that is typical of tetrahedrally coordinated AlO_4 groups. In a few calcium aluminosilicate glasses with $Al_2O_3/CaO>1$ a further signal at chemical shifts of about -3 to +10 ppm has been observed, which indicates the presence of six-fold coordinated AlO_6 octahedra in these systems [81]. However, quantitative studies have shown that ^{27}Al NMR spectra of glasses do not, in general, sample all the Al species present in the glass, and in extreme case up to 90% of the total Al content does not contribute to the spectrum [82]. The deficient NMR intensity reflects the presence of Al in highly disordered environments, the ^{27}Al lines of which may be broadened beyond detection owing to strong quadrupolar interactions and possibly to a large distribution of chemical shifts. The ^{27}Al NMR spectra therefore indicate that a considerable proportion of the aluminum in aluminosilicate glasses occurs in a distorted state which cannot be partitioned off with respect to four- or six-fold coordination.

Unfortunately the analysis of ^{27}Al chemical shifts is complicated by second-order quadrupolar interactions. The magnitude of the quadrupolar shift depends on the values of the asymmetry and quadrupolar coupling parameters which in turn are related to the electric field gradient at the nucleus of interest. In the case of glass, which has a large degree of disorder in the structure, these parameters are poorly constrained and extraction of the isotropic chemical shift and quadrupolar

contribution is not possible. Therefore, our discussion will be based on changes in the position of the [27]Al peak which is a combination of chemical and quadrupolar shift variation.

^{29}Si MAS NMR spectra of alkali [32, 83], alkaline earth [33, 83], and yttrium [30] aluminosilicate glasses are poorly resolved and do not show distinct peaks for different Q^n species. However, some information has been derived from the position of the resonance, indicating which of the Q^n species is predominant (often Q^2, Q^3 or Q^4). Also informative are the shape and breadth of the resonance, which suggest the range and relative amounts of different Q^n species. ^{27}Al MAS NMR spectra of glasses have shown that the coordination of aluminum is usually four-fold in alkali aluminosilicate glass [32, 34] and alkaline earth aluminosilicate glass [33]. Octahedrally coordinated Al has also been found in some rare earth doped aluminosilicate glasses [20, 21, 30].

The [23]Na nucleus has spin I = 3/2 and, like [27]Al, a large *quadrupole* moment and 100% natural abundance. Because the nuclear spin of [23]Na is smaller than that of [27]Al (I = 5/2), for the same quadrupole coupling constant sodium has a larger second-order quadrupolar width and hence broader lines. This width can be reduced at higher magnetic fields [84]. Therefore, the second-order quadrupolar doublet pattern is often only narrowed but not reduced to a single line under MAS conditions. The ^{23}Na NMR peak of *albite* glass [82] with the maximum at -18.3 ppm is quite broad and featureless, indicating sites with a range of quadrupole coupling constants, asymmetry parameters and/or chemical shifts. [23]Na isotropic chemical shift correlates well with both the Na coordination and the degree of polymerization of the materials. The

average Na coordinations in glasses of similar compositions vary little with Na content (degree of polymerization). ^{23}Na MAS NMR data for two series of mixed alkali silicate and aluminosilicate glasses with varying K/Na and Rb/Na ratios [85, 86] show larger changes which may be attributed to changes in the average Na coordination. These limited data suggest that the local Na coordination environments in silicate glasses are more sensitive to the introduction of other network modifiers than to the topology of the tetrahedral network and warrant further studies on silicate glasses containing mixed cations. The peak position on ^{23}Na MAS spectra of aluminosilicate glasses moves toward higher frequencies with increasing Al/Si ratio, implying that the average Na-O distance decreases [84]. The high-field ^{23}Na NMR is an effective probe of the Na$^+$ environment providing not only average structural information but also chemically and topologically distinct chemical shift ranges (distributions) and their variation with composition.

CHAPTER IV

EXPERIMENTS

4.1. Glass sample preparation

The melt-quenching technique was utilized to prepare EDSMAS glasses. The glass samples were made in batches from sodium carbonate, magnesium earth carbonate, europium carbonate, alumina and silica precursor powders of 99.997%, 99.996%, 99.99%, 99.999% and 99.999% purity respectively based on metals basis. Non-oxide powders were utilized, whenever possible, to improve precursor subdivision in the final melt. All powders were mixed in an automated mixer for approximately one hour prior to being loaded into a platinum crucible and placed in a furnace. For complete decomposition of the carbonates from the starting material the temperature of the furnace was raised to 800°C and held for 18 hours, then raised to 1350°C to approach the melting point and again held for 18 hours. The temperature of the furnace was then raised to 1650 °C, where it was maintained for 50 hours to achieve full melting of the mixture (to dissolve high melting components). The melt was stirred twice during this 50-hour period using a platinum rod. Finally, the temperature of the furnace was lowered to 1550 °C at a rate of -50 °C/hour. Once at 1550°C, the glass was transferred to a 425°C annealing furnace to get rid of strains. The temperature of the annealing furnace was then raised to 725°C (glass transition temperature) to relieve large scale strains and the glass was maintained at this temperature for at least 1 hour. The annealing furnace was then turned off, and the glass was allowed to cool down to room temperature. Bubble-free samples with high optical quality were made using this method.

For the Brillouin and Raman studies, the high quality glass samples were cut into a parallelepiped shape and polished using cerium oxide polishing material. For the NMR studies EDSMAS glass samples were finely ground to powder with a ceramic mortar and pestle.

4.2. BLS experiment and procedures

Fig.14 illustrates BLS setup. The incident light was produced by Ar^+ laser (*Spectra Physics 2020*) operating at 514.5nm wavelength in a single TEM_{00} mode. The scattered light from sample (s) was analyzed at room temperature (~23°C) using piezo-electrically scanned six-pass tandem Fabry-Perot interferometer (TFPI) with high contrast and finesse. The principle of TFPI operation is explained in detail in [87, 88]. The intensity of the filtered light was measured with *Hamamatsu R-463* photomultiplier tube and recorded on a 1024-channel multi-channel analyzer (*Canberra, 35 plus*). From this instrument the obtained spectra are downloaded to PC for further curve-fitting. Since for glasses *LA* and *TA* peaks are well spaced from each other in frequency domain, then using polarization rotator mounted to the laser head the direction of the incident polarization was fixed as vertical (*V*) while the Brillouin scattered light entering the TFPI was non-polarized (*N*). This way we can get two pair of peaks corresponding to *LA* and *TA* acoustic modes by acquiring single *VN* spectrum having *VV* and *VH* polarization components, respectively. The typical BLS (*VN* = VV + VH) spectrum from Eu1.26 EDSMAS glass is given in fig. 8(a).

90° Brillouin Scattering Setup

Sandercock 6-pass FP Interferometer
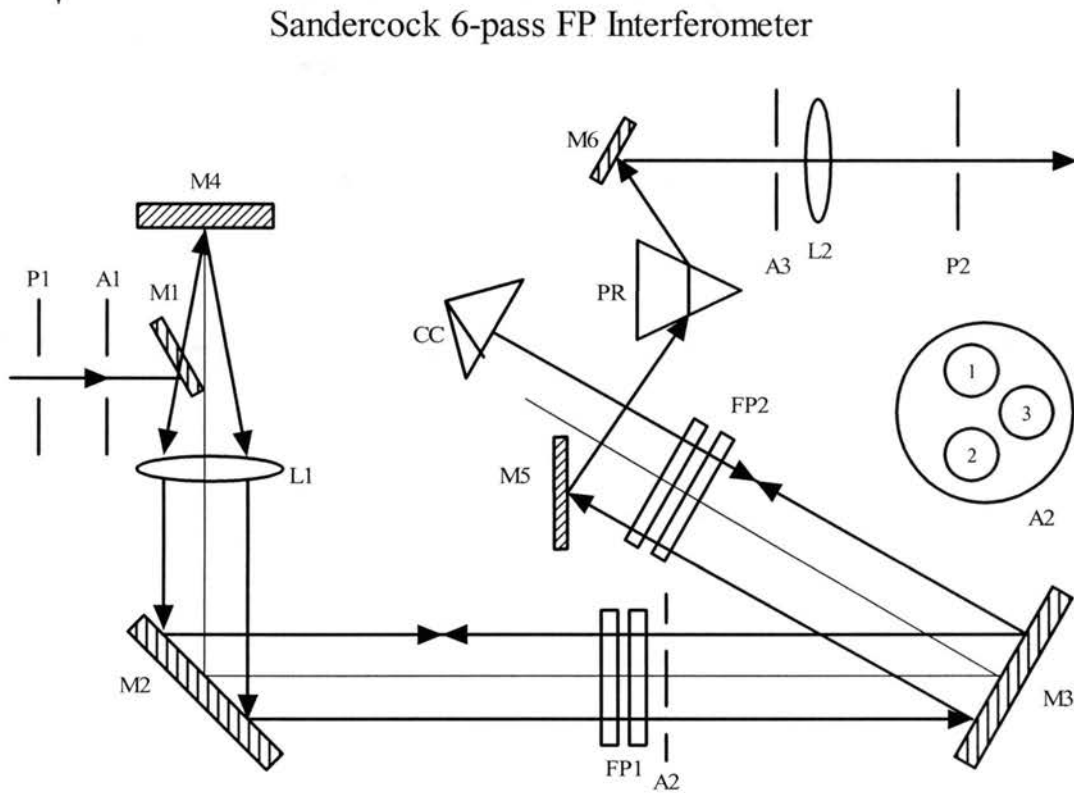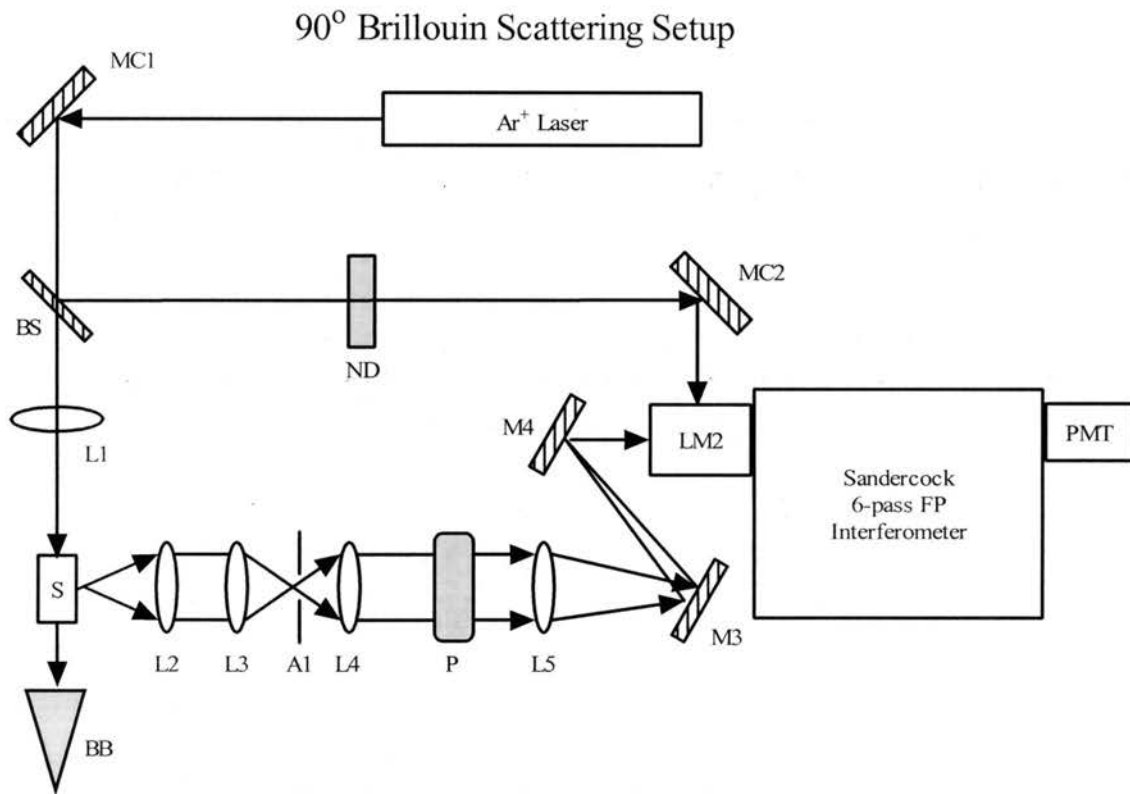
Fig.14. Right-angle BLS experimental setup and Sandercock 6-pass TSFPI

The longitudinal and transverse acoustic peaks are curve-fitted separately using Gaussian lineshape functions and the mean values for peaks shifts and integrated intensities on Stokes and anti-Stokes sides were obtained by Peak Fit 4.0 *Jandel Scientific* software. The Brillouin scattered light was collected at right angle ($\theta = 90°$) with respect to the direction of the incident light. During the experiments the incident laser power was fixed at 230 mW. The separation between first pair of mirrors of TFPI was set at 3 cm corresponding to 1.67 cm^{-1} free spectral range (FSR) and finesse ~ 40. The most accurate method of measuring elastic constants is based on the use of ultrasonic sound velocity measured by the Brillouin scattering experiment [66].

The EDSMAS glass is the medium where absorption at the 514.5 nm is not negligible due to $^7F_0 \rightarrow {}^5D_1$ transition of Eu^{+3} centered at ~ 529 nm [5]. Thus, the actual Brillouin scattering intensities I_B for longitudinal and transverse acoustic modes will be characterized by the known attenuation relation $I_B = I_0 \exp(-\alpha_a L)$, where the total propagation distance passed by light inside the sample $L = L_i + L_s$ is the sum of the distance traveled by the incident L_i and scattered L_s light in the sample (see fig. 15), α_a is the absorption coefficient of the sample at 514.5 nm, I_0 is the absorption-free scattering intensity. Thus, taking into account the absorption, the absorption-free Pockel's photoelastic constants P_{12} and P_{44} of (2.1.19) will be adjusted to:

$$P_{12} = \left(\frac{\rho I_L(VV) \cdot \exp(\alpha_a L)}{\rho^0 I_L^0(VV) \cdot \exp(\alpha_a L)} \right)^{1/2} \frac{\omega_L}{\omega_L^0} \left(\frac{n^0}{n} \right)^5 \left(\frac{n+1}{n^0+1} \right)^2 P_{12}^0, \qquad (4.2.1a)$$

$$P_{44} = -\left(\frac{\rho I_T(VH) \cdot \exp(\alpha_a L)}{\rho^0 I_T^0(VH) \cdot \exp(\alpha_a L)} \right)^{1/2} \frac{\omega_T}{\omega_T^0} \left(\frac{n^0}{n} \right)^5 \left(\frac{n+1}{n^0+1} \right)^2 |P_{44}^0|, \qquad (4.2.1b)$$
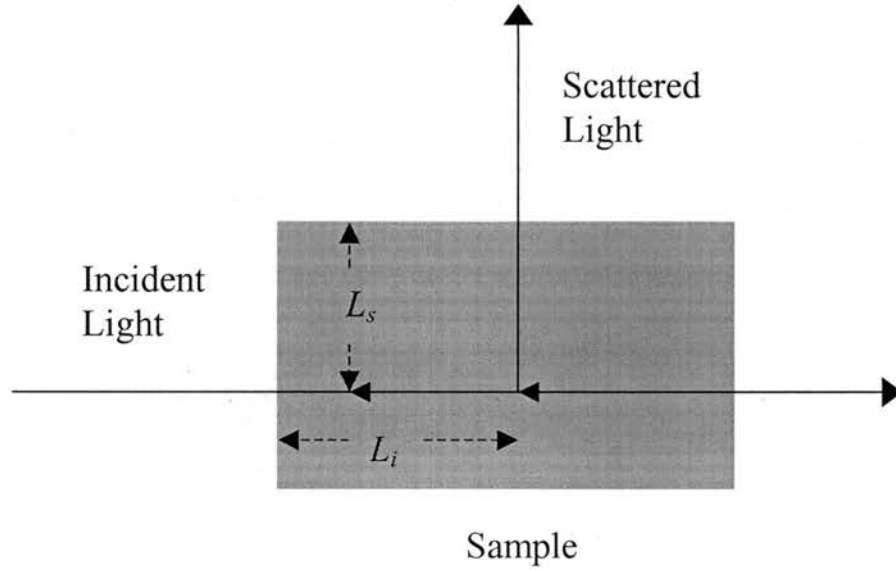
Fig. 15. Top view of the sample showing the distance traveled by the

incident and scattered light

The fused silica was chosen as a reference glass sample for which the values of P_{12}^0 and P_{44}^0 are taken from Ref. [46]. Integrated Brillouin intensity measurements at fixed L_s but variable L_i were performed to determine the absorption-free scattering intensity I_0 and the absorption coefficient α_a. A linear regression routine was used to extrapolate the intensity relation to obtain I_0 and α_a. Fig.16 shows the experimental data and linear fitting results of the Eu3.90 sample in a semi-log plot. By performing *HH*- polarization BLS measurements we were able to deduce that P_{12} and P_{44} absolute values for all our glasses have positive and negative values, respectively, which is taken into an account in (4.2.1). This observation takes place for most of the oxide glasses [18, 45, 46, 69, 89].
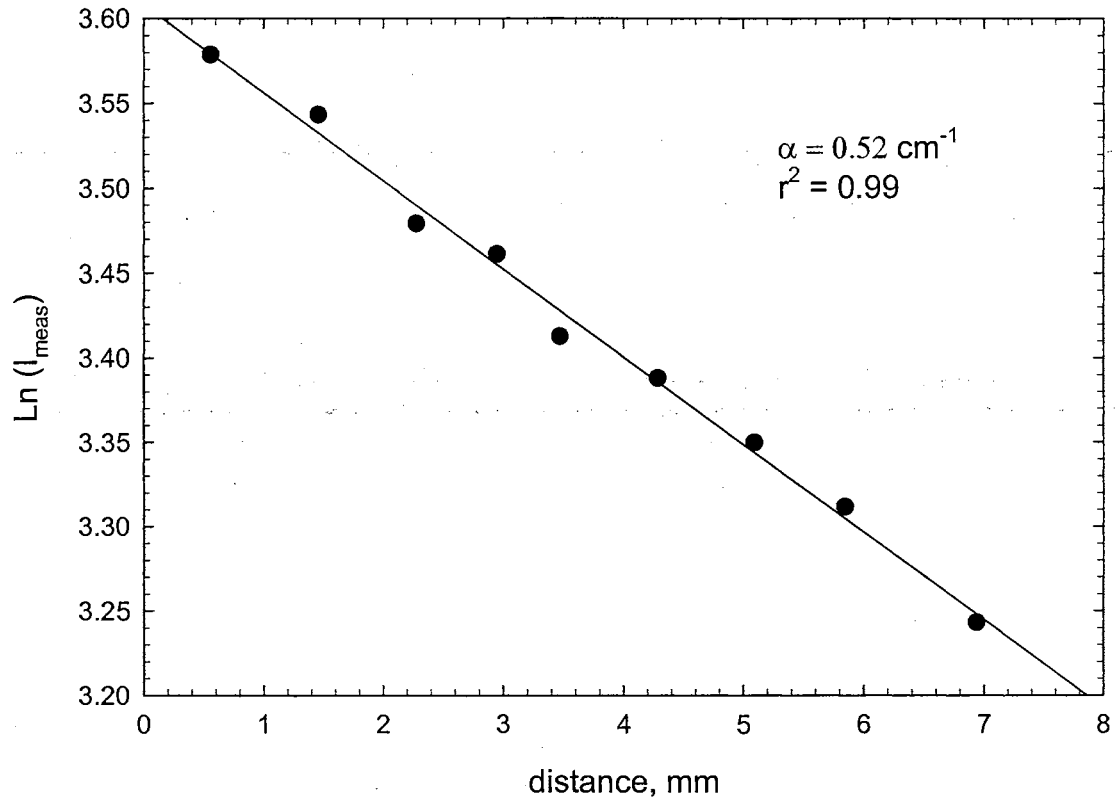
Fig.16. Regression of measured absorption coefficient α_a of

the Eu3.90 sample using BLS. L_{inc} = varied, L_{scat} = fixed

4.3. RLS Experiment and Procedures

Light of 457.9 nm wavelength from an Ar^+ laser was chosen to be far from resonance for Eu^{3+} ions, thus lowering the absorption and making the effect of fluorescence on the Raman spectrum negligible [90]. The samples under study were cut into a parallelepiped shape and polished using cerium oxide polishing material. A 250 mW laser beam was directed into the transparent glass sample (s), placed on a horizontal adjustable holder, and scattered light was observed at right angles with respect to the incident light beam direction. All unpolarized Raman scattering spectra were taken at 0.3 cm^{-1}/ sec scanning rate using *Instrument SA, Inc. RAMANOR* double grating *U-1000* monochromator. The spectrometer output signal was sent to PMT cooled with thermoelectric cooler. The PMT output is processed with photo-counting electronics consisting of a preamplifier-discriminator (PAD) and a count rate meter. The obtained Raman spectra are downloaded to PC for further curve-fitting using Peak Fit 4.0 *Jandel Scientific* software. The RLS experiment block diagram is displayed in Fig 17. At the laser excitation wavelength of 457.9 nm with U-1000 monochromator using holographic grating with 1800 grooves/mm and four slits with the size of 200 μm, the instrumental resolution of 2.27 cm^{-1} was estimated.

4.4. Solid-State NMR Experiment and Procedures

All solid state NMR experiments were performed using a *Chemagnetics CMX-II* spectrometer probe (see Fig. 18). For Eu-series ^{27}Al and ^{29}Si NMR spectra were obtained at 7.07 Tesla (78.434 MHz, 59.800 MHz) with a 5 mm triple-resonance
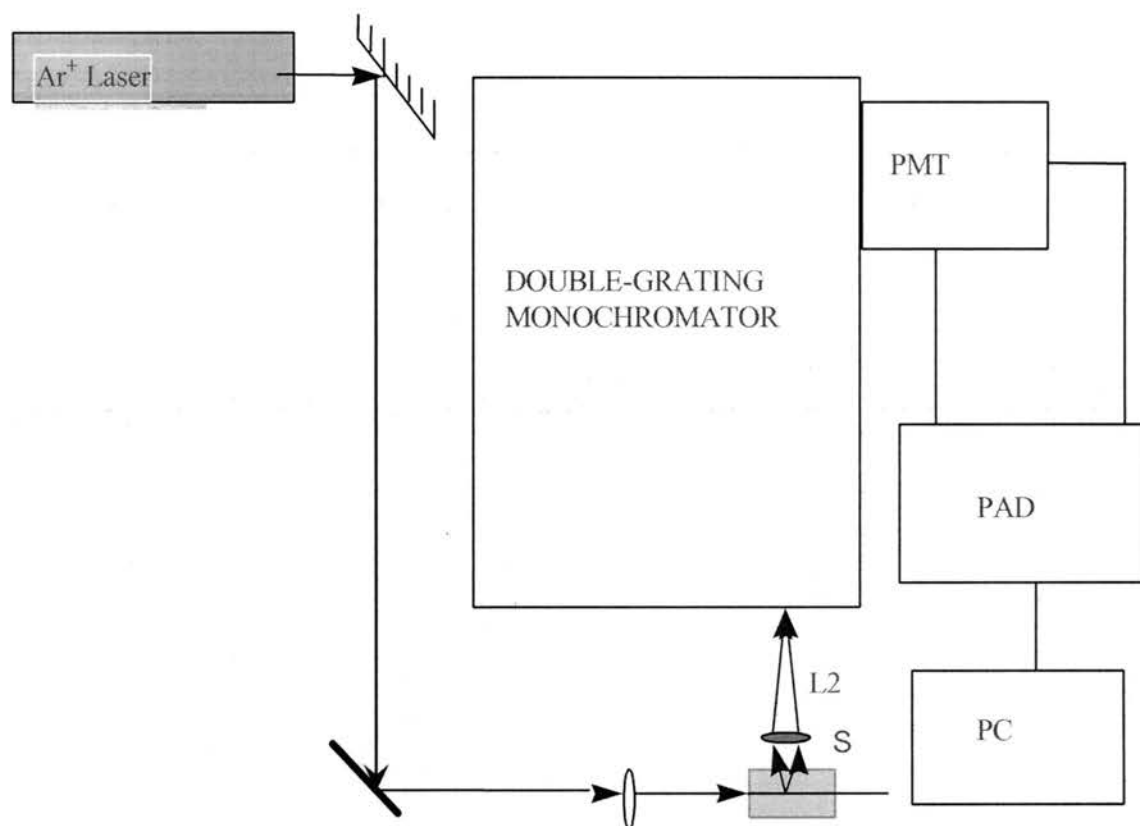
Fig. 17. Experimental RLS setup

Solid-State Nuclear Magnetic Resonance Spectrometer

Computer

B_0

Magnet

$54.74°$

B_0

MAS Probe Head

Console

Transmitter

Receiver

Probe

Compressed Air Supply

MAS Speed Controller

Bearing

Tach   Drive

Chemagnetics CMX-II

^{27}Al Frequency   78.435 MHz

MAS Spinning Speed   8.0 kHz

Diodes   Filter

Diodes

Preamplifier
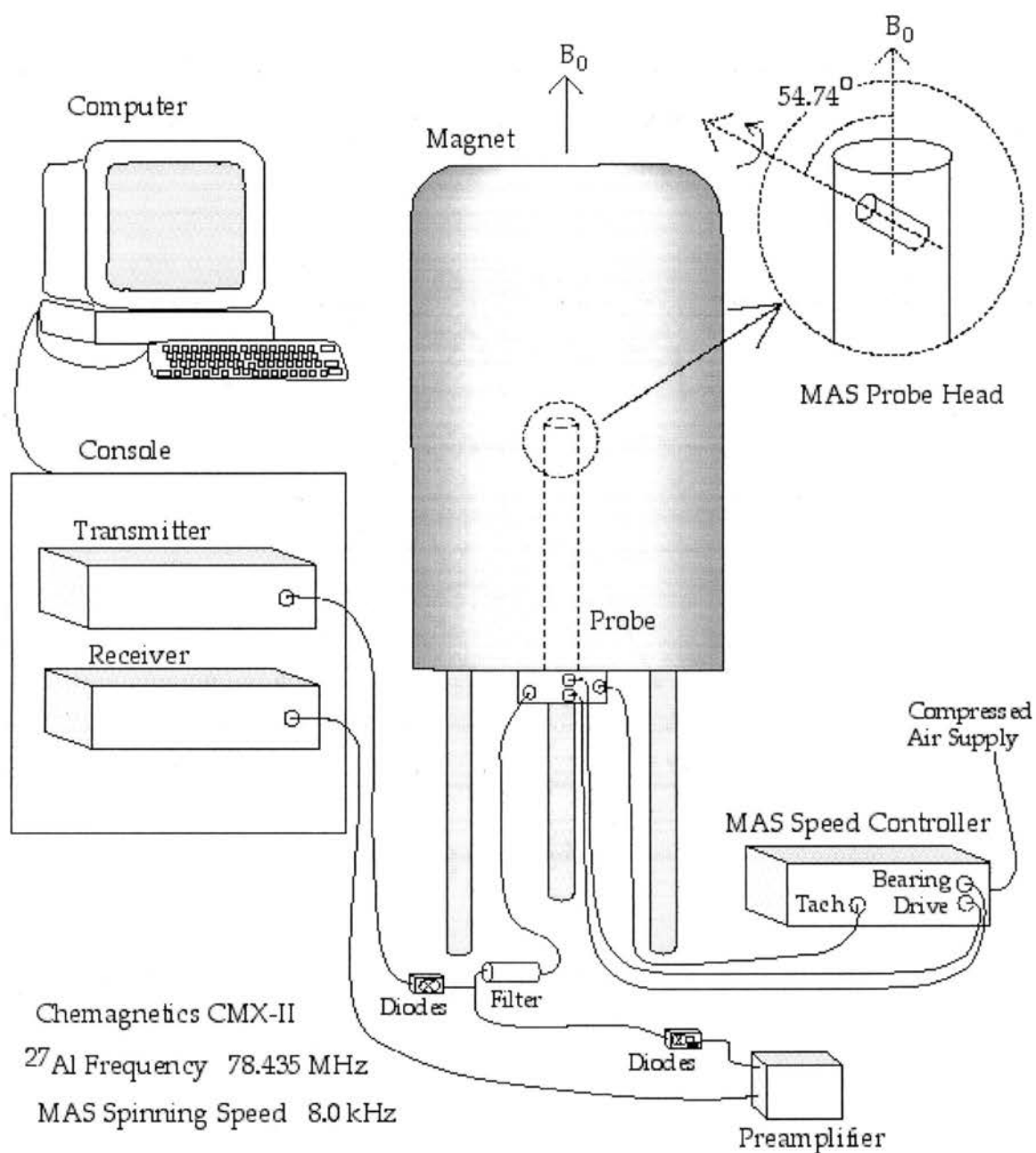
Fig.18. Solid-State NMR Spectrometer Chemagnetics CMX-II

magic-angle spinning (MAS) probe. ^{27}Al spectra were also obtained at 11.74 Tesla (130.183 MHz) with a 2.5mm MAS probe. The results of peak positions and FWHMs in the ^{27}Al MAS NMR spectra were obtained by fitting Gaussian line shapes to the spectra with fitting error ± 1 ppm. Finely ground powder samples were packed in cylindrical zirconia rotors with plastic drive tip, spacer, and cap. For Eu-series the pulse widths used to calculate the radiofrequency field strengths at 7.07 Tesla were measured for ^{27}Al on a liquid sample of 1M aqueous $Al(NO_3)_3$ and for ^{29}Si on solid sodium-3-trimethylsilylpropionate (TMS). Measurements of ^{27}Al spin relaxation time constants (T_1 and T_2) for the central transition were made at 78.434 MHz on samples spinning at 10.000 ± 0.005 kHz using the inversion recovery (π_s-τ-($\pi/2$) $_s$-acquire) pulse sequence for T_1 and spin-echo (($\pi/2$) $_s$- τ-π_s-τ–acquire) pulse sequence for T_2, where the subscript "s" signifies a solid-state pulse width. Following Haase and coworkers [91, 92] a weak radiofrequency field strength (6.0 kHz) was used to selectively excite the central transition. The ($\pi/2$)$_s$ pulse width (14μs) was 1/3 of the liquid-state $\pi/2$ pulse width, demonstrating selective excitation of the central transition [93]. A background ^{27}Al MAS spectrum of $Na_2C_2O_4$ for each value of τ (for both sequences) was obtained, and these spectra were subtracted from the corresponding spectra of the glasses. A delay of 1 s between scans was used, and 1200 scans were averaged for each τ value for ^{27}Al T_2 measurements. Synchronous sampling [94] was achieved by selecting τ values such that the entire length of the pulse sequence prior to acquisition corresponded to an even integral number of rotor periods. ^{27}Al T_1 measurements were made with a delay of 2s between scans and 2000

scans averaged. Measurements of ^{29}Si T_2 utilized the spin-echo pulse sequence with synchronous sampling and a $\pi/2$ pulse width of 9μs. Pulse delays depended upon the sample and are provided in Section 5.1.4.

For Al- and Na-series the MAS NMR spectra were obtained at 7.07 Tesla with a with 5 mm diameter rotors packed with glass powder samples finely ground with a ceramic mortar and pestle. ^{27}Al spectra (78.435 MHz) were measured using triple-resonance probe and spun at 8.000 ± 0.005 kHz. These spectra are the result of 1024 averaged scans with a 0.5 s delay and 3.2 μs pulse width, which is a 90° pulse width measured on a solid sample. The spectra were externally referenced to 1M aqueous Al(NO$_3$)$_3$. ^{29}Si spectra (59.8 MHz) were obtained with a double resonance probe and spun at 6.000 ± 0.005 kHz. These spectra are the result of 500 averaged scans for the Al0, Al2.96 and Al5.92 samples, and 700 scans for the Al8.88 and Al14.80 samples of Al-series. More scans were taken for the latter two samples because there was not enough material to fill the rotor. The resulting scans had 120 s delay and 10 μs pulse width, which is a 90° pulse width measured on TMS. ^{23}Na MAS NMR spectra (79.618 MHz) are the result of 1024 averaged scans with a 0.5 s delay and 2.8 μs pulse widths. All pulse widths represent 90° pulses measured on the solid samples. ^{23}Na spectra were externally referenced to 1M aqueous NaCl.

4.5. Refractive index and density measurements

The refractive indexes of EDSMAS glasses were measured with the accuracy of less than $\pm$ 0.5 % using an enhanced version of the Brewster's angle experiment [95]. The technique requires one to have polished surfaces of glasses and can be done for both

transparent and opaque samples. The density of each glass sample was measured using Archimedes's method with an error of less than ± 1 %. The samples were immersed into the distilled water, the density of which is very well known. The density was determined as the ratio of the glass sample mass to the volume of the displaced distilled water.

CHAPTER V

EXPERIMENTAL RESULTS AND DISCUSSION

5.1. Eu-SERIES

5.1.1. Elastic parameters

The results of BLS measurements for Eu-series are shown in Table 3. Measured Brillouin shifts (ω_L, ω_T), refractive indices n, density ρ and absorption coefficients are used to calculate elastic constants (C_{11}, C_{44}) using (2.1.10), Young's modulus E, bulk modulus B and Poisson's ratio σ using (2.1.12). The large decrease in such elastic parameters as C_{11}, C_{44}, E and B demonstrated in Fig. 19(a) with an initial introduction of rare earth ions into our glass is attributed to the rapid decrease in the material's density. But the following increase of the doping level of europia up to 8.11 mole % yields structural rearrangement so that the enhancement in the values of these elastic parameters result in the increased hardness of the EDSMAS glass. This observation is in agreement with the increase of the measured values of elastic moduli with the increasing rare-earth ions for europium [26] and yttrium [96] aluminosilicate glasses.

The hardness of materials is not simply related to microscopic forces from the lattice dynamics point of view. The coordination of atoms plays a very important role in the elastic behavior of materials. Husson *et al.* has studied the relationship of intermolecular forces and elastic constants using α-quartz and α-alumina [97]. Their results show that very rigid covalent Si-O bonds do not directly contribute to the elastic constants in α-quartz, while the high coordination of Al sites presents a high weight to elastic constants in α-alumina. This role of the coordination of atoms in material hardness is corroborated

Sample ID	ρ (g/cm^3)	ω_L (cm^{-1})	ω_T (cm^{-1})
Eu0	2.72 ± 0.05	0.797 ± 0.003	0.479 ± 0.002
Eu0.73	2.48 ± 0.02	0.797 ± 0.003	0.476 ± 0.003
Eu1.26	2.61 ± 0.02	0.800 ± 0.003	0.478 ± 0.003
Eu3.90	2.94 ± 0.03	0.807± 0.003	0.476 ± 0.003
Eu5.26	3.12 ± 0.03	0.812 ± 0.003	0.475 ± 0.003
Eu8.11	3.33 ± 0.03	0.812 ± 0.003	0.469 ± 0.003
Fused Silica	2.21	0.804	0.506

Sample ID	C_{11} (GPa)	C_{44} (GPa)	E (GPa)	B(GPa)	σ
Eu0	88.1 ± 1.1	31.8 ± 0.4	77.4 ± 1.0	45.7 ± 0.6	0.218 ± 0.002
Eu0.73	81.8 ± 0.7	29.2 ± 0.4	71.4 ± 0.8	42.9 ± 0.2	0.222 ± 0.002
Eu1.26	85.7 ± 0.7	30.6 ± 0.4	74.8 ± 0.8	44.9 ± 0.2	0.222 ± 0.002
Eu3.90	94.4 ± 1.1	32.9 ± 0.5	81.1 ± 0.9	50.5 ± 0.4	0.233 ± 0.002
Eu5.26	99.7 ± 1.1	34.1 ± 0.5	84.6 ± 1.0	54.2 ± 0.4	0.240 ± 0.003
Eu8.11	100.9 ± 1.0	33.7 ± 0.5	84.2 ± 1.0	56.0 ± 0.3	0.249 ± 0.003
Fused Silica	79.6	31.5	73.9	37.6	0.174

Table 3. Calculated elastic constants C_{11}, C_{44}, Young modulus E, bulk modulus B and Poisson ratio σ of Eu-series based on the measured values of density ρ and Brillouin shifts ω_L, ω_T.
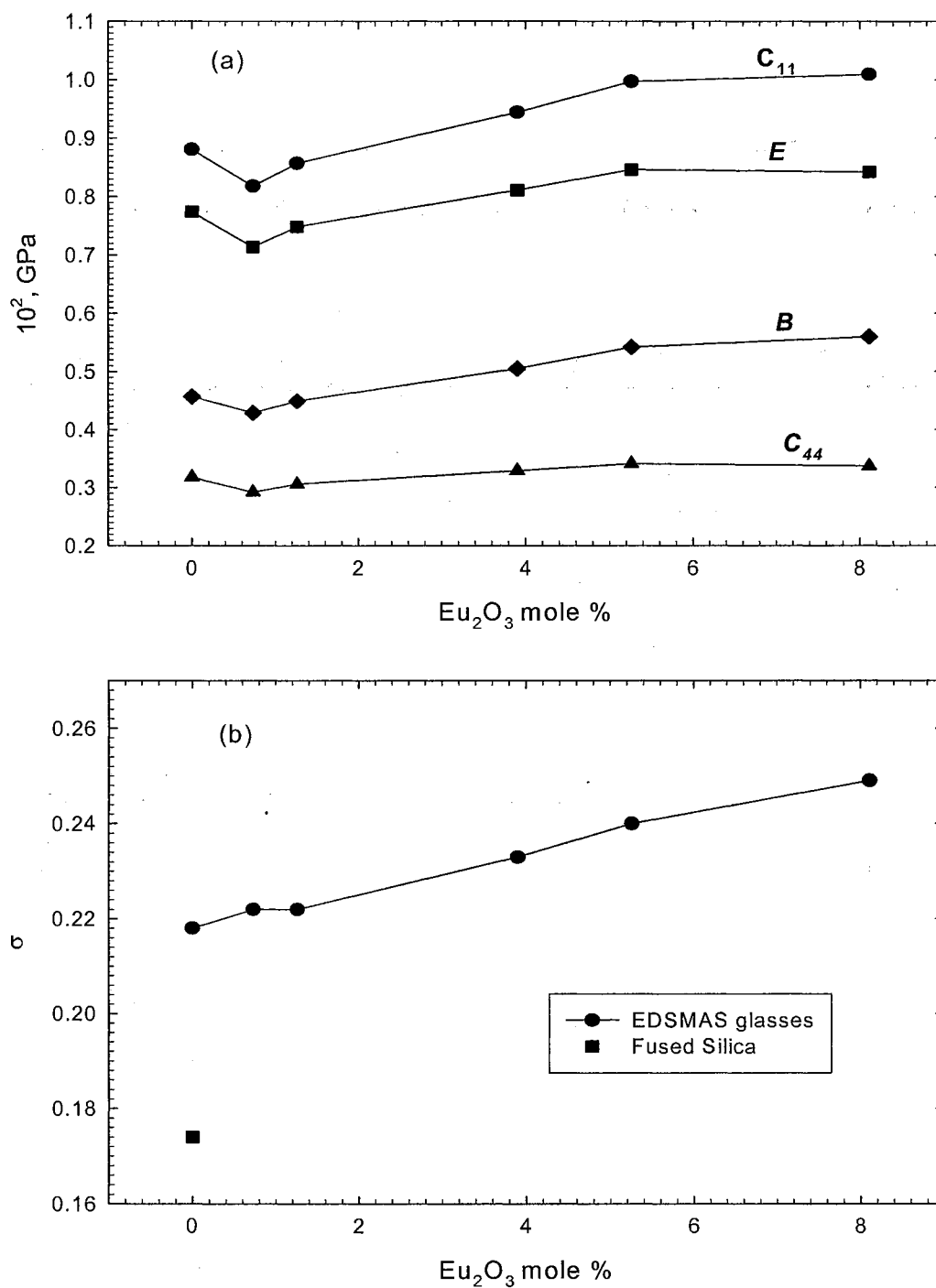
Fig.19. (a) Compressional C_{11}, shear C_{44}, Young E and bulk B moduli

(b) Poisson ratio versus Eu_2O_3 mole%

by the results of neutron scattering [98] and 2-D dynamic angle spinning NMR [99]. These studies indicate that in binary silicate glasses, the network modifiers (Mg^{2+}, Ca^{2+}, or K^{+}) are highly coordinated. Tanabe et al. [26] found that the coordination number of Eu^{3+} ions in the Eu^{3+} doped alumina silicate glass ranges from 10 to 12 depending on the Eu^{3+} concentration from 10 to 40 mol%. Husson's model provides a possible explanation to our results. When rare-earth ions are introduced into glasses, they break the Si-O-Si and Si-O-Al covalent bonds and cause the formation of more Si-NBO links while reducing the free space in the glass. The reduction of free space is due to the fact that the rare-earth ion has the largest atomic size in our samples [100], i.e. $r_{(Eu)} = 1.85$ Å $> r_{(O)} = 1.38$ Å $> r_{(Na)} = 1.02$ Å $> r_{(Al)} = 0.39$ Å $> r_{(Mg)} = 0.34$ Å $> r(Si) = 0.26$ Å. Therefore, as the rare-earth concentrations increase, more free space is captured and the average coordination in the glass increases. Consequently, the elastic constants C_{11} and C_{44} increase, as do the Young's and adiabatic bulk moduli. As another proof, the activation energy E_A of sodium modifiers obtained from the ionic conductivity measurements of EDSMAS glass samples is observed to increase with Eu^{3+} doping [6]. E_A is proportional to the strain energy E_s, which in turn is proportional to the shear modulus C_{44} [101]. Therefore, E_s and thus C_{44} should increase with increasing Eu^{3+} content. The increase of E_s and C_{44} is also in agreement with the decreasing of the doorway size between adjacent interstices [101] due to doped europiums having largest ionic size in the glass and blocking the diffusion of sodium ions. B.J. Porter [12] stated that although more fragmental, the silica network is held together through strong mainly ionic interactions with the lanthanide ions. Eu^{3+} ions have higher binding energy with oxygen anions than Na^{+} and Mg^{2+} modifier ions because rare-earth ions have higher field strength than their

divalent and monovalent counterparts [17]. Thus, the effect of high field strength of Eu^{3+} ions overcomes the depolymerization of the silica network, which results in increased hardness of the material. The increase of the glass molar mass as will be seen later in Table 4 also supports the increase of the hardness and is in agreement with the previous studies of rare earths as modifier ions in oxide glasses [102].

The larger values of the Poisson ratio σ, compared with fused silica as shown in Fig. 19(b), imply that the overall bonding in the glass becomes more ionic [66, 103, 104]. The Judd-Ofelt intensity parameters Ω_2 and Ω_6 obtained from absorption measurements [105], performed on the Eu^{3+} doped SMAS glass samples, increase as Eu^{3+} concentration increases. Ω_2 increases with the enhancement of the polarity or the asymmetry of Eu^{3+} sites. Ω_6 increases with the diminishing in the Eu-O bond covalence [106, 107]. Thus, from the behaviors of Ω_2 and Ω_6, we can see that the bond polarizability of Eu-O increases and the Eu-O bond becomes more ionic as the Eu^{3+} concentration increases. The estimated total number of NBOs (see Table 1(a)) increases with the increase of rare-earth doping level due to depolymerization of silica network characterized mostly by the formation of larger number of number Si-NBO bonds. The increase of the refractive index n also supports the enhancement of σ. Thus, the unique combination of the increase in hardness and ionicity take place *simultaneously* with Eu^{3+} doping into soda magnesia aluminosilicate glass. This *combined* effect is quite possible since doped Eu^{3+} ions on one hand - replace low valence modifiers (Na^+, Mg^{2+}) and on the other – substitute high valence glass network formers (Si, Al).

5.1.2. Photoelastic constants

Based on calculated molar mass M of the EDSMAS glasses of Eu-series and measured values of P_{12}, P_{44}, n, ρ we calculated LLE, LE, AE, α and G using (2.1.20), (2.1.21), (2.1.23) and (2.1.24). The results of these calculations along with the measured values of photoelastic constants P_{12} and P_{44} are listed in Table 4 and plotted in Figs. (20-22) versus Eu_2O_3 mole %. The values of the measured absorption coefficient α_a used for calculating P_{12} and P_{44} are listed in Table 4 as well. For concentrations up to 5.26 mole % of Eu_2O_3, we observed a monotonic decrease of P_{12}, P_{44}, LE and AE because of the increase in the polarizability α, the increase in density ρ and the increase in the refractive index n. However, LLE gets stronger because the increase in molar mass of the EDSMAS glass is predominant as compared to changes in ρ, n and α. The increase in the polarizability is in agreement with Poisson's ratio data shown in Fig. 19(b). The correlation integral G diminishes because of the presence of a strong r^{-4} dependence in the integrand of this integral in (2.1.22). It has been shown that the Eu-O bond length is larger than the bond length of each glass network former (Si, Al) and modifier (Mg, Na) linked to an oxygen [108, 109]. Therefore, it is this difference in bond lengths which we think is responsible for the decrease of the correlation integral G. From Fig. 22 we see that $|LE| < |AE| < LLE$, i.e. the largest contribution to P_{12} values comes from the first term, Lorentz-Lorentz effect (LLE), i.e. the term which accounts for the change of refractive index due to local density changes accompanying the light induced strain. In addition, the lattice effect (LE) is smaller than the atomic effect (AE) because it is easier to distort individual atomic sites than the group of atoms (lattice). At 8.11 mole% of

Eu_2O_3 we have a rapid decrease of the *LLE* value which is attributed to the significant enhancement of the polarizability.

Sample ID	α_a (cm^{-1})	P_{12}	P_{44}	M (g/mole)	n
Eu0	0.59±0.10	0.251±0.009	-(0.054±0.004)	59.251	1.528 ± 0.005
Eu0.73	0.38±0.10	0.251±0.009	-(0.055±0.004)	61.389	1.515 ± 0.005
Eu1.26	0.76±0.10	0.251±0.009	-(0.056±0.004)	62.938	1.524 ± 0.005
Eu3.90	0.52±0.10	0.249±0.008	-(0.056±0.004)	70.665	1.554 ± 0.005
Eu5.26	0.69±0.10	0.248±0.008	-(0.057±0.004)	74.645	1.568 ± 0.005
Eu8.11	0.83±0.10	0.188±0.005	-(0.042±0.003)	82.988	1.610 ± 0.005
Fused Silica	0.04	0.279	-0.078	60.086	1.462

Sample ID	α (10^{-23} cm^3)	G (10^{23} cm^3)	*LLE*	*LE*	*AE*
Eu0	0.153±0.007	3.98±0.20	0.615±0.007	-(0.065±0.001)	-(0.119±0.001)
Eu0.73	0.170±0.008	3.66±0.18	0.613±0.007	-(0.064±0.001)	-(0.119±0.001)
Eu1.26	0.168±0.008	3.69±0.18	0.615±0.007	-(0.065±0.001)	-(0.119±0.001)
Eu3.90	0.174±0.009	3.47±0.17	0.627±0.006	-(0.069±0.001)	-(0.124±0.001)
Eu5.26	0.175±0.009	3.43±0.17	0.636±0.006	-(0.070±0.001)	-(0.127±0.001)
Eu8.11	0.226±0.011	2.29±0.12	0.550±0.003	-(0.076±0.001)	-(0.117±0.001)
Fused Silica	0.150	5.270	0.678	-0.057	-0.134

Table 4. Calculated values of *LLE, LE, AE,* α and *G* of Eu-series based on the measured values of absorption coefficient α_a, photoelastic constants P_{12} and P_{44}, index of refraction *n*, density ρ and calculated molar mass *M*.
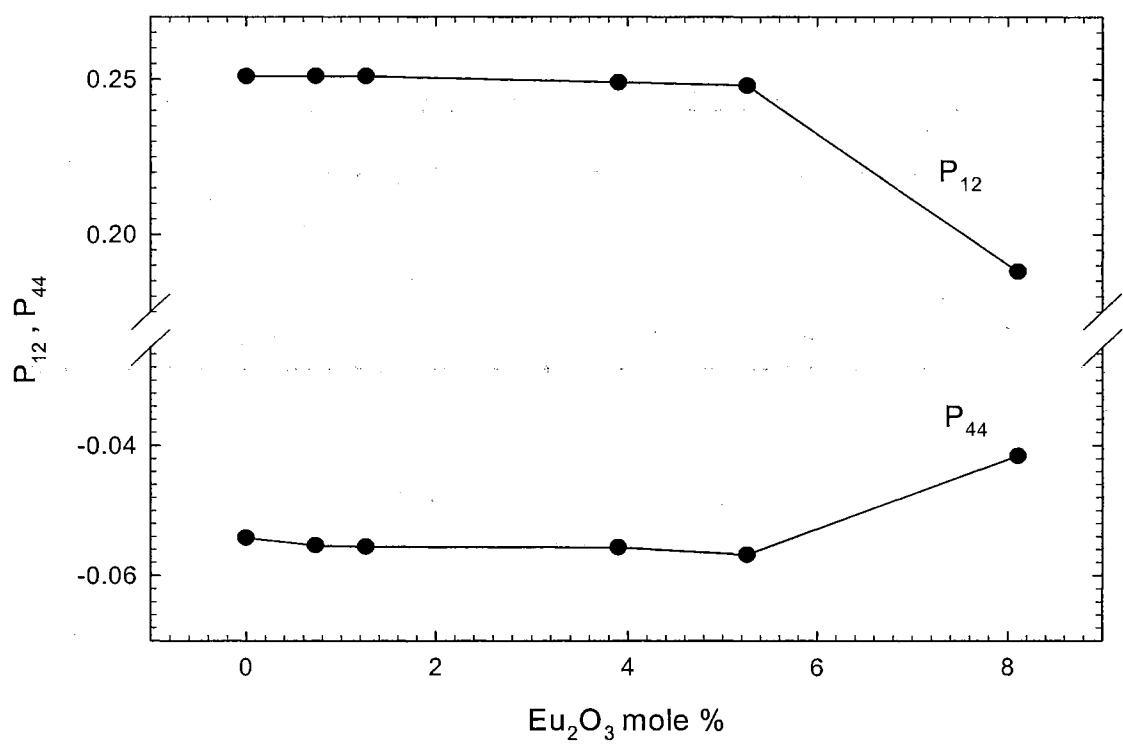
Fig.20. Photoelastic constants P_{12} and P_{44} versus Eu_2O_3 mole%
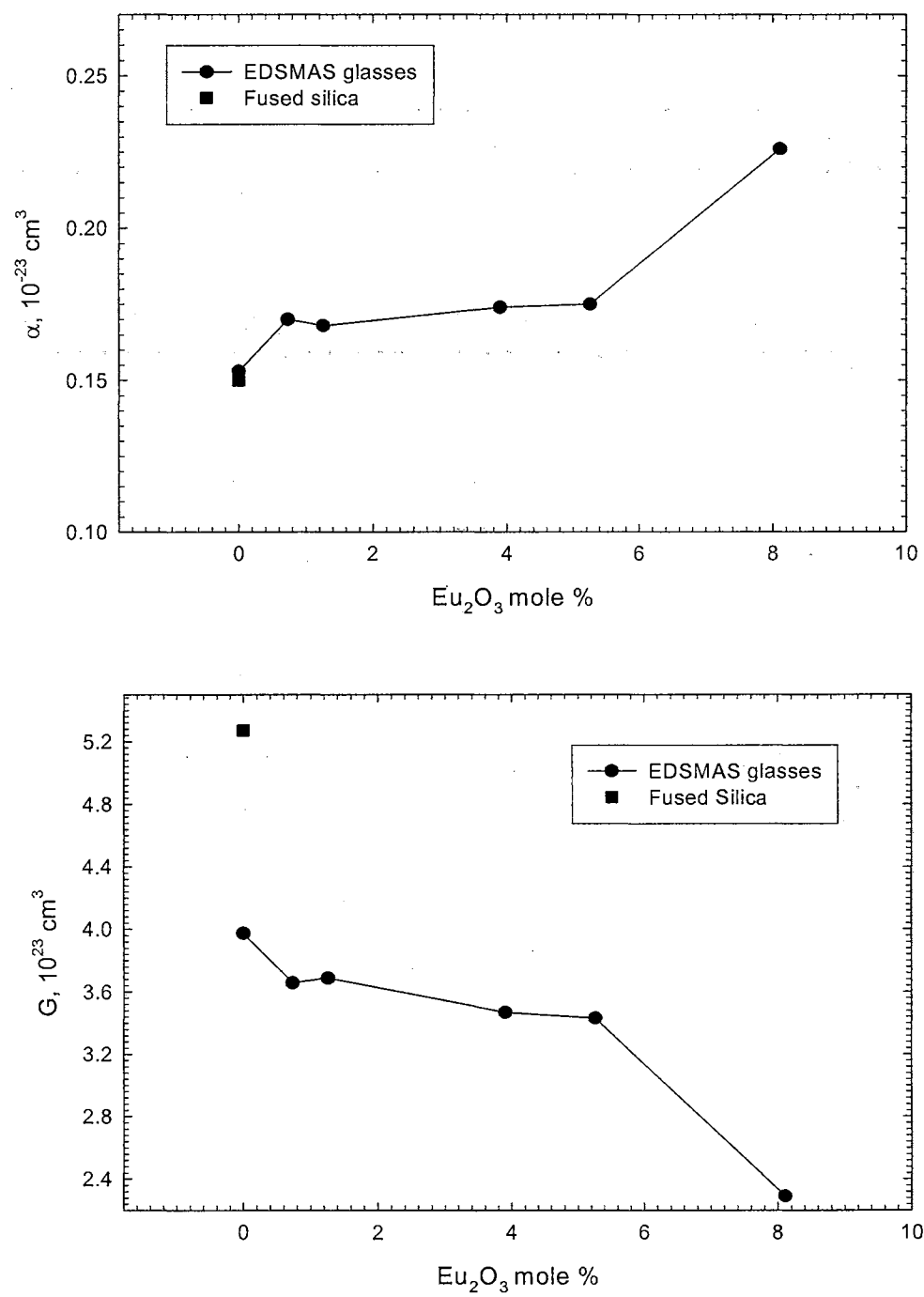
Fig.21. Polarizability α and correlation integral G versus Eu_2O_3 mole%
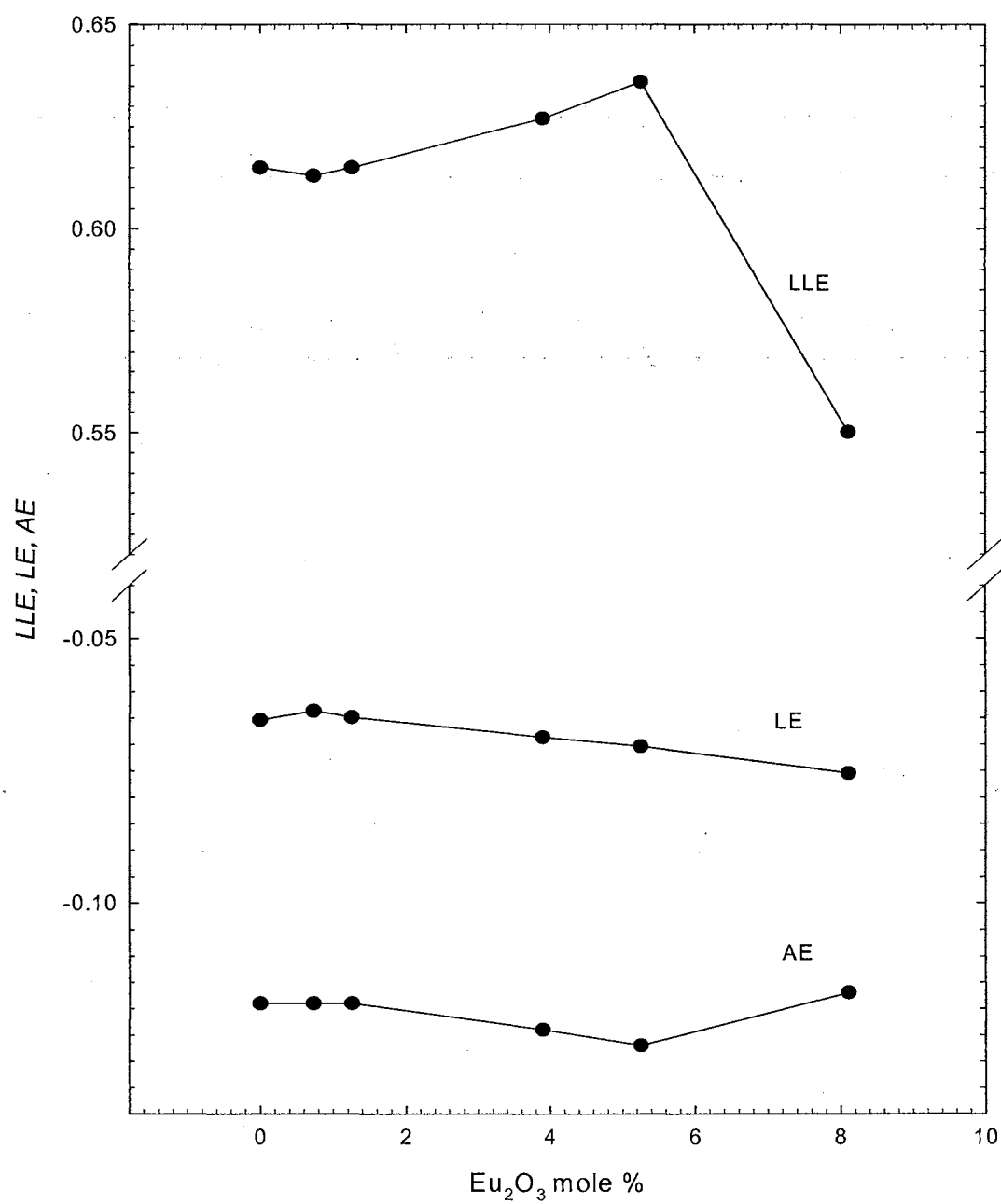
Fig.22. Lorentz-Lorentz effect (*LLE*), lattice effect (*LE*) and

atomic effect (*AE*) versus Eu_2O_3 mole%

5.1.3. RLS Spectroscopy

Unpolarized Raman spectra for the EDSMAS glasses with various Eu_2O_3 concentrations are shown in Fig. 23. The Raman peak intensities are a function of not only the number of vibrating modes but also bond polarizabilities, therefore only the relative changes in abundances of various Q^n species with varying Eu content can be deduced from changes in the Raman peak intensities. In the high-energy Raman spectrum of the rare earth-free glass (Eu0) we have partially resolved peaks at 1100 cm^{-1} and 970 cm^{-1}, attributed to the existence of Si-NBO stretching vibrations in Q^3 and Q^2 silicon tetrahedral groups, respectively [110]. The NBOs formed in Eu0 glass are due to Na^+ and Mg^{2+} cations, i.e. Q^3 and Q^2 species in this case are represented by Q^3-Mg, Q^3-Na and Q^2-Mg, Q^2-Na units. The 1100 cm^{-1} band is dominant indicating preponderance of Q^3-Mg, and Q^3-Na species in this glass sample. With the increase of the rare-earth content at the expense of the glass host, the Raman envelope at (900-1240) cm^{-1} shifts toward lower wave-numbers and the band at 970 cm^{-1} gradually merges with the band at 1100 cm^{-1}. The shift toward lower wave numbers and change in the shape of the (900-1240) cm^{-1} band with increasing Eu_2O_3 content can be attributed to an increase in the Q^3-Eu species at about 1030 cm^{-1} [118, 79] at the expense of Q^3-Na and Q^3-Mg species, as well as an increase in the contribution from Q^2 species and the development of contributions from Q^1 (~ 900 cm^{-1}) and Q^0 (~ 850 cm^{-1}) [110]. Thus, the net effect of the increase of the rare-earth ion content is the appearance and gradual increase of depolymerized SiO_4 units in EDSMAS glass. Rare earth ions incorporated in aluminosilicate glasses act as network modifiers to form NBOs rather than $AlO_{n/2}^{(n-3)-}$ macroanions [111]. We have estimated the fraction of all NBO atoms ($R_{Total NBO}$) and the fractions of NBOs associated with Na
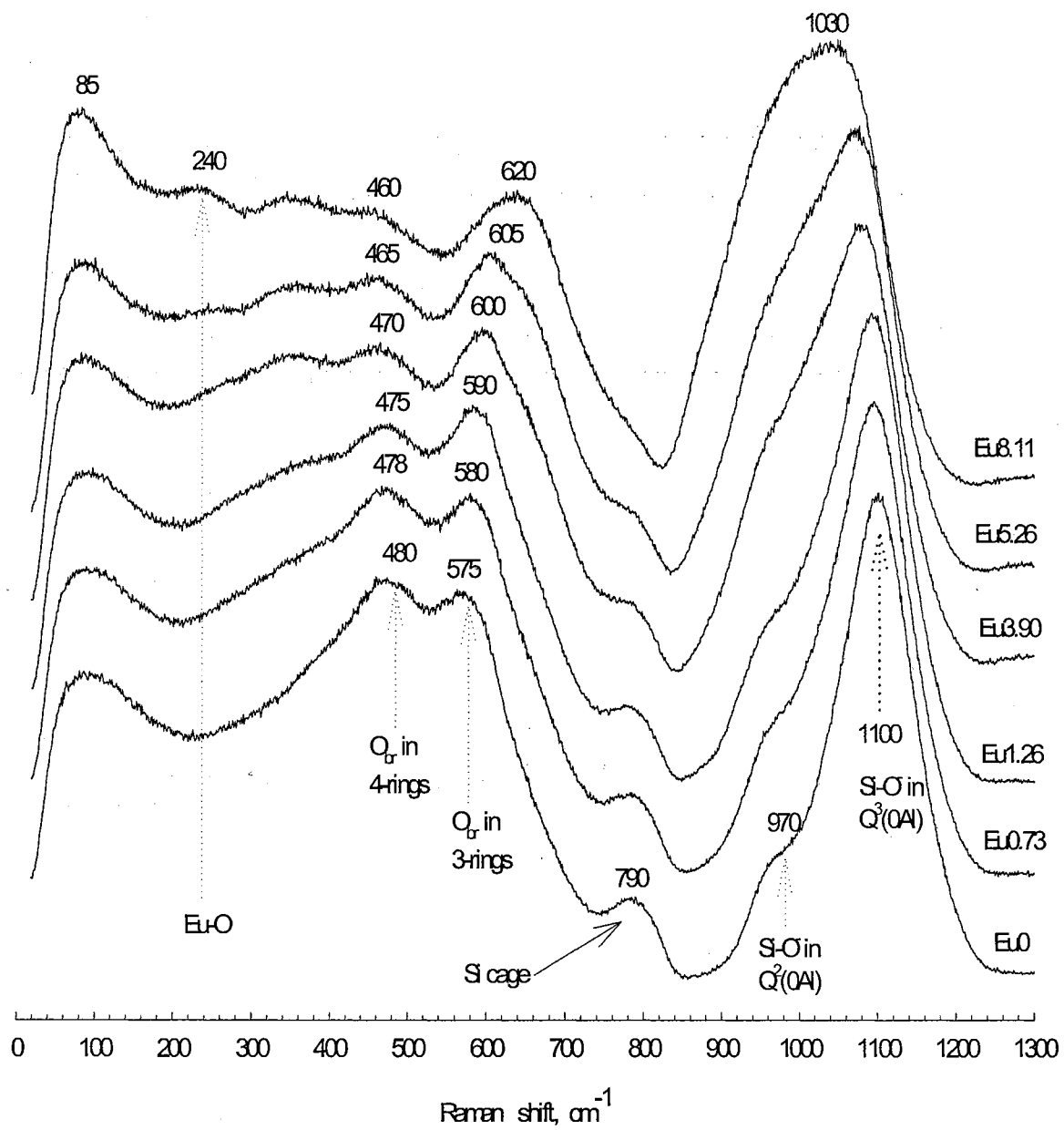
Fig. 23. Raman spectra of EDSMAS glasses of Eu-series

75

and Mg (R_{Na+Mg}) and with Eu ions (R_{Eu}). These values are shown in Table 1(a). In the estimation of the relative NBO amounts [36] it was assumed that Na^+, Mg^{2+} and Eu^{3+} ions in EDSMAS glass create one, two and three NBOs, respectively, and one Na^+ ion is needed to compensate the charge of one $[AlO_4]^-$ complex. Up to 5.26 mole % of Eu_2O_3, $R_{Na+Mg} > R_{Eu}$, but at 8.11 mole % of Eu_2O_3, R_{Eu} exceeds R_{Na+Mg}. Below 8.11 mole % of Eu_2O_3, the peak at ~ 1100 cm^{-1} representing Q^3-Na and Q^3-Mg remains dominant, but at 8.11 mole % of Eu_2O_3 this peak shifts closer to the expected position of Q^3-Eu at ~1030 cm^{-1}. The trend in the estimated total ratio of NBOs vs. Eu_2O_3 content ($R_{Total\ NBO}$) in Table 1(a) also agrees with the increase in amplitude of the Raman spectra at 970 cm^{-1} and below, attributable to an increase in Q^n with n ≤ 2. As the number of different Q^n species increases, the local structure of the EDSMAS glass becomes not only more depolymerized but also more disordered, which is in agreement with previous studies of rare-earth aluminosilicate glasses [20, 22, 30] and rare-earth alkaline silicate glasses [112]. This interpretation of the spectra is also in agreement with the explanation given by Brawer and White [113], who suggested that high field strength modifier ions lead to highly disordered structures, with a broad distribution in the types of SiO_4 tetrahedra.

The frequency increase of the 575 cm^{-1} Raman band assigned to the bridging oxygen breathing mode in both three-member pure silicate- [114] and (Si,Al)-rings [115, 34] with increasing Eu^{3+} resembles the one reported by Krol and Smets [79] with the increase of high field strength ions (Tl^+, In^{3+}, Sc^{3+}, Y^{3+} and La^{3+}) in sodium silicate glass. Since Eu^{3+} ions have larger ionic radii then Na^+ and Mg^{2+} ions, the relative increase of Eu^{3+} concentration with respect to the concentrations of Na^+ and Mg^{2+} ions leads to an increase in the formation of three-member rings, as a result of the formation of larger

cages in the glass structure [34], explaining the increase in the height of the 575 cm^{-1} with respect to the height of 480 cm^{-1} band. The latter band is similarly attributed to the bridging oxygen breathing mode in both pure silicate- [114] and (Si,Al)-four member rings [115]. This peak shifts toward lower frequencies from 480 cm^{-1} to 460 cm^{-1} with the increase of europium doping into the EDSMAS glass. The peak at 790 cm^{-1} is assigned to the tetrahedral Si cage motions [34, 110].

The low frequency Raman spectrum exhibits a shoulder at around 240 cm^{-1}, which can be reasonably attributed to modes involving Eu-O vibrations, since Eu ions form much weaker bonds with oxygen and the mass of Eu is much higher than that of Si or Al. This Raman shift is consistent with that of Sm-O vibrations in samarium aluminosilicate glass [20] and various rare-earths in phosphate glasses [112]. From fluorescence spectroscopic studies, the presence of different structural sites occupied by europium ions was deduced for the EDSMAS glasses [5] and for the europium lithium calcium aluminosilicate glasses [116], which might explain the broadness of the 240 cm^{-1} band.

The height of the Boson peak at ~ 85 cm^{-1} gradually increases with respect to the band at 480 cm^{-1} band. It has been proposed that the polarizability and atomic mass of rare-earth ions, as well as the ionicity of their chemical bonding, are the origin of the Boson band amplitude enhancement with the increase of the rare earth (Pr^{3+}, Dy^{3+}, Nd^{3+}, Ce^{3+}) concentration [117]. Our BLS studies also indicate that the overall bonding in the EDSMAS glass becomes more ionic with the increase of Eu_2O_3 content [ref. 18, Chapter 5.1.1].

5.1.4. Solid-State NMR Spectroscopy

Fig. 24 shows ^{27}Al MAS spectra of the glasses, which display a single peak at ~ 55 ppm that broadens as the mole % of Eu_2O_3 increases, the fitted peak positions ω and full widths at a half of maximum (FWHM) $\omega_{1/2}$ are shown in this figure as well. This single peak can be assigned to aluminum coordinated with four oxygens, since the resonance frequency is similar to that seen for AlO_4 in lanthanum and yttrium aluminosilicate glasses [22]. The coordination of aluminum is generally four-fold in alkali aluminosilicate glass [32, 34] and alkaline earth aluminosilicate glass [33]. Both four-fold and six-fold coordination of aluminum have been observed in rare-earth (La, Ce, Eu) aluminosilicate glasses [21, 22, 26] and yttrium aluminosilicate glass [22, 30]. In comparing these observations to our detection of only Al(4) in the EDSMAS glasses, it may be important to consider that our concentrations of europium are below the rare earth or yttrium concentrations that yielded six-fold coordination (10 - 40 mole % of rare earth or yttrium oxide). In addition, the overall concentration of aluminum is much higher (10 – 40 mole % Al_2O_3) in the above mentioned glass systems compared to Al content in the EDSMAS glasses. Al(6) sites may not form until a certain level of rare earth and Al content is reached. Small spectral features in the region of the spectrum usually assigned to octahedral Al species do increase with Eu content. However, these features are not much above the noise level as seen in Fig. 24.

Quantitative analysis [19] of ^{27}Al by NMR showed that as the mole % of Eu_2O_3 in the glass increases, the percentage of the ^{27}Al calculated from the glass composition that can be detected by NMR decreases, going down to about 30% at 8.11 mole % of Eu_2O_3. Listed in Table 5 are the relaxation time constants for ^{27}Al with magic-angle spinning for

$\omega = 55, \delta\omega_{1/2} = 55$ Eu 8.11

$\omega = 54, \delta\omega_{1/2} = 42$ Eu 5.26

$\omega = 54, \delta\omega_{1/2} = 34$ Eu 3.90

$\omega = 56, \delta\omega_{1/2} = 25$ Eu 1.26

$\omega = 55, \delta\omega_{1/2} = 23$ Eu 0.73

$\omega = 55, \delta\omega_{1/2} = 19$ Eu 0

120   100   80   60   40   20   0   -20

Frequency, ppm from $Al(NO_3)_3$ (aq.)
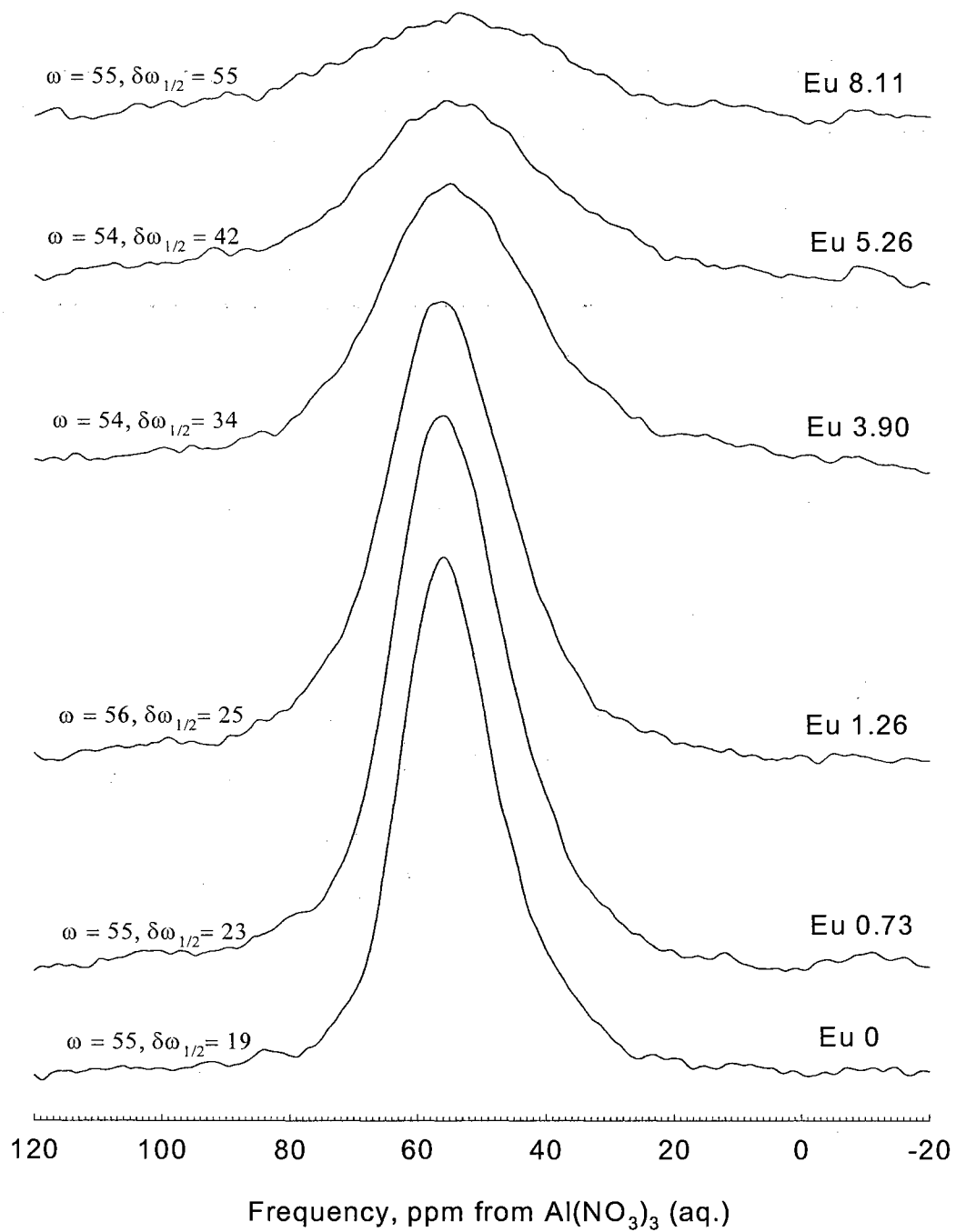
Fig. 24. ^{27}Al MAS NMR of EDSMAS glasses of Eu -series

79

Sample ID	T_1 (ms)	T_2 (ms)
Eu0	25 ± 3	4.6 ± 0.1
Eu1.26	31 ± 3	4.7 ± 0.1
Eu3.90	26 ± 3	4.2 ± 0.1
Eu8.11	23 ± 2	3.9 ± 0.2

Table 5. ^{27}Al MAS NMR Relaxation Times using fitting equations y = A₁(1 − A₂exp(-τ/T₁)) for T₁ and y = A₁exp(-2τ'/T₂) for T₂, where τ' = τ + (1/2)($t_{\pi/2}$) + (1/2)(t_{π}) where T_1 and T_2 are the spin-lattice and spin-spin relaxation constants, respectively.

four of the glass samples. Both T_1 and T_2 change very little with europium content. The T_2 values suggest homogeneous line widths of 0.9 to 1.0 ppm, for the Eu0 sample and those containing Eu_2O_3. Since ^{27}Al MAS line widths (about 19-55 ppm) are much larger than this, the line widths of the glasses are probably the result of a dispersion of chemical shifts and/or second-order quadrupolar shifts due to a variety of local structures around the Al(4), as might be expected for a glass. Considering that T_2 decreases only a small amount with Eu content, the observed broadening of the Al(4) resonances in the MAS spectrum as Eu content increases must be mainly due to increased disorder of the structure in the vicinity of aluminum, rather than enhanced relaxation by the paramagnetic Eu^{3+} ion.

^{29}Si NMR spectra of Eu-series EDSMAS glasses along with fitted peak positions ω and FWHMs $\delta \omega_{1/2}$ are shown in Fig. 25. Figure 26(a) shows how the observed ^{29}Si signal

80

$\omega = -98$, $\delta\omega_{1/2} = 38$ Eu 8.11

$\omega = -96$, $\delta\omega_{1/2} = 32$ Eu 5.26

$\omega = -98$, $\delta\omega_{1/2} = 28$ Eu 3.90

$\omega = -95$, $\delta\omega_{1/2} = 24$ Eu 1.26

$\omega = -94$, $\delta\omega_{1/2} = 23$ Eu 0.73

$\omega = -100$, $\delta\omega_{1/2} = 20$ Eu 0

0   -20   -40   -60   -80   -100   -120   -140   -160   -180   -200

Frequency (ppm from TMS)
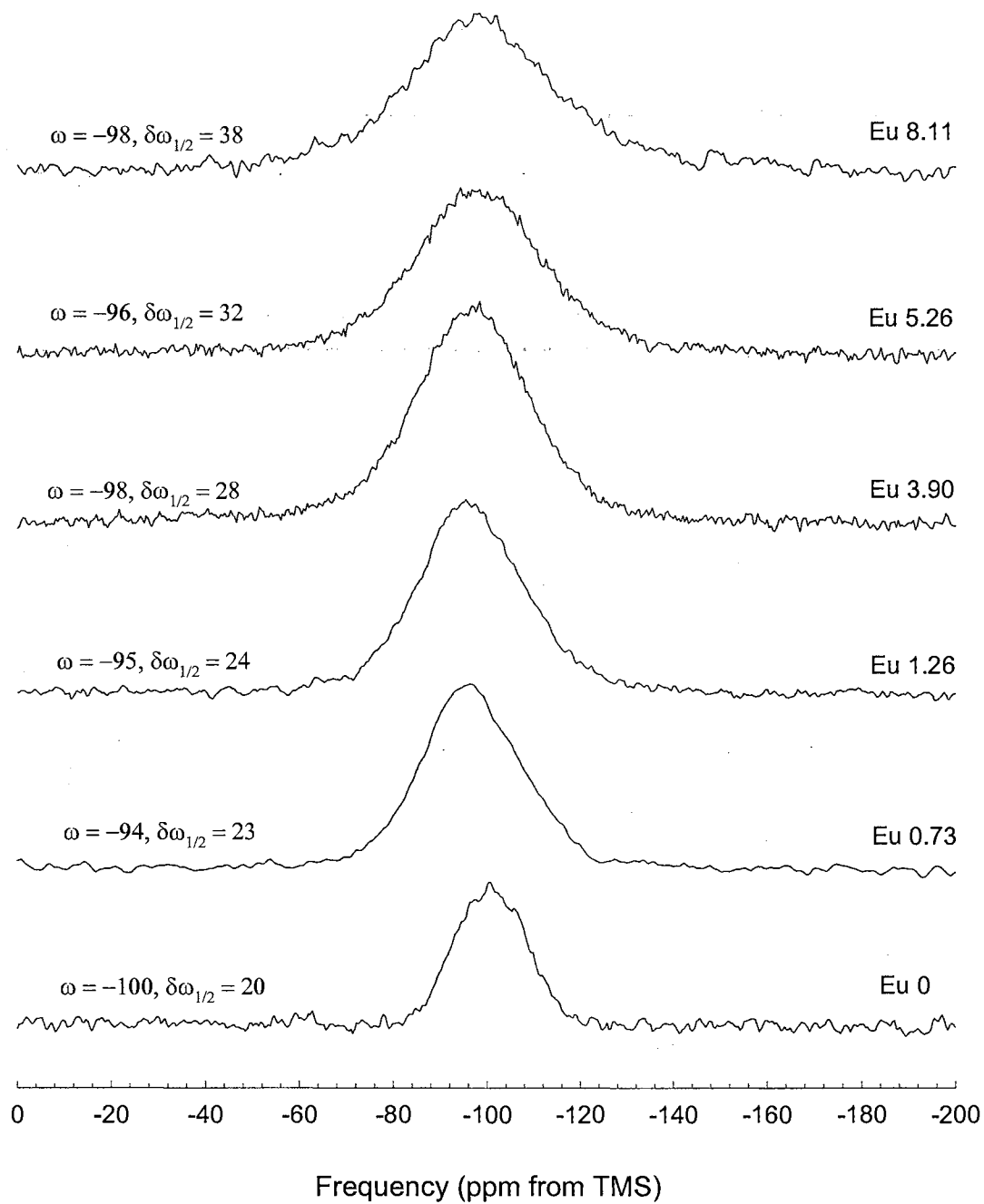
Fig. 25. ^{29}Si NMR of EDSMAS glasses of Eu-series

(a) Variable delay data for ^{29}Si

^{29}Si for Eu0 sample

^{29}Si for Eu8.11 sample

(b)T_2 data for ^{29}Si

- Eu8.11: $T_2 = 10 +/- 1$ ms
- Eu0: $T_2 = 52 +/- 3$ ms
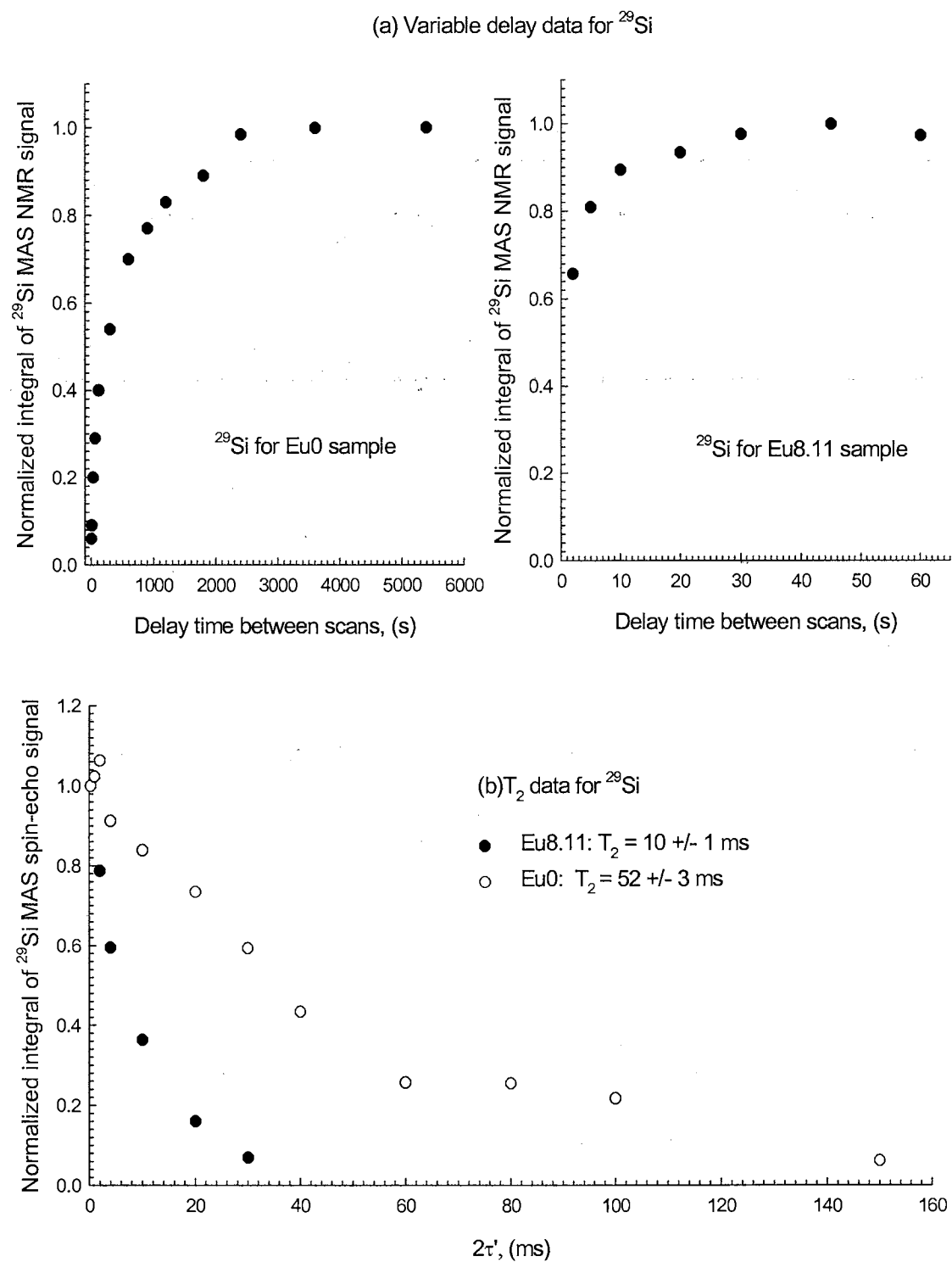
Fig. 26. Normalized integral of ^{29}Si MAS (a) NMR signal and

(b) spin-echo signal for Eu0 and Eu8.11 samples

varies with pulse delay for two of the glass samples. For the Eu0 sample, a delay of over 3000 s is necessary to allow for complete relaxation, while for the Eu8.11 sample a delay of 45 s is adequate, suggesting that T_1 decreases substantially as Eu enters the glass. Spectra were taken at 59.8 MHz with a spinning rate of 8.000 ± 0.005 kHz, and a $\pi/2$ pulse width of 9.0 μs. The number of scans averaged was 8 for 0 mole % Eu_2O_3 and 1800 for 8.11 Eu_2O_3 mole %. Figure 26(b) demonstrates spin-echo data of ^{29}Si MAS spectra and provides T_2 measurements for Eu0 sample (3600s pulse delay, 8 scans averaged) and for Eu8.11 sample (45s pulse delay, 500 scans averaged). The parameter τ' is defined in the legend of Table 5, along with the equation used in fitting. We can clearly see that $T_2(Eu8.11) < T_2(Eu0)$. The ^{29}Si MAS spectra for these two samples in Fig. 27 show a single broad peak at -(98-100) ppm, which is broader in the sample with europium. The ratio of the integrals of the two spectra, after division by the number of scans and number of moles of ^{29}Si, is 6 ± 2 %. Although we have not presented quantitative ^{29}Si NMR data for the complete set of glasses, because of the long time required to obtain such data due to the long T_1 relaxation times, loss of ^{29}Si signal with increasing europium concentration is evident. In the spectra of Fig. 27 the Eu8.11 sample shows a signal-to-noise ratio comparable to that of the Eu0 sample with a much larger number of scans averaged, indicating overall poorer signal-to-noise. Weighing of the samples permitted the integrals of the two spectra to be divided by number of moles of ^{29}Si and number of scans averaged. Assuming that all ^{29}Si is observable in the Eu0 sample, the ratio of these integrals shows that 6 % of the ^{29}Si is observable in the Eu8.11 sample, suggesting that the signal loss for ^{29}Si is greater than for ^{27}Al.

Eu0 sample:
position = -100 ppm
FWHM = 20 ppm

Eu8.11 sample:
position = -98 ppm
FWHM = 35 ppm

0   -20   -40   -60   -80   -100   -120   -140   -160   -180   -200

Frequency (ppm from TMS)
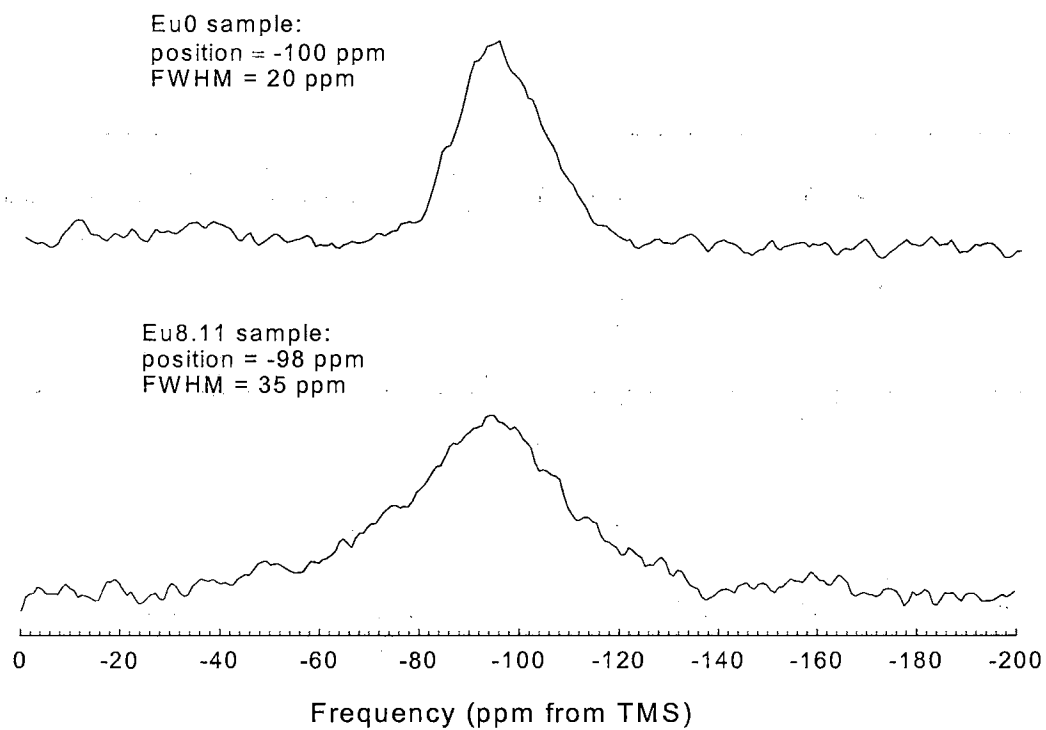
Fig. 27. ^{29}Si NMR spectra of Eu0 and Eu8.11 samples

As for ^{27}Al, the width of the ^{29}Si MAS peak cannot be accounted for by T_2 relaxation alone, since the T_2 values imply 0.1 ppm and 0.5 ppm homogeneous widths for 0 mol % and 8.11 mol % Eu_2O_3, respectively, while the actual widths are 20 ppm and 39 ppm. Since, in contrast to the case for ^{27}Al, T_2 decreases substantially with an increase of the mol % of Eu_2O_3, the broadening of the ^{29}Si peak with increasing Eu concentration may be due at least in part to enhanced relaxation by the paramagnetic Eu^{3+} ion. An increase in structural disorder, such as a greater variety of bond lengths and bond angles, could also contribute to the line broadening. The situation is more complicated than for ^{27}Al, because the ^{29}Si MAS peak comprises a group of unresolved peaks representing Q^n units with a series of values of n, each of which has a dispersion of chemical shifts due to structural disorder. Hence, both the width and position of this composite peak could change with the relative amounts of the different Q^n species. Because the ^{29}Si line broadening could originate from a few different sources, it is difficult to make a definite conclusion regarding its relationship to structure. Established ^{29}Si NMR resonance assignments for a variety of silicate and aluminosilicate glasses with alkali and alkaline earth modifiers are -76 to -88 ppm for Q^2, -85 to -97 ppm for Q^3, and -100 to -116 ppm for Q^4 [32, 118-122]. $Q^n(1Al)$ species are probably present in our glasses in small amounts because the Al_2O_3 concentration is low; the resonances for these species are at less negative frequency in comparison to those for the corresponding $Q^n(0Al)$ species. Q^3 species are the most prominent in both of the EDSMAS glass samples examined which is general agreement with growth of Q^3-Eu species deduced from Raman spectra. The development of more depolymerized SiO_4 tetrahedra, i.e. Q^n species with $n \leq 2$ is not well supported by the ^{29}Si NMR spectra. However, the NMR results only monitor the

observable subset of nuclei that are not too close to Eu^{3+}. It is probable that no shift in the position of the ^{29}Si peak is observed with europium content because there is a preferential disappearance of Q^n species with low n, which with their higher charge would have a greater propensity to coordinate with Eu^{3+}.

The ^{23}Na MAS NMR peaks for Eu-series EDSMAS glasses are shown in Fig.28 to be increasing in the linewidth which can be due to the rare earth ion effect of paramagnetic broadening. For Eu-free sample ^{23}Na peak is at -27 ppm. However upon initial introduction of rare earth ions, the position of the peak rapidly increases to -21 ppm. However, with further increase of Eu concentration, there is gradual shielding of ^{23}Na nuclei with the chemical shift moving to more negative values from -21 back to -27 ppm. This anomalous behavior is probably due to the complex combination of both: paramagnetic broadening and depolymerization. At highest Eu concentration we observe small sharp peak at ~ 6 ppm, which is probably due to the presence of sodium defect influenced by the rare earth ions clustering [6, 123]

5.1.5. The relation to holographic grating strength

The increase of Eu_2O_3 concentration from 0 to 8.11 mole % in soda magnesia aluminosilicate glasses improved both the transient and permanent gratings (Fig. 2) although reducing the ionic conductivity [6]. It is clear then, that the active role of the Eu^{3+} ions to drive the diffusion of small modifiers is more important in light induced grating formation than is the passive role of Eu in altering the structure of the network for this range of concentration. The saturation behavior of the grating strength at high Eu concentrations can be partly due to the decrease of Na ionic conductivity due to passive

$\omega = -27$ Eu 8.11

$\omega = -27$ Eu 5.26

$\omega = -24$ Eu 3.90

$\omega = -23$ Eu 1.26

$\omega = -21$ Eu 0.73

$\omega = -27$ Eu 0

-100   -80   -60   -40   -20   0   20   40

Frequency, ppm from NaCl (aq.)
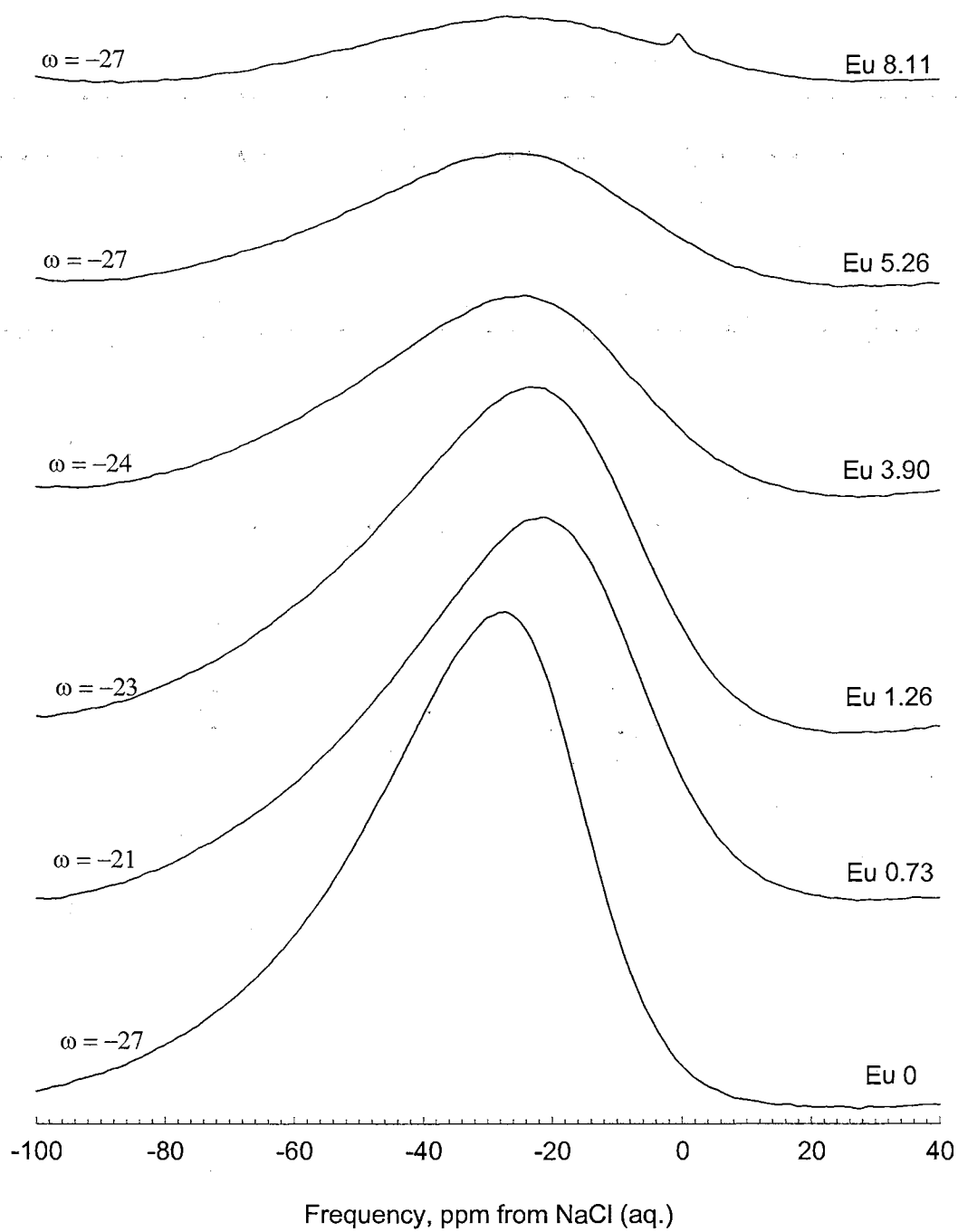
Fig. 28. ^{23}Na MAS NMR spectra of EDSMAS glasses of Eu-series

role of Eu ions deduced from the measurements of the activation energy of Na ions with the increase of rare-earth content [6]. Rare-earth ions alter the network either by clustering or by beginning to block the diffusion channels in the network. Clustering of rare-earths at this concentration is possible [6, 123]. The development of highly depolymerized species, i.e. Q^n with $n \leq 2$ deduced from Raman spectra supports this contention. This causes an inhomogeneous distribution of Eu in the glass network, which in turn, leads to a decrease in the ability of Eu to effectively influence the migration of light modifiers.

The increase of the EDSMAS glass hardness (elastic constants) measured by the BLS spectroscopy implies that the stability of the traps [73] for the hopping light ions (Na^+ and Mg^{2+}) can increase because europium modifiers tend to stretch the glass network [9]. This increased stability of the traps also contributes to the increased photorefractive grating efficiency [73].

As was mentioned in Chapter I, through the process of FWM experiment Eu^{3+} ions of EDSMAS glass are excited by the laser write beam to the off-resonance $^5D_2$ – energy level. Radiationless relaxation from this excited state to the $^5D_0$ metastable level results from the emission of several high-energy phonons on the order of 1000 cm^{-1} [2]. This affects the structure of the glass modulating the index of refraction. In this sense, the role of high energy phonons (~ 1000 cm^{-1}) is believed to be crucial, since they fill the energy gap between the excited level and metastable $^5D_1$ as well as $^5D_0$ levels and provide the activation energy for some light modifiers (Na and Mg atoms) to migrate from the bright to dark region of the grating during FWM experiment, so that the permanent grating is formed. These high energy phonons are provided through optical phonons in the form of

Si-NBO stretching vibrations in various Q^n species (n<4), with Q^3-Eu tetrahedral units becoming the predominant species.

5.2. Al-SERIES

5.2.1. Elastic parameters.

The results of BLS measurements for Al-series are shown in Table 6. Measured Brillouin shifts (ω_L, ω_T), refractive indices n, density ρ and absorption coefficients are used to calculate elastic constants (C_{11}, C_{44}) using (2.1.10), Young's modulus E, bulk modulus B and Poisson's ratio σ using (2.1.12). As shown in Fig. 29(a) the trend of such elastic parameters as C_{11}, C_{44}, E, B clearly show that the glasses become less compressible with the increase of alumina concentration. However, the increase of Poisson ratio σ in Fig. 29(b) indicates that the structure bonding becomes more polarizable. These trends in elastic parameters are in agreement with those in calcium aluminosilicate glasses [14] with the increase of Al_2O_3 concentration.

When Al atoms are introduced into glasses, they substitute Si atoms in the tetrahedral network causing the formation of more bridging oxygens (BO) (see Table 1(b)) while capturing the free space in the glass because aluminum atoms have larger atomic radii ($R_{Al} \approx 0.39$ Å) than silicon atoms ($R_{Si} \approx 0.26$ Å) do [100]. The NBO ions are used to form the Al-O-Si bridging oxygen, where the Al^{3+} ions are tetrahedrally coordinated. Therefore, as Al_2O_3/SiO_2 ratio increases, more free space is captured. The increase of the glass hardness can also be understood from the schematics shown in Fig. 30. Substitution of Si by Al is accompanied by forming stronger Si-BO bonds (Si-O-Al-O-Si bridges) via transferring the network modifiers (e.g. $M = Na^+$, Mg^{2+} and/or Eu^{3+}) from Si-NBO

Sample ID	ρ (g/cm^3)	ω_L (cm^{-1})	ω_T (cm^{-1})
Al 0	2.48 ± 0.02	0.789 ± 0.003	0.472 ± 0.002
Al 2.96	2.61 ± 0.02	0.800 ± 0.003	0.478 ± 0.003
Al 5.92	2.64 ± 0.03	0.808 ± 0.003	0.482 ± 0.003
Al 8.88	2.69 ± 0.03	0.824 ± 0.003	0.489 ± 0.003
Al 14.80	2.74 ± 0.04	0.843 ± 0.003	0.498 ± 0.003
Fused Silica	2.21	0.804	0.506

Sample ID	C_{11} (GPa)	C_{44} (GPa)	E (GPa)	B (GPa)	σ
Al 0	79.8 ± 0.7	28.6 ± 0.4	69.8 ± 0.7	41.7 ± 0.2	0.221 ± 0.002
Al 2.96	85.7 ± 0.7	30.6 ± 0.4	74.8 ± 0.8	44.9 ± 0.2	0.222 ± 0.002
Al 5.92	88.1 ± 0.8	31.4 ± 0.5	76.8 ± 0.8	46.2 ± 0.3	0.223 ± 0.002
Al 8.88	92.9 ± 0.9	32.7 ± 0.5	80.3 ± 0.9	49.3 ± 0.3	0.228 ± 0.003
Al 14.80	98.2 ± 1.0	34.3 ± 0.5	84.5 ± 1.0	52.5 ± 0.4	0.232 ± 0.003
Fused Silica	79.6	31.5	73.9	37.6	0.174

Table 6. Calculated elastic constants C_{11}, C_{44}, Young modulus E, bulk modulus B and Poisson ratio σ of Al-series based on the measured values of density ρ and Brillouin shifts ω_L, ω_T.
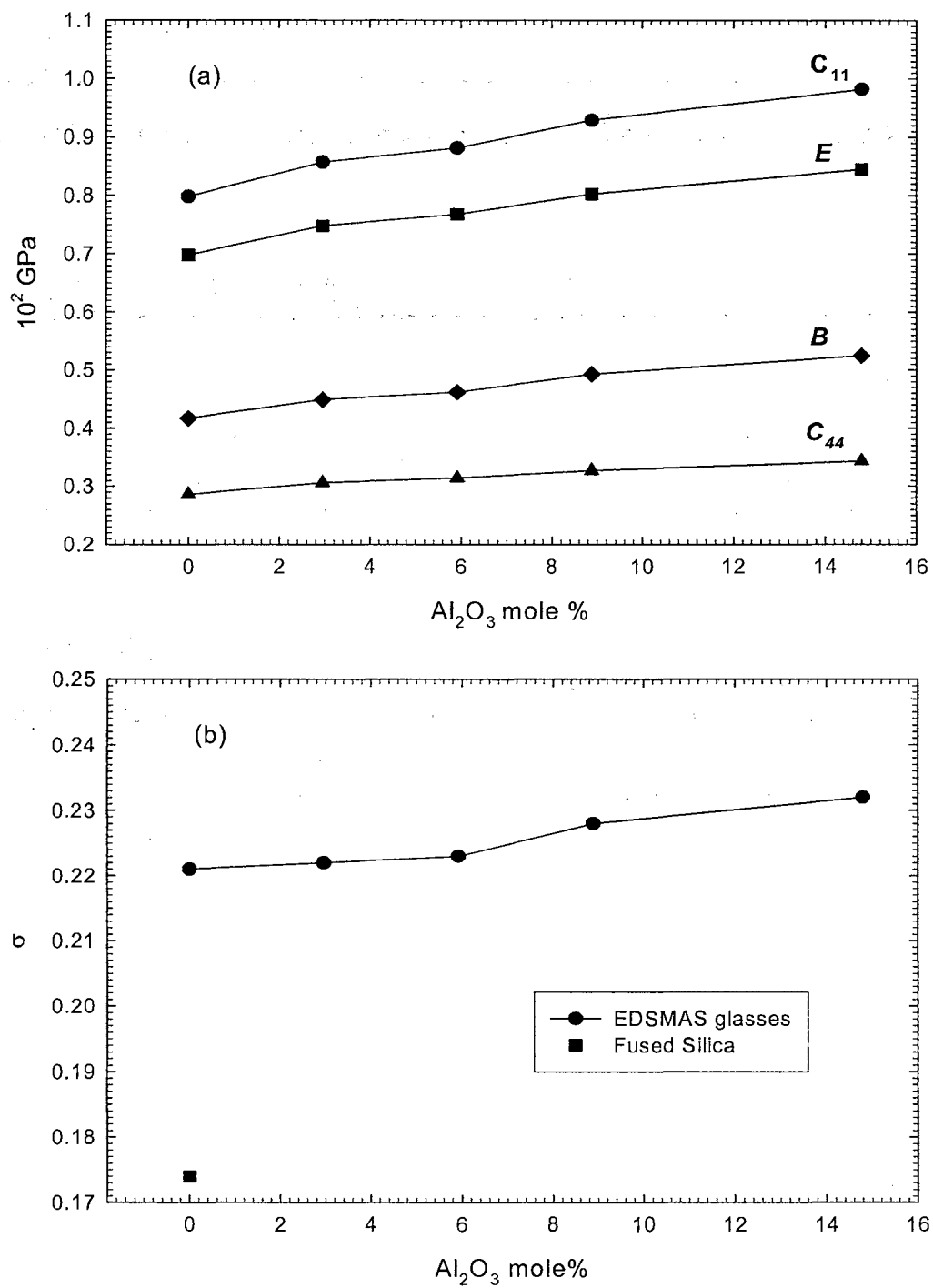
Fig. 29. (a) Compressional C_{11}, shear C_{44}, Young E and bulk B moduli

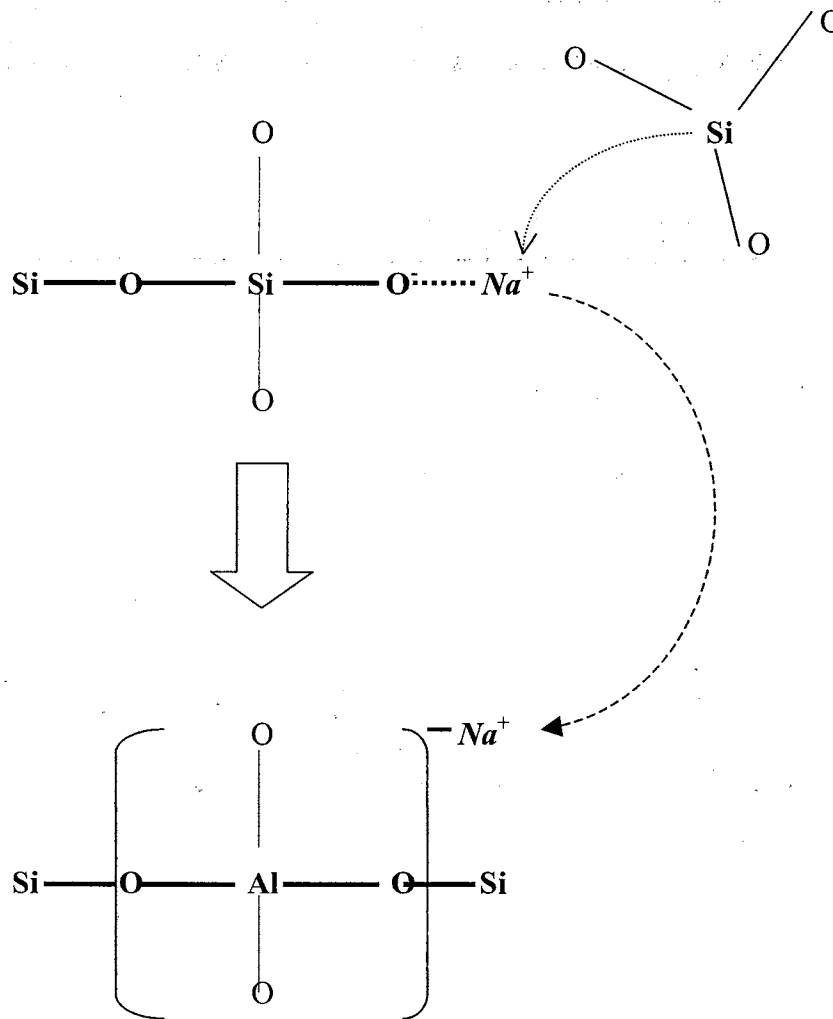(b) Poisson ratio σ versus Al_2O_3 mole %

Fig. 30. Si substitution by Al causes the formation of more strong Si-O-Al-O-Si bridges

while recovering Si-O-Si bridging oxygens by means of charge redistribution of Na^+ ion

from Si-O⁻Na link to compensate the charge of $[AlO_4]^-$ complex.

weaker bridges to the vicinity of $[AlO_4]^-$ groups. In this way the recovering of Si-O-Si bond, i.e. BO at the site of the removed modifier occurs. Besides, the molar mass M of the glass increases with alumina/silica ratio which is also in agreement with the mass increase upon enhancement of alumina concentration in yttrium aluminosilicate glass [96]. Consequently, the elastic constants C_{11} and C_{44} increase, as do the Young's and adiabatic bulk moduli. Sodium ions will be the most favorable candidates for charge compensation due to their monovalency and abundance in EDSMAS glass.

Mysen *et al* [124] observed that in $NaAlO_2$-SiO_2 system the effect of pressure on T-O-T angle becomes more pronounced with increasing Al/(Al+Si). This increase is associated with a greater effect of pressure on the viscosity with increasing Al/(Al+Si) [125]. In contrast, in the system $CaAl_2O_4$-SiO_2, the inter-tetrahedral angle becomes less sensitive to pressure with increasing Al/(Al+Si) of the melt. This diminished effect [124] is associated with decreasing effect of pressure on the viscosity of aluminosilicate melts on the join $CaAl_2O_4$-SiO_2 [125]. The response of the inter-tetrahedral angle to pressure can also be correlated with the compressibility of aluminosilicate glasses. In the $NaAlO_2$-SiO_2 system the melts become increasingly compressible with increasing Al(Al+Si), whereas in the case of $CaAl_2O_4$-SiO_2 system the compressibility decreases with increasing pressure. It is possible that EDSMAS glass system demonstrates increasing compressibility due to the enhancement of Al_2O_3/SiO_2 ratio because of important role played by high valence ions present in the glass such as Mg^{2+} and Eu^{3+} ions. The large field strength of the Mg^{2+} and Eu^{3+} ions allows them to act more like intermediate ions and to have a larger effect on the strength of the bonds connecting the vitreous network. Furthermore the divalent

magnesium and trivalent europium ions act as a link between neighboring NBO ions, whereas the monovalent sodium ions tend to act simply to balance the charge on a single neighboring oxygen ion. In other words, magnesium and europium ions do not simply balance the charge on neighboring NBOs, but also act as structural links to maintain the connectivity of the network (of course the links are significantly weaker than the Si-O-Si linkages).

The larger values of the Poisson ratio σ for the EDSMASS glasses, compared with those of fused silica as shown in Fig. 29(b), imply that the overall bonding in the EDSMAS glass is more polarizable (softer lattice) [66, 103, 104] than in fused silica because of the presence of NBOs and the average glass bonding becomes even more ionic with further increase of alumina-to-silica ratio. Besides, the activation energy of Na^+ ions obtained from the ionic conductivity measurements of the EDSMAS glass samples is observed to decrease with increasing alumina content [7]. This has been attributed to the fact that Na^+ ions charge compensating the $[AlO_4]^-$ complexes are bound more weakly that those sodium ions bound to NBOs [65]. Sodium ions are associated with aluminum tetrahedron should have a higher ionicity than those associated with NBO ions [126], i.e. the polarizability of $[AlO_4]^- Na^+$ bond is higher than that of $Si-O^- Na^+$ bridges (see Fig. 31 with two types of Na^+ ions). The Judd-Ofelt intensity parameters Ω_2 and Ω_6 obtained from absorption measurements on EDSMAS glasses [24], are also observed to increase with Al_2O_3/SiO_2 ratio. Ω_2 increases by increasing the polarity or the asymmetry of Eu^{3+} sites. The formation of Al-O-Si bond lowered the covalency of Eu-O bond and thus increased Ω_6 value [105]. Based on the [151]Eu Mossbauer spectra [127], it

has been shown that the covalence of the Eu-O bond decreases with increasing Al_2O_3 content. Thus, from
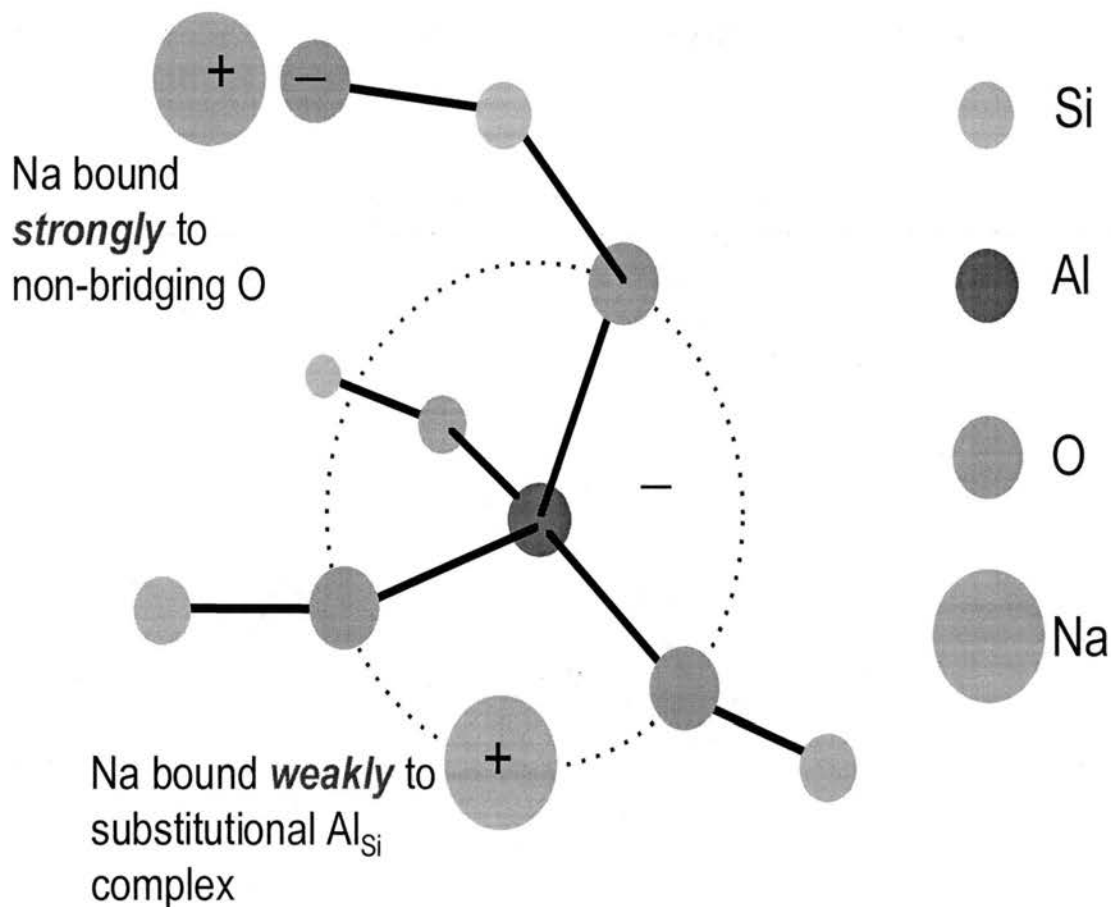
Fig. 31. Two types of Na^+ ions present in EDSMAS glass

the trends of Ω_2 and Ω_6 values, we can see that the bond polarizability of Eu-O increases and the Eu-O bond becomes more ionic as the concentration of Al atoms increases. The ionic polarizability of soda aluminosilicate glass increases with the Al/Si ratio deduced by high resolution x-ray photoelectron spectroscopy [128]. Thus, all these facts are

95

supportive of the increasing polarizability in the overall bonding structure of the EDSMAS glass.

5.2.2. Photoelastic constants

Based on calculated molar mass M of the EDSMAS glasses of Al-series and measured values of P_{12}, P_{44}, n, ρ we calculated LLE, LE, AE, α and G using (2.1.20), (2.1.21), (2.1.23) and (2.1.24). The results of these calculations along with the measured values of photoelastic constants P_{12} and P_{44} are listed in Table 7 and plotted in Figs. 32-34 versus Al_2O_3 mole %. The values of the measured absorption coefficient α_a used for calculating P_{12} and P_{44} are listed in Table 7 as well. We observe that up to 5.92 mole % of Al_2O_3, LLE and P_{12} (P_{44}) decrease (increase) mostly because of the increase (decrease) in polarizability α. The opposite trend takes place at higher alumina concentrations, i.e. LLE and P_{12} (P_{44}) increase (decrease) mostly because of the decrease (increase) in polarizability α. Since all other parameters such as n, M, ρ change monotonously throughout the whole Al-series, they do not characterize the extreme behavior of P_{12} and LLE. Although there is an extremum behavior in polarizability α, the average polarizability obtained by the linear fit of the experimental points in Fig. 33(a) can be approximated as increasing, which is in agreement with Poisson's ratio data, Judd-Ofelt intensity parameters obtained from the absorption measurements [24], and the enhancement of sodium ionicity and dielectric constant in soda aluminosilicate glass with the increase of Al/Si ratio [126].

The same approximation applied to correlation integral G values yields the diminishing of G values shown in Fig. 33(b). In order to understand the significance of

the decrease in the average G obtained by the linear fit of the experimental points in terms of structural changes of the EDSMAS glass, we note the presence of r^{-4} in the integrand of the integral indicating that the G values are very sensitive to the effective

Sample ID	α_a (cm^{-1})	P_{12}	P_{44}	M (g/mole)	n
Al 0	0.53±0.01	0.256±0.010	-(0.058±0.005)	61.701	1.518 ± 0.005
Al 2.96	0.76±0.01	0.251±0.009	-(0.056±0.004)	62.938	1.524 ± 0.005
Al 5.92	0.45±0.01	0.238±0.008	-(0.055±0.004)	64.181	1.527 ± 0.005
Al 8.88	0.21±0.01	0.253±0.008	-(0.060±0.005)	65.420	1.530 ± 0.005
Al 14.80	0.23±0.01	0.253±0.008	-(0.062±0.005)	67.899	1.537 ± 0.005
Fused Silica	0.04	0.279	-0.078	60.086	1.462

Sample ID	α (10^{-23}cm^3)	G (10^{23} cm^3)	LLE	LE	AE
Al 0	0.154±0.008	4.11±0.21	0.624±0.008	-(0.064±0.001)	-(0.122±0.001)
Al 2.96	0.168±0.008	3.69±0.18	0.615±0.007	-(0.065±0.001)	-(0.119±0.001)
Al 5.92	0.174±0.009	3.52±0.18	0.602±0.006	-(0.065±0.001)	-(0.125±0.001)
Al 8.88	0.167±0.009	3.83±0.19	0.631±0.006	-(0.066±0.001)	-(0.127±0.001)
Al 14.8	0.170±0.009	3.79±0.19	0.641±0.006	-(0.067±0.001)	-(0.128±0.001)
Fused Silica	0.150	5.27	0.678	-0.057	-0.134

Table 7. Calculated values of LLE, LE, AE, α and G of Al-series based of the measured values of absorption coefficient α_a, photoelastic constants P_{12} and P_{44}, index of refraction n, density ρ, calculated molar mass M.
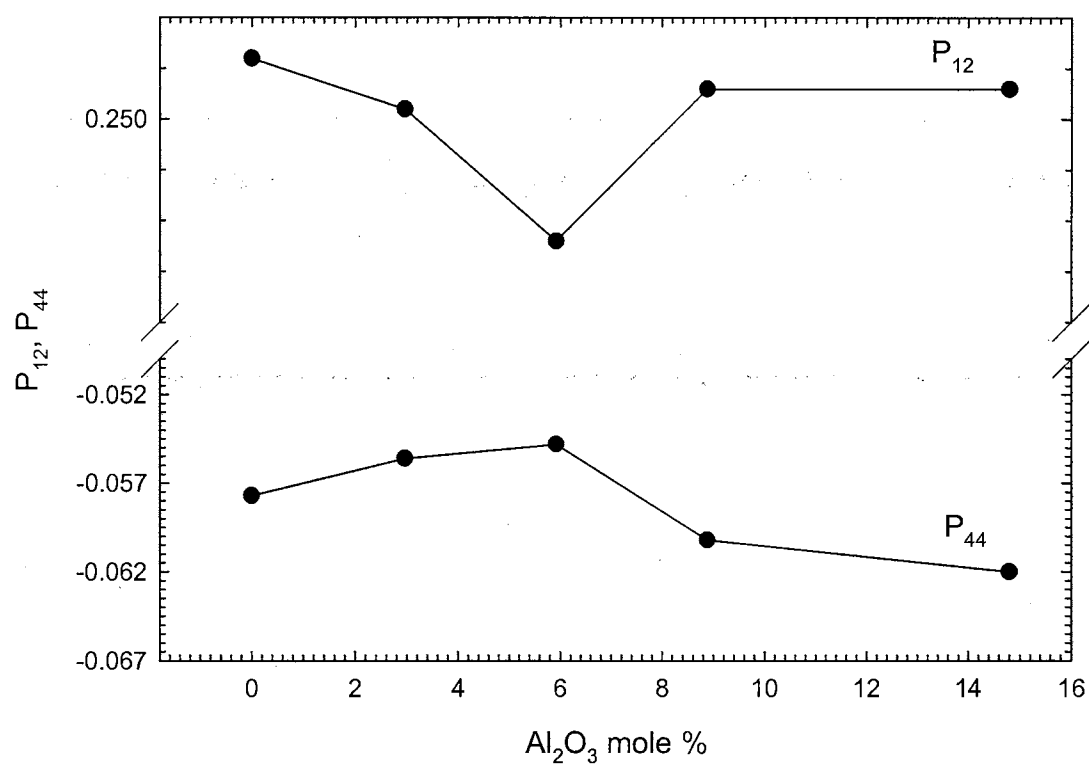
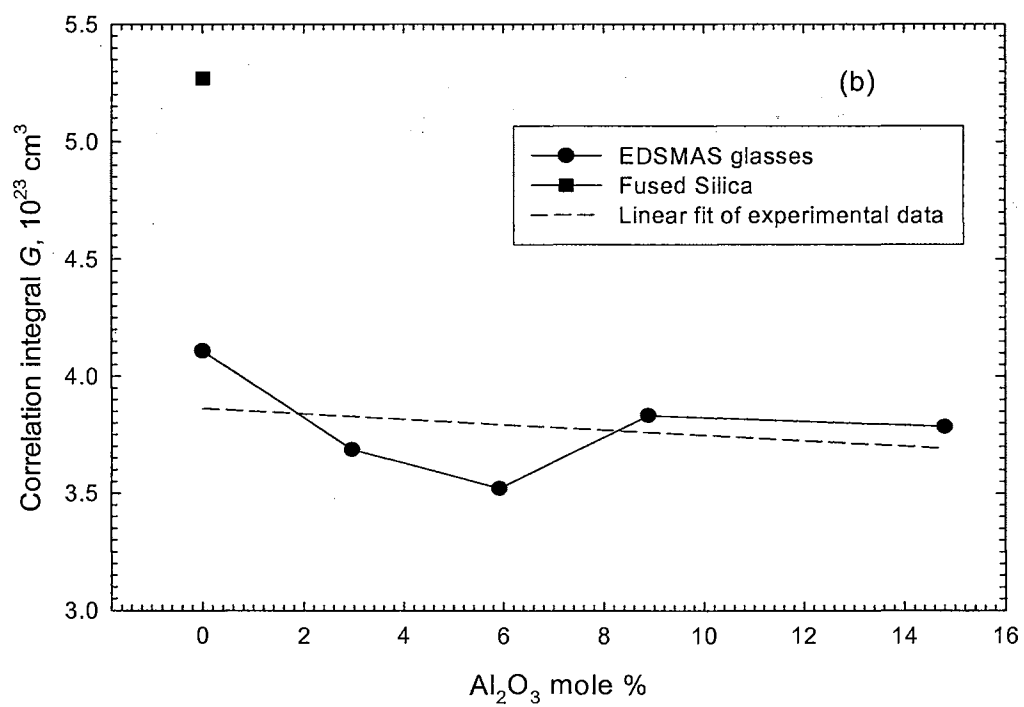Fig. 32. Photoelastic constants P_{12} and P_{44} versus Al_2O_3 mole%
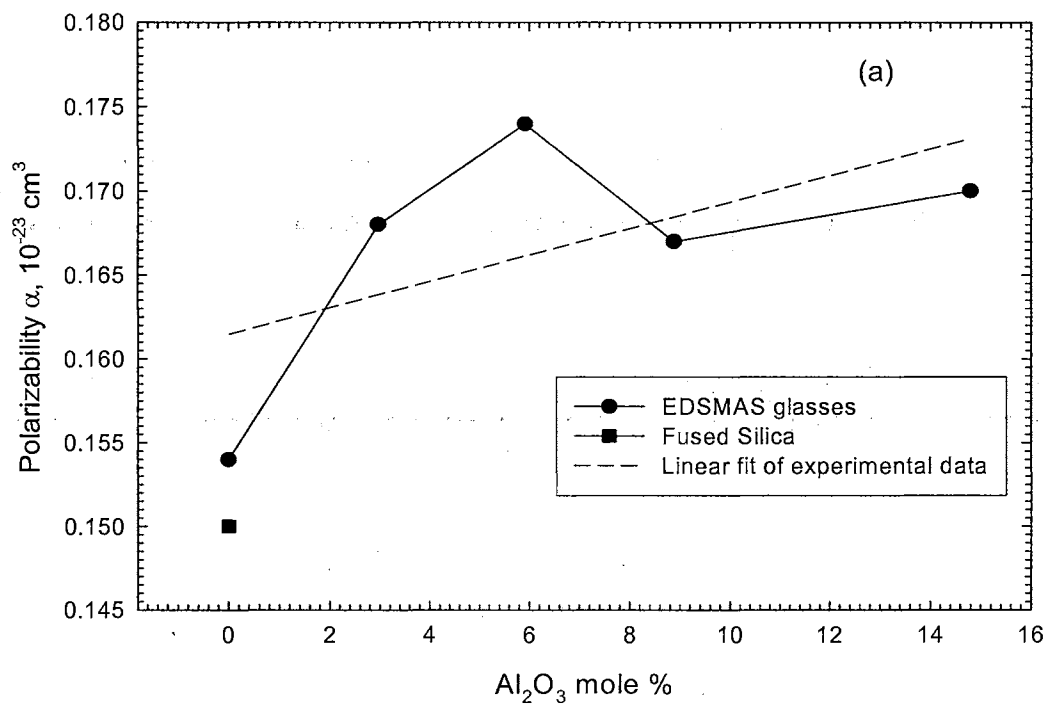
Fig. 33. (a) Polarizability α and (b) correlation integral G vs Al_2O_3 mole %
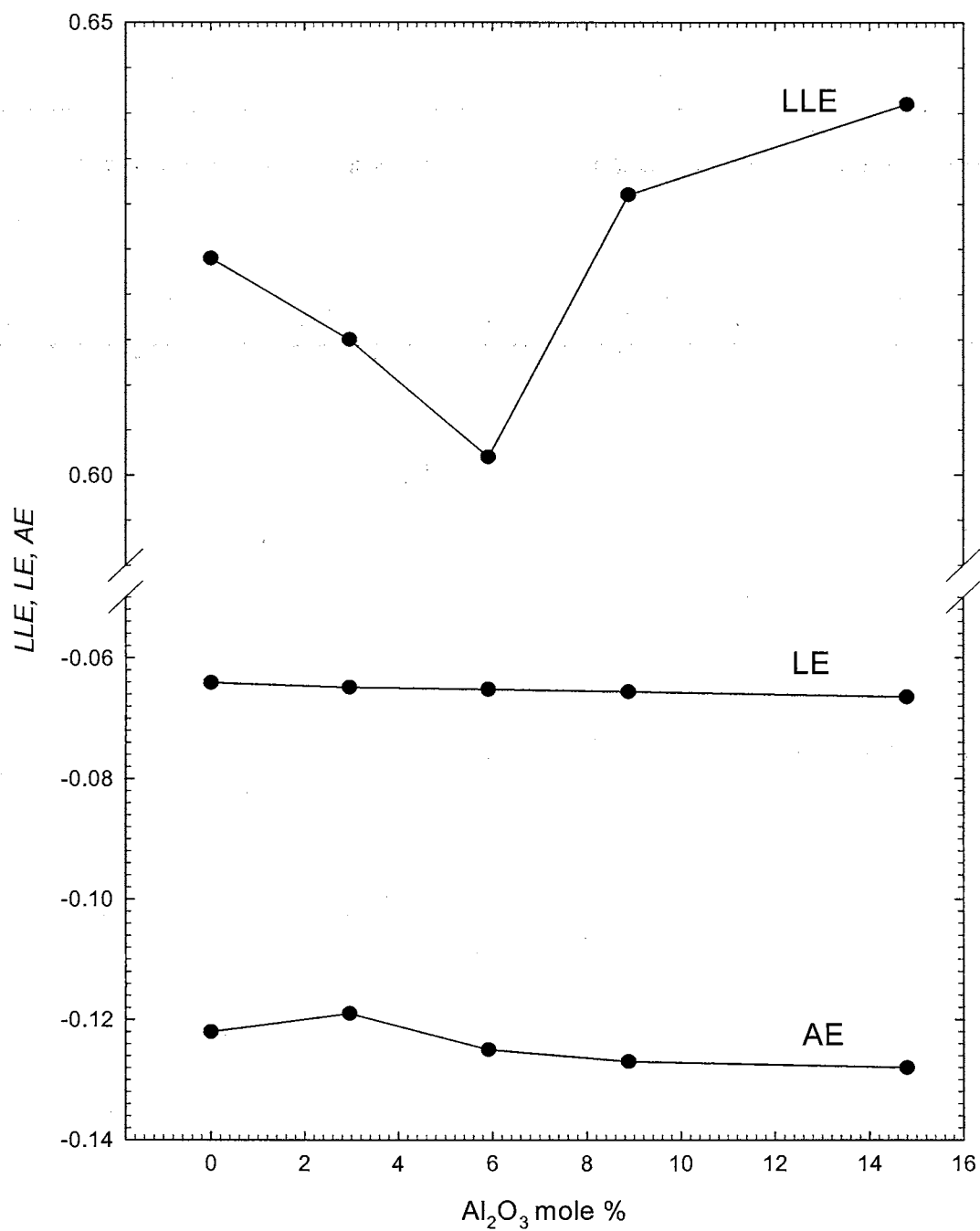
Fig. 34. Lorentz-Lorentz effect (*LLE*), lattice effect (*LE*) and atomic effect (*AE*) versus Al_2O_3 mole %.

change in the bond lengths. It has been shown that in aluminosilicate glasses T-O (T = Si, Al) bond length ranges from r_{Si-O} = 1.62 Å for pure SiO_4 to r_{Al-O} = 1.72 Å for pure AlO_4 tetrahedra [108]. Therefore, it is this difference in bond lengths of Al-O and Si-O which we think is responsible for the decrease of the correlation integral G. From Fig. 34 we see that $|LE| < |AE| < LLE$, i.e. the largest contribution to P_{12} values comes from the first term, i.e. Lorentz-Lorentz effect (LLE). Besides, lattice effect (LE) is smaller than the atomic effect (AE) because it is easier to distort atomic sites than the group of atoms (lattice).

5.2.3. RLS Spectroscopy

Unpolarized Raman spectra for the EDSMAS glasses with various Al_2O_3 concentrations are presented in Fig. 35. High energy Raman spectrum of Al-free glass (Al0 sample) has two partially resolved bands at 1100 cm^{-1} and 960 cm^{-1}, attributed to Si-NBO stretching vibrations in SiO_4 tetrahedra with one and two NBOs, respectively [129]. The 1100 cm^{-1} band is dominant indicating preponderance of Q^3 species in this glass sample. With the increase of Al_2O_3/SiO_2 ratio, the whole (850-1240) cm^{-1} Raman envelope undergoes systematic spectral broadening with the eventual merging of the 1100 cm^{-1} and 960 cm^{-1} Raman bands. These effects occur because of the appearance and successive height enhancement of the hidden bands corresponding to Si-BO stretches in Si-O-Al bridges of $Q^n(mAl)$ structural units (m = 1,2,3 and possibly 4) and concurrent height suppression of the bands corresponding to Si-NBO stretches in silicate Q^n bands, where n is the number of BOs per SiO_4 and m is the number of AlO_4 tetrahedra placed next to SiO_4 tetrahedron [129, 130]. Fig. 36 schematically demonstrates the characteristic
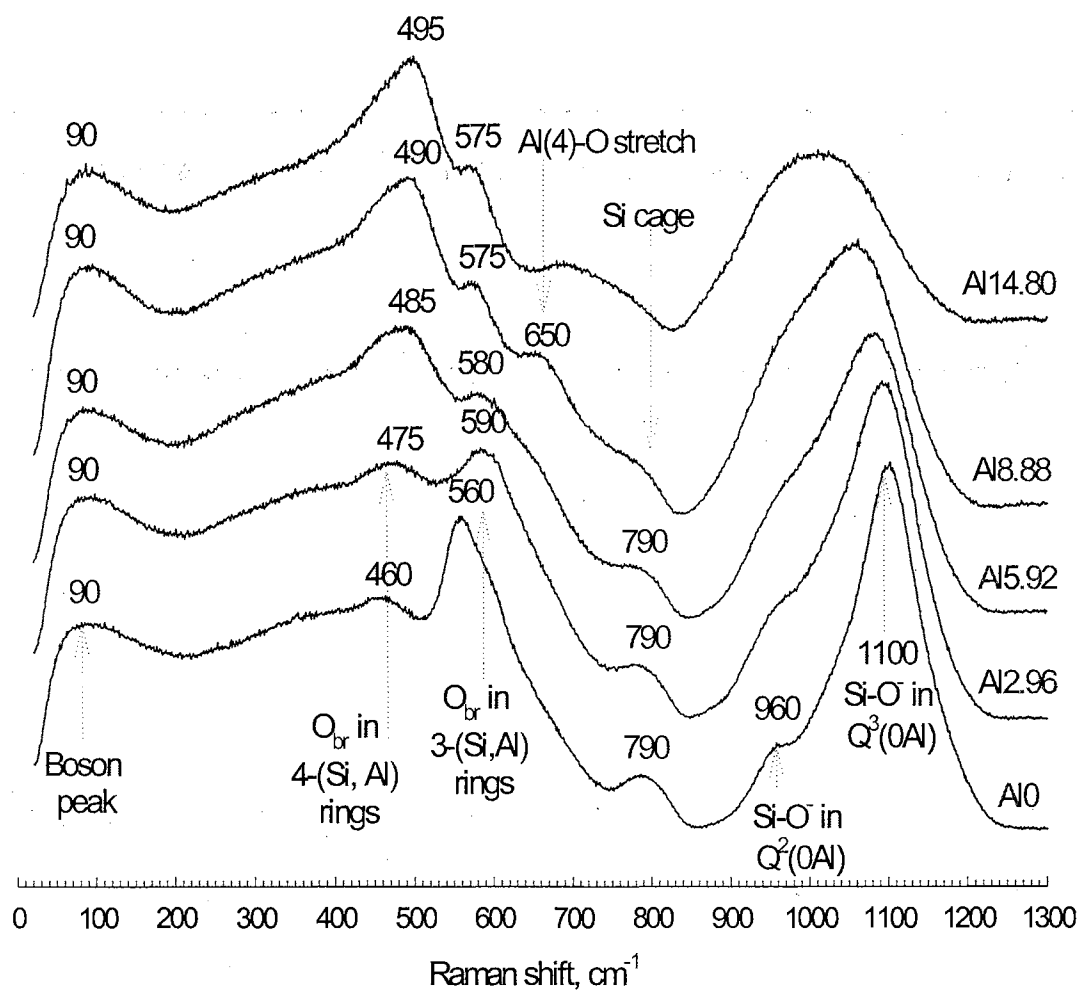
Fig. 35. Raman spectra of EDSMASS glasses of Al-series

SiO\
SiO— Si ⇒OAl
SiO/

$1140\ cm^{-1}$, $Q^4(1Al)$

SiO\   /OAl
      Si
SiO/   \OAl

$1000\ cm^{-1}$, $Q^4(2Al)$

      /OAl
SiO— Si →OAl
      \OAl

$925\ cm^{-1}$, $Q^4(3Al)$

        /OAl
AlO←Si→OAl
AlO/

$890\ cm^{-1}$, $Q^4(4Al)$
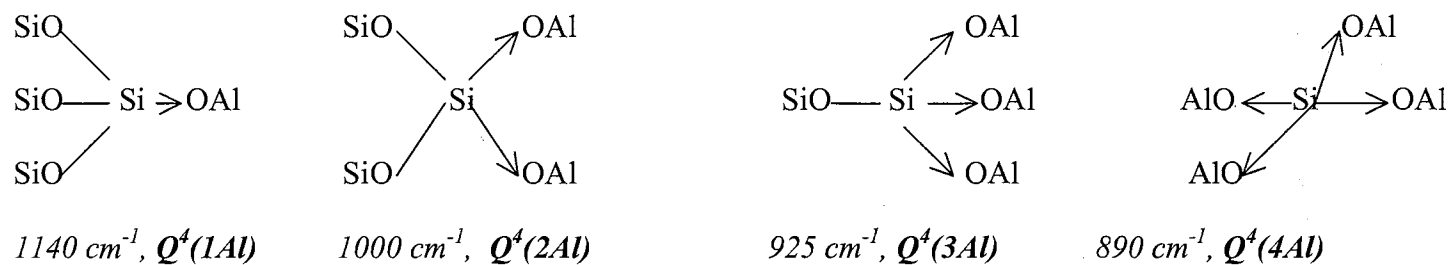
a) $Q^4(mAl)$ units (m =1-4) of aluminosilicate glasses

SiO
SiO←Si—O⁻
SiO/

1060-$1100\ cm^{-1}$, $Q^3(0Al)$

O⁻
SiO←Si→OSi
O⁻

$890\ cm^{-1}$, $Q^2(0Al)$

O⁻
SiO←Si—O⁻
O⁻

$900\ cm^{-1}$, $Q^1(0Al)$

O⁻
O⁻—Si—O⁻
O⁻

$850\ cm^{-1}$, $Q^0(0Al)$
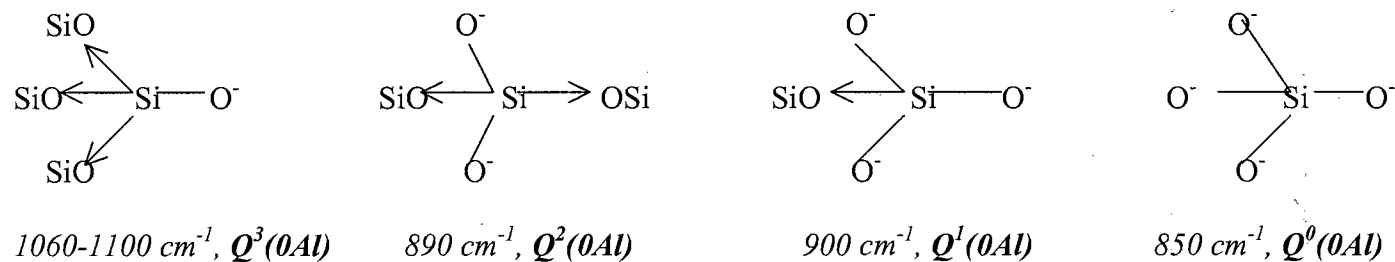
b) $Q^n(0Al)$ units (n =0-3) of silicate glasses

Fig.36. (a) Characteristic structural aluminosilicate $Q^4(mAl)$ units (m =1-4) [21] and (b) silicate $Q^n(0Al)$ units (n =0-3) [112].

structural units of aluminosilicate and silicate glasses. The concurrent (850-1240) cm^{-1} Raman envelope suppression with respect to the height of the band at 790 cm^{-1} takes place because Si-NBO links are decreased in their number and the polarizability of Si-BO bonds formed with the increase of alumina are much less than that of Si-NBO bonds, i.e. Si-O stretching vibrations in Si-O-Al and Si-O-Si bridges have small Raman activity. At 14.88 mole % of Al_2O_3, the maximum of (850-1240) cm^{-1} Raman band is at ~ 1040 cm^{-1}, which implies, according to Fig. 36, that $Q^4(2Al)$ (~ 1000 cm^{-1}) and $Q^3(0Al)$ (~ 1060-1100 cm^{-1}) species are the predominant ones for this glass sample. These two bands are heavily overlapped, so it would be ambiguous to say which one among them are really dominant species. However, since the majority of oxygens in this glass sample are in the bridging form (see Fig. 1(b)), we would expect to have the predominance of $Q^4(2Al)$ species in this material.

The mid-frequency 790 cm^{-1} band is traditionally assigned to the motion of silicon on a tetrahedral cage of oxygen remaining the replica of vitreous silica [106]. With no presence of aluminum atoms (Al0 glass) the sharp peak at 560 cm^{-1} resembles a symmetric oxygen "ring-breathing" mode of three-member siloxane ring "defects" similar to 606 cm^{-1} D_2 line in fused silica [131]. Introducing aluminum atoms to the glass network (Al2.96 sample) causes the appearance of a new band at 590 cm^{-1}. It is reasonable to assign this peak to a combination of oxygen "breathing" (O_{br}) modes within three-member $(Si,Al)_3$ and siloxane rings in the glass [114, 131]. Further increasing of the Al_2O_3 / SiO_2 ratio leads to the slight frequency downshift from 590 cm^{-1} to 575 cm^{-1} which may be due to the weakening of Si-O and Al-O bonds in $(Si,Al)_3$

rings. The concurrent narrowing of this band occurs as well, indicating that the aluminosilicate 3-member ring structural network undergoes ordering.

The relative height of 460 cm^{-1} band significantly increases with respect to that of 590 cm^{-1} band, suggesting that enhancement of Al population especially affects the amount of 4-member $(Si,Al)_4$ rings [115] which increases relative to that of the three-member $(Si,Al)_3$ rings. This trend suggests that Al atoms form more polymerized network with broader T-O-T angle rather than fragmental aluminosilicate network, which is in agreement with the increase of C_{11}, C_{44}, E and B deduced from BLS studies. In addition, both peaks become narrower, suggesting that $(Si,Al)_4$ and $(Si,Al)_3$ ring structures become structurally distinct from each other and more ordered. The frequency of the 460 cm^{-1} band increases from 460 cm^{-1} to 495 cm^{-1} due to the O_{br} mode frequency enhancement in these rings. Possible strengthening of Al-O and Si-O bonds in four-member rings can be responsible for this, which is again in agreement with increasing hardness of the glass deduced from Brillouin scattering studies. It is necessary to note that opposite trends in the frequencies of the bands at 460 cm^{-1} and 590 cm^{-1} were observed for the EDSMAS glasses by varying Eu_2O_3 concentration [19]. Hence, it is likely that the effect of network formers (modifiers) on the EDSMAS glass is characterized by the frequency increase (decrease) of 460 cm^{-1} band and by the frequency decrease (increase) of 590 cm^{-1} band. This contention is also supported by the increase of vibrational frequency of 590 cm^{-1} band with the increase of Na concentration in EDSMAS glass (see Na-series section below). The Boson peak at ~ 90 cm^{-1} and other portions of low frequency Raman spectra remain unaffected. A new

Raman band at 650 cm^{-1} can be assigned to Al-O stretching vibration [132] with Al being in tetrahedral coordination.

5.2.4. Solid-State NMR

The coordination of aluminum is four-fold in alkali aluminosilicate glass [32, 34, 64] and alkaline-earth aluminosilicate glass [33]. The study of the local structure of Sm-doped aluminosilicate glass revealed more tetrahedral than octahedral aluminum sites [133]. It is important to note that as we increase Al_2O_3/SiO_2 ratio, the change in the linewidth of our ^{27}Al, ^{29}Si and ^{23}Na NMR spectra of Al-series EDSMAS glasses is not due to paramagnetic nature of Eu^{3+} ions present in our glasses since for all these glasses have a constant Eu_2O_3 concentration (see Table 1(b)).

In Fig.37 the ^{27}Al MAS-NMR results show a single peak at ~ 56 ppm providing clear evidence that the only coordination of aluminum in EDSMAS glasses of Al-series is four. With the increase of alumina content the height of the peak at ~ 56 ppm increases further with respect to background level showing further enhancement in the amount of tetrahedrally coordinated Al sites. The ^{27}Al peak position does not change because aluminum atoms are not shielded by the next nearest Al neighbors or remotely spaced Al neighbors.

^{29}Si NMR spectra in Fig. 38 show single, broad and symmetric bands typical for the variety of silicate and aluminosilicates disordered materials due to a wide distribution of local structural environments around Si sites, i.e. the presence of broad variety of $Q^n(mAl)$ units ($0<n<4$, $0<m<4$) also shown in Fig. 36. For fused silica SiO_2 it is known that ^{29}Si resonance is at -109 ppm corresponding to the

Al14.80

ω = 56 ppm;
$\delta\omega_{1/2}$ = 24 ppm

Al8.88

ω = 56 ppm;
$\delta\omega_{1/2}$= 24 ppm

Al5.92

ω = 55 ppm,
$\delta\omega_{1/2}$= 23 ppm

ω = 56 ppm;
$\delta\omega_{1/2}$= 25 ppm

Al2.96

0   10   20   30   40   50   60   70   80   90   100   110   120
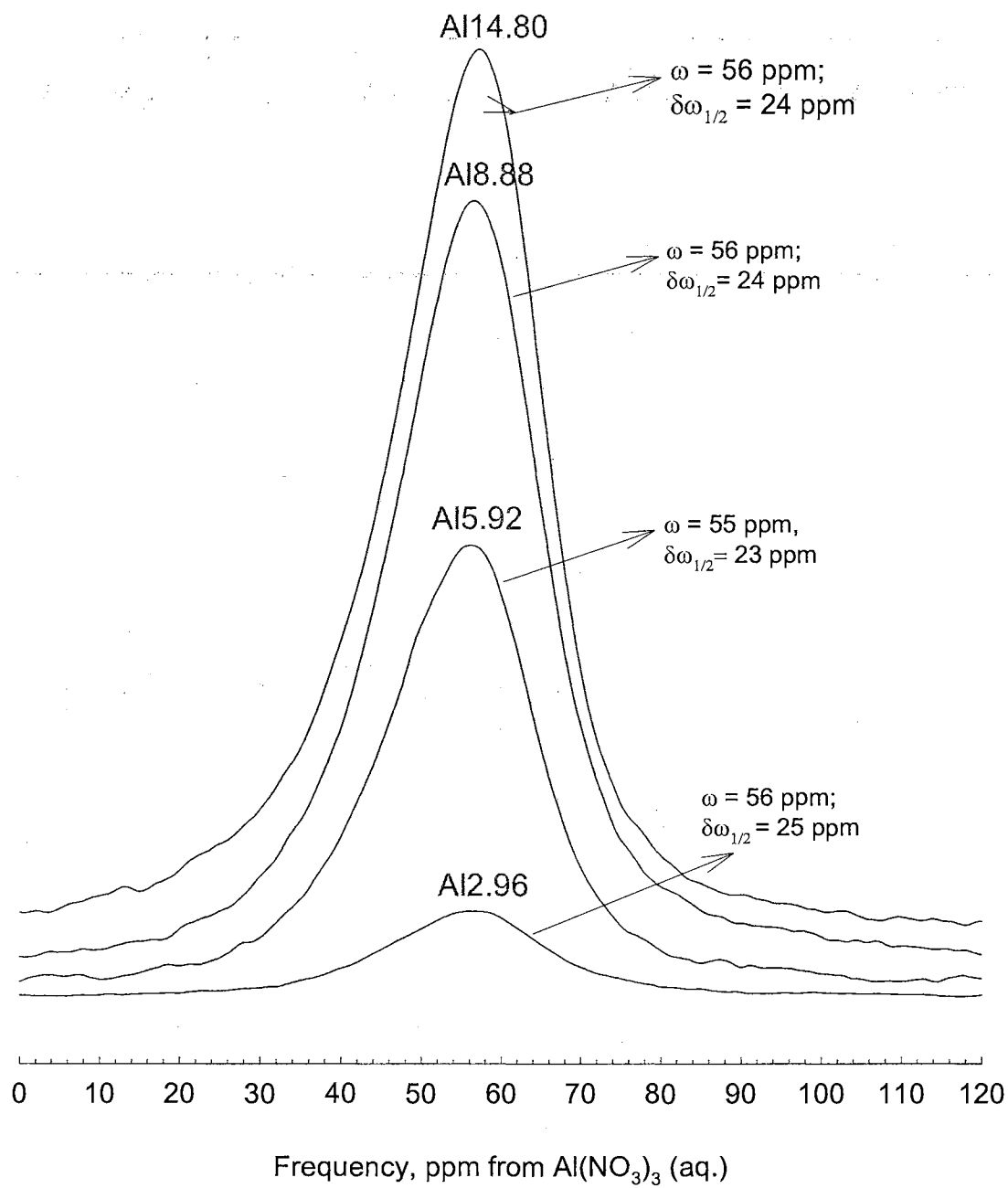
Frequency, ppm from $Al(NO_3)_3$ (aq.)

Fig. 37. ^{27}Al MAS NMR spectra of EDSMAS glasses of Al-series
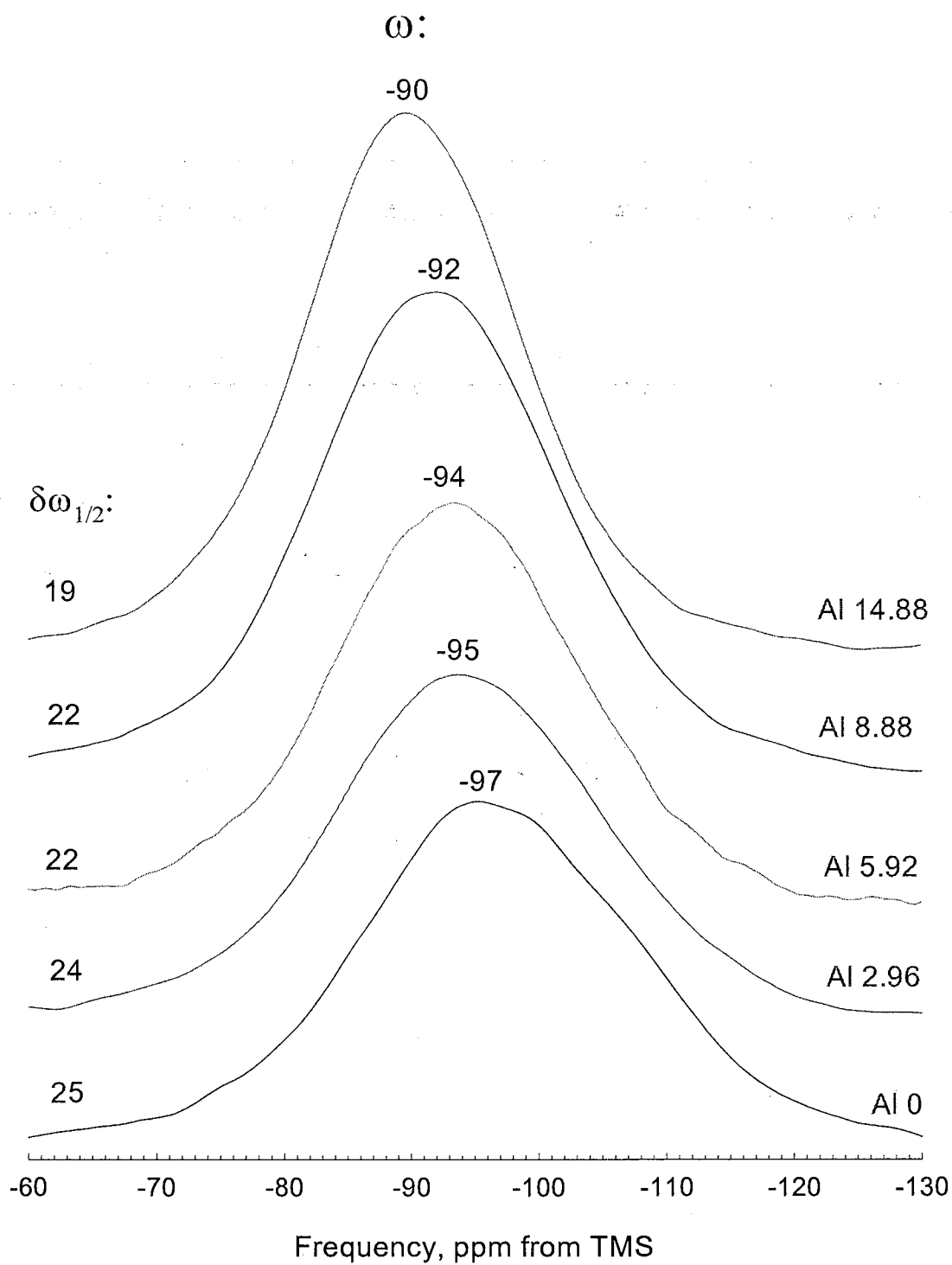
Fig. 38. ^{29}Si MAS NMR spectra of EDSMAS glasses of Al-series

presence of $Q^4(0Al)$ species [81]. For binary alkali silicate glass the chemical shift is at -89 ppm for $Q^3(0Al)$ species [134], while for binary alkaline silicate glass it is at -93 ppm [119]. These chemical shift ranges suggest that for more complex system like alkali alkaline rare earth doped silicate system, i.e. our Al0 glass, the ^{29}Si peak would be centered at even more negative chemical shift value. This is indeed the case: the ^{27}Al peak is centered at -97 ppm for the predominance of $Q^3(0Al)$ species for Al0 glass sample, which is in agreement with the predominance of the $Q^3(0Al)$ species deduced from the height of the Raman band at 1110 cm^{-1} (Fig. 35). With the replacement of silica by alumina the gradual shift of ^{29}Si band toward less negative values of the peak position from -97 to -90 ppm, indicating that the ^{29}Si nuclei become less magnetically shielded due to the appearance and successive height enhancement of the $Q^n(mAl)$ bands with $m = 1 - 4$ [55, 135, 136]. At 14.80 mole% of Al_2O_3 the ^{29}Si peak maximum is at $\sim$ -90 ppm. For alkali and alkaline earth aluminosilicate glasses with the concentrations of silica, alumina and modifying oxides similar to those of Al14.80 EDSMAS glass, the calculated distributions for $Q^n(mAl)$ units [136] suggest that there is significant contribution from $Q^4(2Al)$, $Q^3(0Al)$ as well as other aluminosilicate and silicate species which is in general agreement with our Raman results. According to the estimation of the NBO fraction (see Fig.1(b)), just 16.5% of all oxygens in this glass sample are actually non-bridging. However, to deduce the exact percentage of $Q^3(0Al)$ species formed due to this 16.5 % of NBOs, $Q^4(2Al)$ species formed due to 83.5 % of BOs as well as the contribution from other specific $Q^n(mAl)$ units to the ^{29}Si NMR envelope usually

represents a challenge in studying the amorphous materials and requires additional research.

The ^{29}Si peak linewidth becomes steadily narrower from -25 to -19 ppm with the increase of alumina-to-silica ratio which resembles the trend for ^{29}Si peak linewidth in CaO-Al$_2$O$_3$-SiO$_2$ glass [119] and other alkali and alkaline aluminosilicate glasses [85], [33] with the increase of Al$_2$O$_3$/SiO$_2$ ratio. The ^{29}Si linewidth decrease is in agreement with the chemical shift variation for the glasses due to an increase in the number of aluminum next-nearest neighbors to silicon [137]. This trend also can suggest a shift in reaction $Q^2 + Q^4 = 2Q^3$ to the right, that is more ordered with increasing Al content [33]. This is opposed to the results for Na- and K-aluminosilicates [106, 138], and confirms that the alkaline earths Mg^{2+} [139] and possibly rare earth Eu^{3+} present in the EDSMAS glass compete with Al for oxygens more efficiently than alkali Na$^+$ ions do, and will stabilize Q^3 tetrahedra with neighboring Al [138]. The shift of the above reaction to the right is in agreement with general reaction $Q^{n-1} + Q^{n+1} = 2Q^n$ with $1 \leq n \leq 3$ [140] for a distribution of species may be present in silicate glass. ^{29}Si line narrowing also is in agreement with the ordering of (Si,Al)$_3$ and (Si,Al)$_4$ ring structures in EDSMAS glasses deduced from RLS spectroscopy.

^{23}Na NMR spectra shown in Fig.39 demonstrate the presence of single broad slightly asymmetric peak at ~ -23 ppm, indicating sites with a range of quadrupolar coupling constants, asymmetry parameters and/or chemical shifts. The ^{23}Na resonance of sanidine is centered at -21 ppm and that of albite glass NaAlSi$_3$O$_8$ is centered at -18 ppm [82]. For ^{23}Na, compositional effects such as the ratio of NBOs

ω:

-23

-24

-23

-23

Al 14.80

Al 8.88

Al 5.92

Al 2.96

-100   -80   -60   -40   -20   0   20   40

Frequency, ppm from NaCl (aq.)
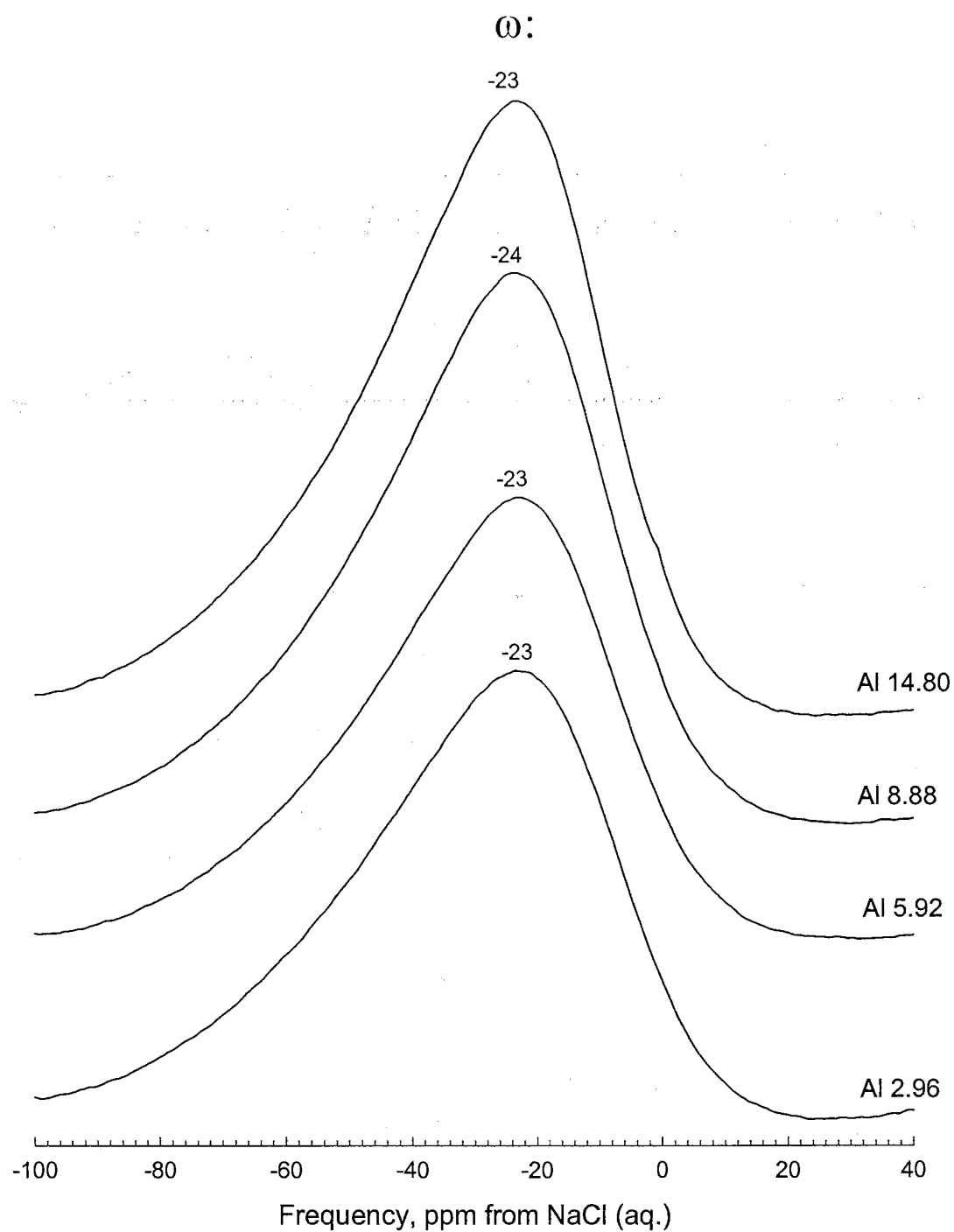
Fig. 39. ^{23}Na MAS NMR of EDSMAS glasses of Al-series

to tetrahedral cations are known to be important, probably in causing variations in next neighbor cation populations. However, with the increase of Al_2O_3/SiO_2 the resonance peak shift appears to be constant, which is in general agreement with the low sensitivity of the ^{23}Na resonance peak position to the variations in the topology of the silicate tetrahedral network [86]. Thus, it would be impossible to resolve two separate contributions from Na-O bonds in (i) Si-NBO and (ii) $[AlO_4]^-Na^+$.

5.2.5. The relation to holographic grating strength

The permanent change in the index of refraction as well as the ionic conductivity, increased linearly with Al_2O_3 concentration [7]. This trend in photorefractive efficiency was attributed to the reduced activation energy for forced diffusion of small modifiers bound to AlO_4^- clusters rather than to Si-NBOs. We also note that with the increase of Al amount, the concentration of Eu^{3+} ions is kept constant, therefore, the absolute values of FWM strength signal as a function of Al ions (Fig. 3) is lower than those of FWM strength signal as function of Eu ions (Fig. 2) by about a factor of 2. The increase of the EDSMAS glass hardness (elastic constants) measured by the BLS spectroscopy can contribute to the stability of the traps [73] for the hopping of weakly bound Na^+ ions due to silicon replacement by tetrahedral Al atoms, and therefore to the increased photorefractive grating efficiency.

5.3. Na-SERIES

5.3.1. Elastic parameters

The results of BLS measurements for Na-series are shown in Table 8. Measured Brillouin shifts (ω_L, ω_T), refractive indices n, density ρ and absorption coefficients are

Sample ID	ρ (g/cm^3)	ω_L (cm^{-1})	ω_T (cm^{-1})
Na9.86	2.50 ± 0.02	0.810 ± 0.003	0.488 ± 0.003
Na14.81	2.61 ± 0.02	0.800 ± 0.003	0.478 ± 0.003
Na19.73	2.64 ± 0.03	0.794 ± 0.003	0.469 ± 0.002
Na24.67	2.68 ± 0.03	0.791 ± 0.003	0.463 ± 0.002
Fused Silica	2.21	0.804	0.506

Sample ID	C_{11} (GPa)	C_{44} (GPa)	E (GPa)	B (GPa)	σ
Na9.86	84.7 ± 0.7	30.7 ± 0.4	74.6 ± 0.8	43.8 ± 0.2	0.216 ± 0.002
Na14.81	85.7 ± 0.7	30.6 ± 0.4	74.8 ± 0.8	44.9 ± 0.2	0.222 ± 0.002
Na19.73	84.9 ± 0.7	29.6 ± 0.4	73.0 ± 0.8	45.4 ± 0.3	0.232 ± 0.003
Na24.67	84.8 ± 0.7	29.0 ± 0.3	71.9 ± 0.7	46.1 ± 0.3	0.240 ± 0.003
Fused Silica	79.6	31.5	73.9	37.6	0.174

Table 8. Calculated elastic constants C_{11}, C_{44}, Young modulus E, bulk modulus B and Poisson ratio σ of Na-series based on the measured values of density ρ and Brillouin shifts ω_L, ω_T.

used to calculate elastic constants (C_{11}, C_{44}) using (2.1.10), Young's modulus E, bulk modulus B and Poisson ratio σ using (2.1.12). The decrease of such elastic parameters as C_{11}, C_{44}, E and the increase of Poisson's ratio σ (Fig. 40) clearly show that the glasses become softer with the increase of soda/silica ratio because Na^+ ions when introduced into the glass, substitute Si atoms in the tetrahedral network causing the formation of larger number of NBOs. The estimated ratio of NBOs is shown in Table 1(c). The increase of σ was also observed with the increase of magnesium modifier ions in aluminosilicate glasses [17]. However, the increase of bulk modulus in Fig. 40(a) indicates that the structural bonding rather less compressible in the volumetric sense. By definition, bulk modulus is the constant ratio of hydrostatic pressure exerted on the material to the volumetric strain which the sample undergoes. Such a behavior of bulk modulus can be explained by dramatic reduction of the free space by Na^+ modifiers substituting Si formers in the glass because sodiums have a large ionic radius ($R_{Na} \approx$ 1.02 Å) compared to atomic size of silicons ($R_{Si} \approx$ 0.26 Å) [100]. In addition, the enhancement of the glass density is observed (see Table 8). Thus, the concurrent appearance of weak Na^+-O bonds and increasing volumetric incompressibility take place in EDSMAS glasses with the increasing of soda/silica ratio.

5.3.2. Photoelastic constants

Based on calculated molar mass M of the EDSMAS glasses of Na-series and measured values of P_{12}, P_{44}, n, ρ we calculated LLE, LE, AE, α and G using (2.1.20), (2.1.21), (2.1.23) and (2.1.24). The results of these calculations along with the measured values of photoelastic constants P_{12} and P_{44} are listed in Table 9 and plotted in
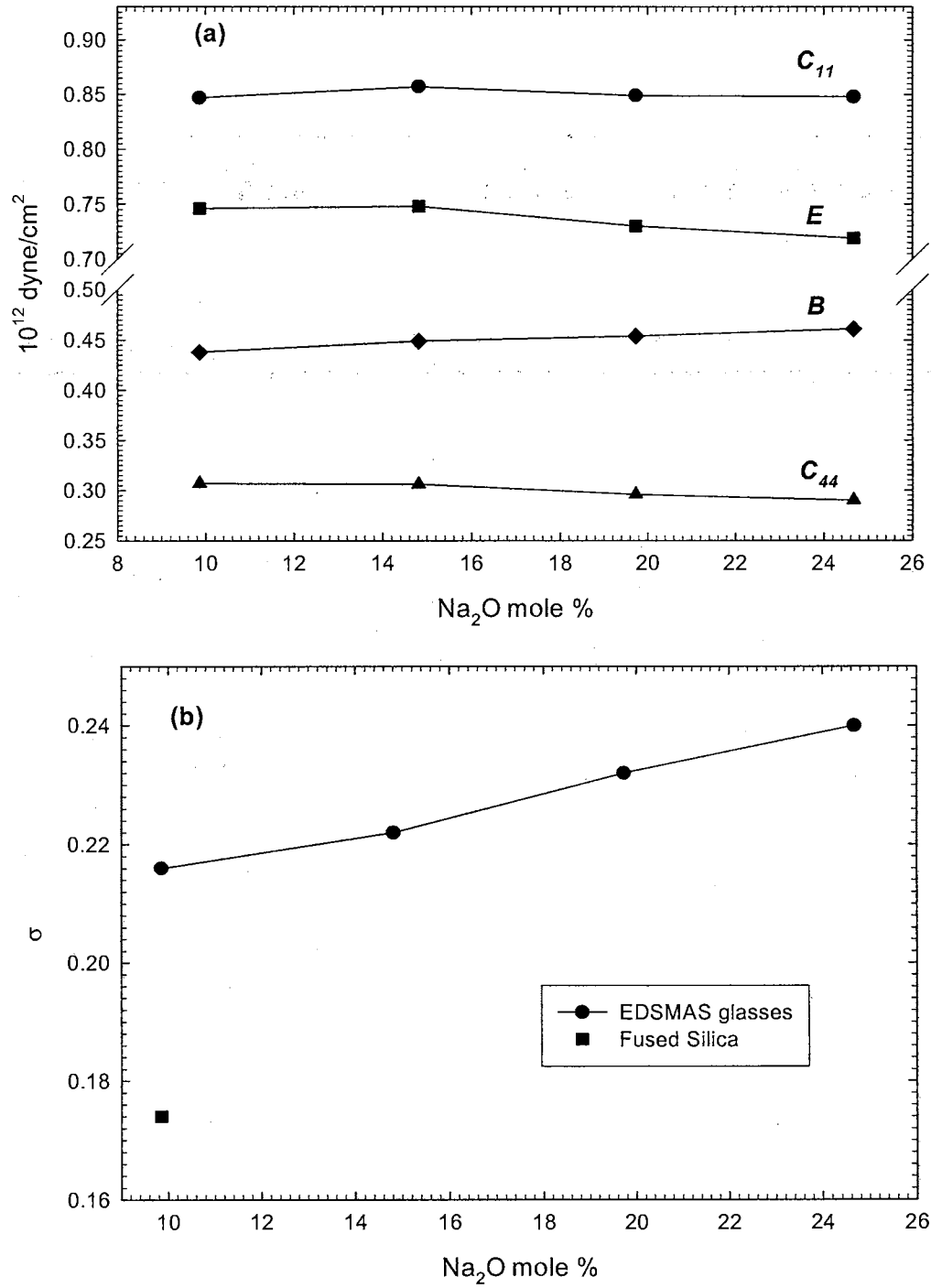
Fig. 40.(a) Compressional C_{11}, shear C_{44}, Young E and bulk B moduli;

(b) Poisson ratio σ versus Na_2O mole%

Sample ID	α_a (cm^{-1})	P_{12}	P_{44}	M (g/mole)	n
Na9.86	0.30±0.01	0.204±0.007	-(0.048±0.003)	62.844	1.519±0.005
Na14.81	0.76±0.01	0.251±0.009	-(0.056±0.004)	62.938	1.524±0.005
Na19.73	0.55±0.01	0.244±0.008	-(0.052±0.004)	63.031	1.528±0.005
Na24.67	0.76±0.01	0.228±0.008	-(0.049±0.003)	63.124	1.535±0.005
Fused Silica	0.04	0.279	-0.078	60.086	1.462±0.005

Sample ID	α (10^{-23}cm^3)	G (10^{23}cm^3)	LLE	LE	AE
Na9.86	0.195±0.009	2.99±0.16	0.547±0.005	-(0.064±0.001)	-(0.112±0.001)
Na14.81	0.168±0.008	3.69±0.18	0.615±0.007	-(0.065±0.001)	-(0.119±0.001)
Na19.73	0.169±0.008	3.55±0.17	0.610±0.006	-(0.065±0.001)	-(0.118±0.001)
Na24.67	0.178±0.008	3.25±0.17	0.579±0.006	-(0.066±0.001)	-(0.115±0.001)
Fused Silica	0.150	5.27	0.678	-0.057	-0.134

Table 9. Calculated values of LLE, LE, AE, α and G of Na-series based on the measured values of absorption coefficient α_a, photoelastic constants P_{12} and P_{44}, index of refraction n, density ρ, calculated molar mass M.

116

Figs. (41-43) versus Na_2O mole %. The values of the measured absorption coefficient α_a used for calculating P_{12} and P_{44} are listed in Table 9 as well. Starting from 14.81 mole % of Na_2O we observe monotonous decrease (increase) of P_{12} and LLE (P_{44}) because of the increase in polarizability α, the increase in density ρ and the increase in the refractive index n. The increase in the polarizability is in agreement with Poisson's ratio data shown in Fig. 40(b). The magnitude of the correlation integral G diminishes as seen in Fig. 42(b) because of the presence of strong r^{-4} dependence in the correlation integral. It has been shown for Na_2O-SiO_2 glasses that $r_{Si-O} = 1.62$ Å and $r_{Na-O} = 2.40$ Å [108, 109]. Therefore, it is this difference in bond lengths of Al-O and Si-O which we think is responsible for the decrease of the correlation integral G. From Fig. 43 we see that $|LE| < |AE| < LLE$, i.e. the largest contribution to P_{12} values comes from the first term, Lorentz-Lorentz effect (LLE), i.e. the term which accounts for the change of refractive index due to local density changes accompanying the light induced strain. Besides, the lattice effect (LE) is smaller than the atomic effect (AE) because it is easier to distort individual atomic sites than the group of atoms (lattice).

5.3.3. RLS Spectroscopy

Unpolarized Raman spectra for the EDSMAS glasses with various Na_2O concentrations are shown in Fig. 44. The Raman peak intensities are a function of not only the number of vibrating modes but also bond polarizabilities, therefore only the relative changes in abundances of various Q^n species with varying Na content can be deduced from changes in the Raman peak intensities. The structure of EDSMAS glass
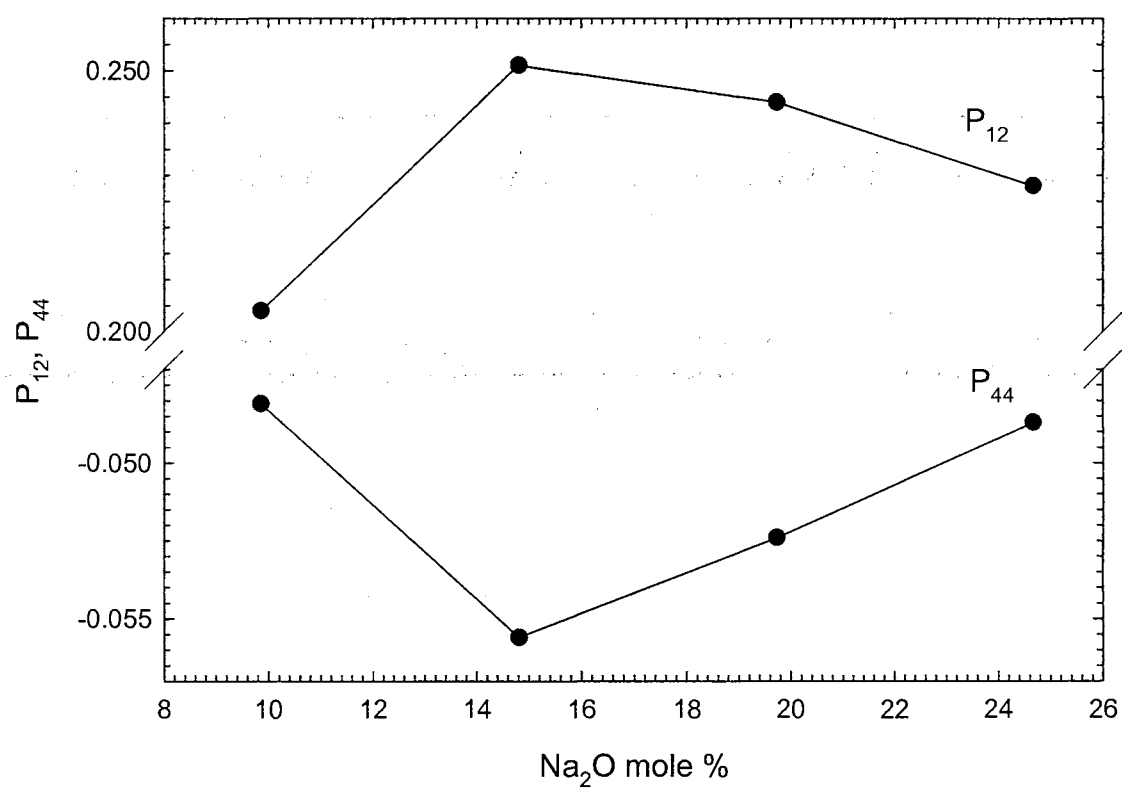
Fig. 41. Photoelastic constants P_{12} and P_{44} versus Na_2O mole%
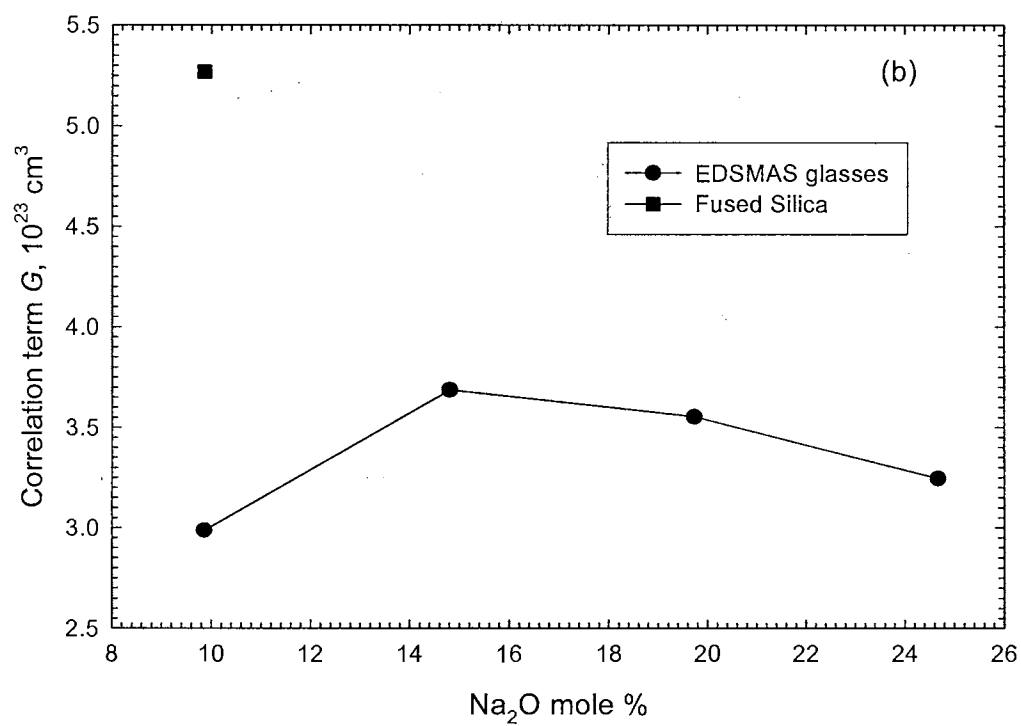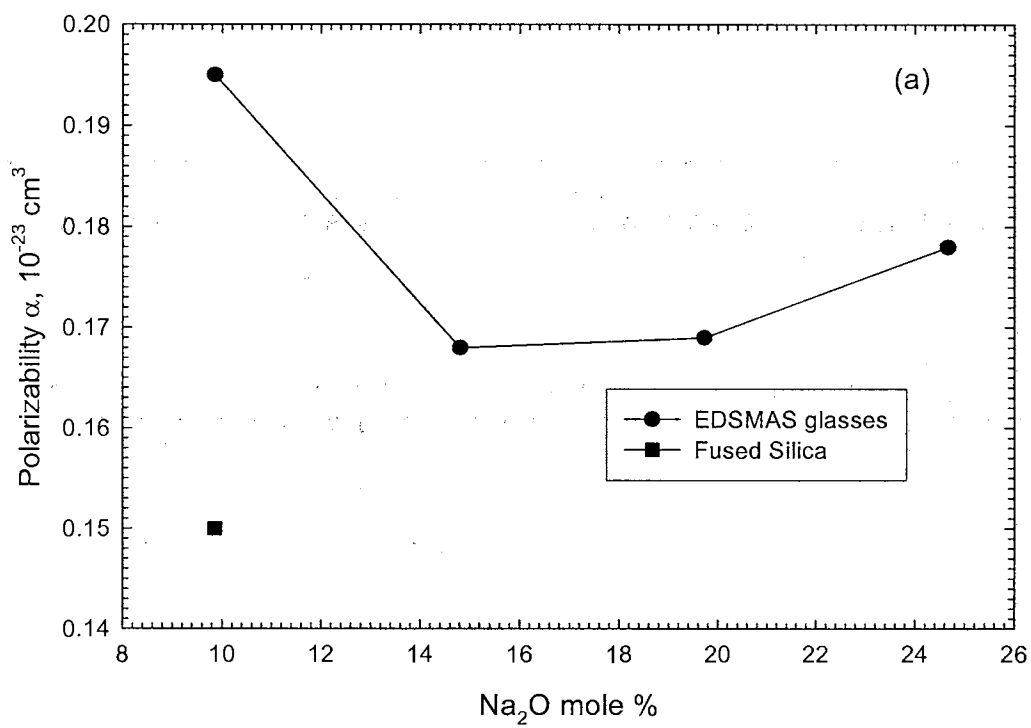
Fig. 42. (a) Polarizability α and (b) the correlation integral G versus Na_2O mole%
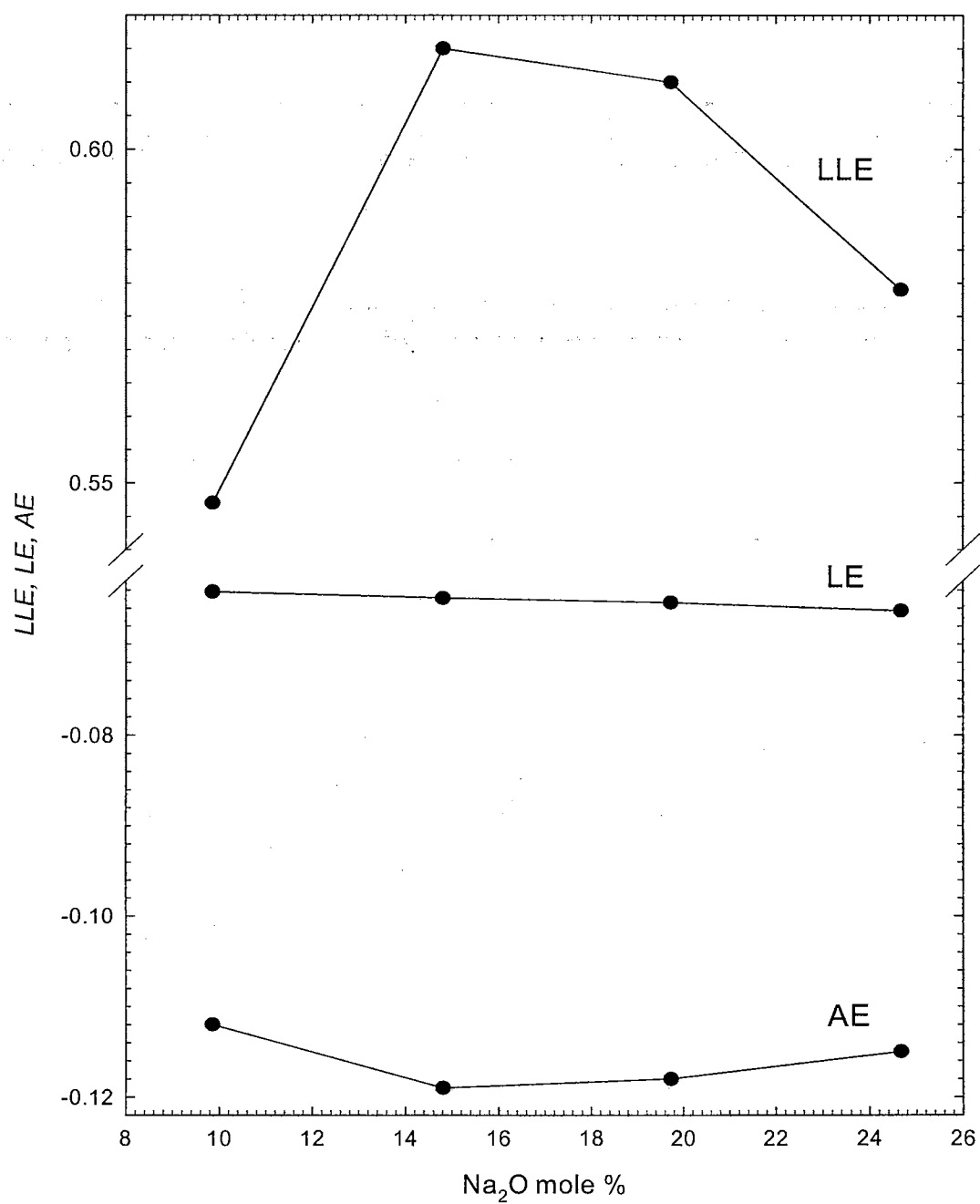
Fig. 43. Lorentz-Lorentz effect (*LLE*), lattice effect (*LE*) and

atomic effect (*AE*) versus Na_2O mole%
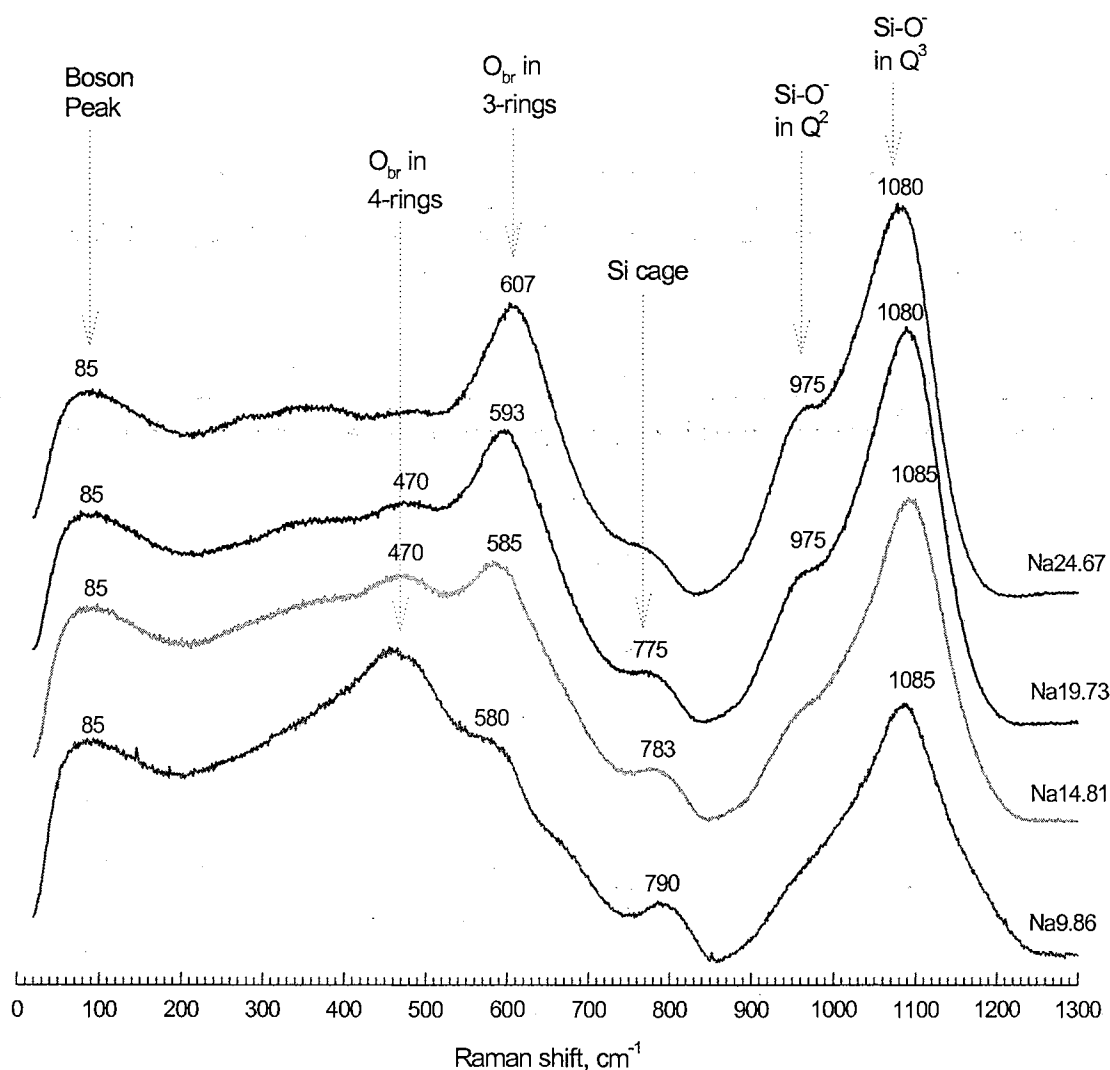
Fig. 44. Raman spectra of EDSMAS glasses of Na-series

becomes more depolymerized with the increase of sodium concentration which is observed in the high-energy Raman spectrum: two partially resolved peaks at 1100 cm^{-1} and 975 cm^{-1} increase in intensity compared to the intensity of 790 cm^{-1} band. These peaks attributed to Q^3 and Q^2 species, respectively, become more distinct from each other with the increase of Na_2O/SiO_2 ratio, which implies that more narrow distribution

121

of Q^n species takes place, i.e. the overall structure tends to be more ordered. This observation is in agreement with previous studies of rare-earth aluminosilicate glasses [20, 22, 30] and rare-earth alkaline silicate glasses [112]. This interpretation of the spectra is also in agreement with the contention of Brawer and White [113], who suggested that low field strength modifier ions lead to more ordered structures. We need to note that the height of 975 cm^{-1} band increases gradually with respect to that of 1100 cm^{-1} band, implying that the number of Q^2 species increases slightly compared to that of Q^3 ones. However, throughout the Na-series Q^3 species still remain the predominant silicon tetrahedral units.

Based on EDSMAS glass composition, the NBOs formed in Na-series are due to Na^+, Mg^{2+} and Eu^{3+} cations, i.e. Q^3 and Q^2 species in this case are represented by (Q^3-Mg, Q^3-Na, Q^3-Eu) and (Q^2-Mg, Q^2-Na, Q^2-Eu) units. The 1100 cm^{-1} band is dominant indicating the preponderance of Q^3-Mg, Q^3-Na and Q^3-Eu species in these glass samples with Q^3-Na being predominant tetrahedral unit. With the increase of the alkali content at the expense of the silica content, the whole Raman envelope at (850-1240) cm^{-1} does not shift toward lower wave-numbers which is expected because the number of alkali earth and rare earth modifiers is kept constant, i.e. the contribution of Q^3-Eu at ~ 1030 cm^{-1} [118] and Q^3-Mg species at ~1060 cm^{-1} [19, 118] will be small compared to Q^3-Na at 1100 cm^{-1}. The development of contributions from Q^1 (~ 900 cm^{-1}) and Q^0 (~ 850 cm^{-1}) [110] will be considered negligible. In Table 1(c) we have estimated the total fraction of NBOs ($R_{Total\ NBO}$) due to the presence of Na^+, Mg^{2+} and Eu^{3+} ions. This trend in the estimated total ratio of NBOs vs. Na_2O content supports the increase in amplitude of the Raman peaks at 975 cm^{-1} and 1100 cm^{-1}.

The pronounced intensity increase of the 580 cm^{-1} Raman band assigned to the bridging oxygen breathing mode in both three-member pure silicate (Si,Si)$_3$ [114] and aluminosilicate (Si,Al)$_3$- rings [34, 115] with increasing Na$^+$ can be understood as follows. The depolymerization of EDSMAS glass due to sodium incorporation is accompanied by the rapid growth of small ring structures: three-member pure silicate and aluminosilicate rings. The band at 470 cm^{-1} attributed to the bridging oxygen breathing mode in both pure silicate- [114] and (Si,Al)-four member rings [115] is not affected, probably because sodium ions entering into the glass cause the appearance of small ring structure fragments rather than large ones. Thus, the height of the 580 cm^{-1} is very sensitive to the degree of depolymerization of EDSMAS glass as in the case of Eu-series. The height of the Boson peak at $\sim$ 90 cm^{-1} is not affected by Na$^+$ ions as it in Eu-series probably because Na$^+$ modifier ions have lower field strength and ionicity compared to Eu^{3+} ions [117]. It should be noted, however, that Boson peak is sensitive to the identity of alkali ion in the family of Eu^{3+} doped alkali alkaline silicate glasses [141].

5.3.4. Solid-State NMR Spectroscopy

^{27}Al NMR spectra of EDSMAS glasses of Na-series are shown in Fig. 45. There is gradual shift toward more positive values of chemical shift from 53 to 62 ppm, which is evidence for aluminum nuclei to become less shielded. Moreover, the width of the ^{27}Al envelope slightly narrows from 24 to 22 ppm. Since with the increase of

ω = 62, Δω$_{1/2}$ = 22   Na 24.67%

ω = 61, Δω$_{1/2}$ = 24   Na 19.73%

ω = 56, Δω$_{1/2}$ = 25   Na 14.80%

ω = 53, Δω$_{1/2}$ = 24   Na 9.86%

-100   -50   0   50   100   150   200

Frequency, ppm from Al(NO$_3$)$_3$ (aq.)
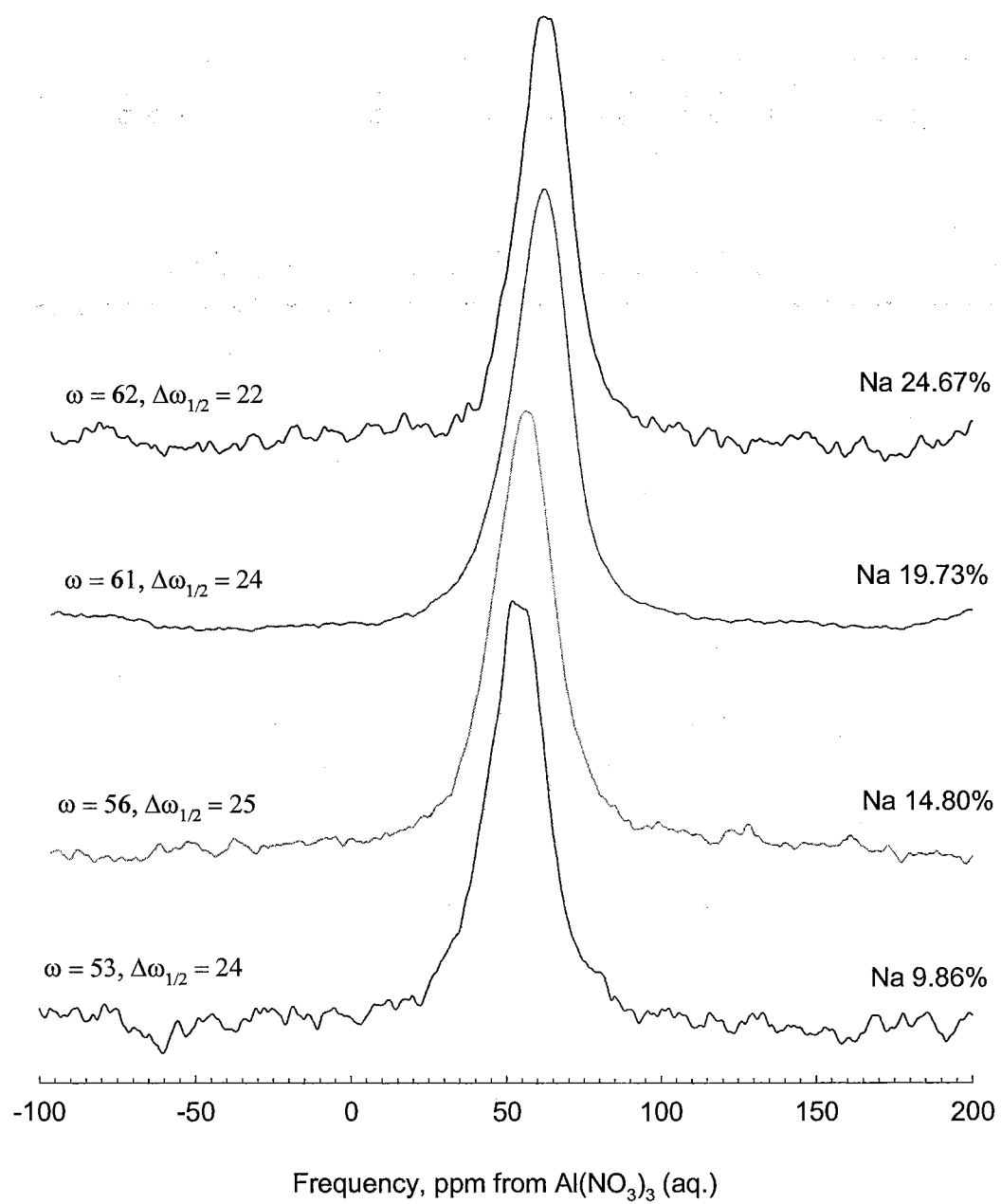
Fig. 45. ^{27}Al MAS-NMR spectra of EDSMAS glasses of Na-series

Na_2O/SiO_2 ratio, the Al_2O_3 content is kept constant, therefore, we effectively decrease Si/(Si+Al) ratio. The latter effect was observed in aluminosilicate glasses [85] and parallels the variation for [27]Al peak maxima in framework aluminosilicate crystals [142]. The data for model crystalline aluminosilicates [143] indicate that the progressive deshielding at Al with decreasing Si/(Si+Al) for our glasses is due to a progressive decrease in the mean Al-O-Si angle per tetrahedron, at least for compositions with few Al-O-Al linkages. This decrease in the mean Al-O-Si angle could simply be due to a decreasing Si/(Si+Al) ratio, but is also fully consistent with a decrease in the average number of tetrahedra per ring as observed from the enhancement of the 580 cm^{-1} Raman peak in Fig. 44 and as suggested by [144].

The ^{29}Si NMR spectra of the framework Na-series EDSMAS glasses are the progressively deshielding of the peak maximum (progressively less negative chemical shifts from -102 to -89 ppm) with decreasing SiO_2/Na_2O ratio (see Fig. 46). This trend is in agreement with the less negative values of the chemical shift ranges for $Q^n(0Al)$ species with higher n, i.e. in the glass with higher degree of depolymerization. The range of shifts from -102 to -89 ppm corresponds to the majority of $Q^3(0Al)$ species [55, 137] which fully agrees with our Raman high energy data.

^{23}Na NMR spectra of Na-series are shown in Fig. 47. [23]Na nuclei become less shielded because the peak shift changes from -26 to -17 ppm. The resonance peak shift and the number of NBO per tetrahedron (NBO/T) may actually be related to the number of first neighbor network-modifiers. An increase in their number (and

ω = −89

Na24.67

ω = − 93

Na19.73

ω = − 95

Na14.80

ω = −102

Na9.86

100   50   0   -50   -100   -150   -200   -250   -300
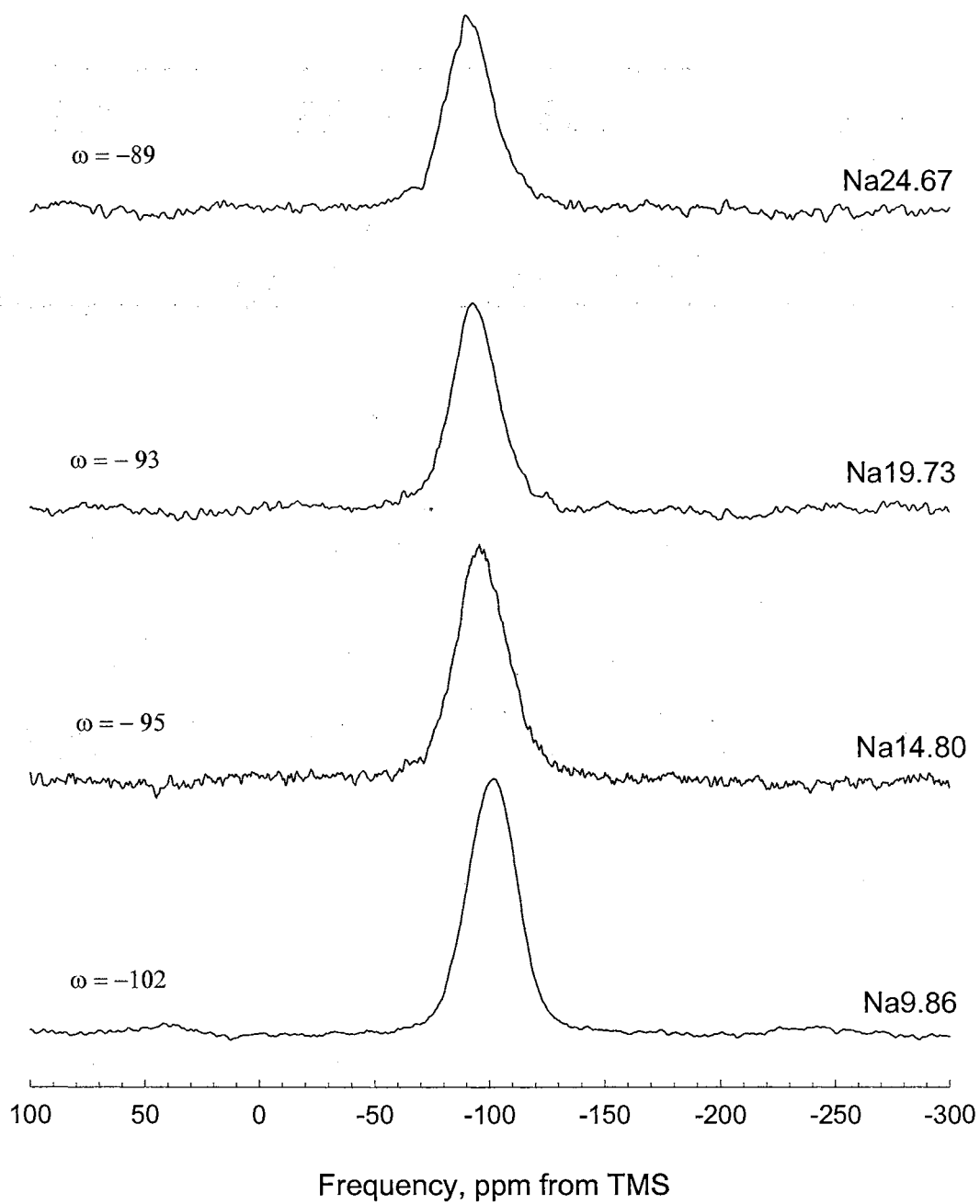
Frequency, ppm from TMS

Fig. 46. ^{29}Si NMR spectra of EDSMAS glasses of Na series
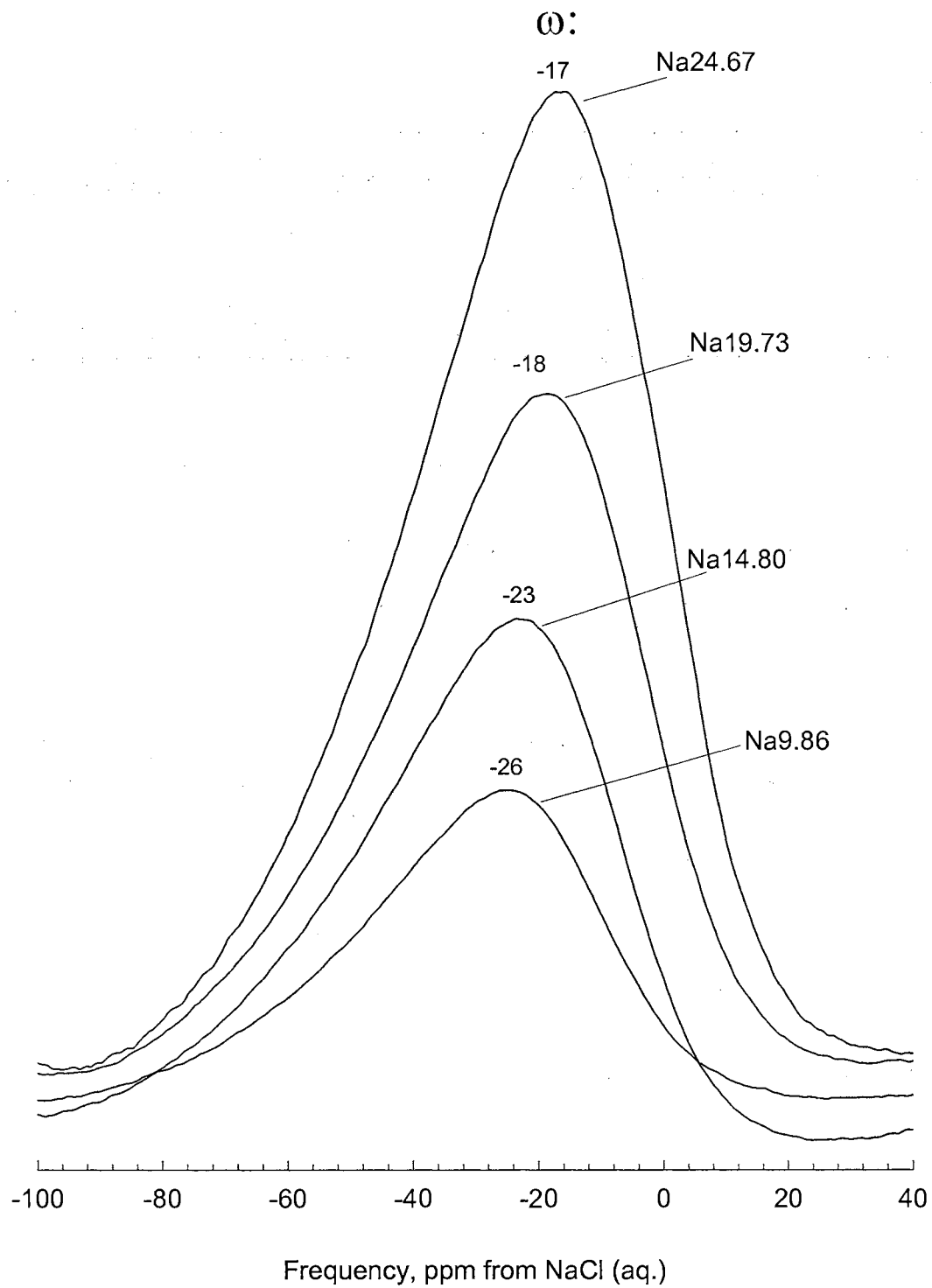
Fig. 47. ^{23}Na MAS NMR spectra of EDSMAS glasses of Na-series

therefore an increase in NBO/T) may result in the decrease of the positive charge on the central Na^+ (higher electron density) and thus an increase in its chemical shift [86]. It is also worth noting the relatively tight correlations between the ^{23}Na chemical shift, the mean Na-O distance and Na coordination: the less negative values of chemical shift correspond to shorter mean Na-O bond lengths and lower Na coordination [86].

5.3.5. The relation to holographic grating strength

The decay in the photorefractive grating strength was observed [145] for EDSMAS glasses with Na_2O with slight changes in Al_2O_3 and MgO concentrations. The main reason for non-increasing trend in nonlinear Δn was attributed to non-changing pumped Eu^{3+} ion concentration. Another reason can be the supply of holographically inefficient Na^+ modifier ions (strongly bound sodiums available through formation of NBO at the site of depolymerized silica tetrahedra). The number of holographically more efficient light modifiers (weakly bound Na^+ ions bound to AlO_4^- tetrahedra) will be small and constnat since Al_2O_3 amount is fixed at 2.96 mole %. The decrease of the EDSMAS glass hardness (elastic constants) measured by the BLS spectroscopy may also contribute to the destabilization of the traps [73] for the hopping of Na^+ ions and therefore to the decreased photorefractive grating efficiency.

CHAPTER VI

CONCLUSIONS

In the present dissertation using laser light (Brillouin and Raman) scattering and solid-state NMR spectroscopic studies we have studied structural, vibrational, elastic and photoelastic properties of EDSMAS glasses as a function of content of individual oxide components: Eu_2O_3, Al_2O_3 and Na_2O to provide new knowledge related to the mechanism underlying the formation of holographic gratings in these glassy photorefractive materials during FWM experiment. The acoustic and optical phonon vibrations ranging from 0.4 cm^{-1} to 0.9 cm^{-1} and from 50 cm^{-1} to 1300 cm^{-1}, respectively, were studied. ^{29}Si, ^{27}Al and ^{23}Na MAS NMR spectroscopies were used to probe the environment of Si and Al glass network formers and Na^+ network modifiers. The main characterization results of these studies are published in [18, 19] and reported at conferences [146-151].

The intermediate structural order in EDSMAS glass is determined in large part by the distribution of NBOs and the partitioning of Al among the various Q^n sites. Si and Al atoms were found to be in tetrahedrally coordinated sites. No Al was observed in 6- or 5- coordinated sites. The increase of the 580 cm^{-1} Raman band's frequency was found to be due to introduction of modifying ions, while the decrease of the Raman mode's frequency is due to addition of glass network formers. The overall bonding in all three EDSMAS glass series becomes more polarizable compared to fused silica. The depolymerization (polymerization) of the EDSMAS glass is mainly characterized by the presence of NBOs (BOs) and three (four) member silicate and aluminosilicate rings. Observed photoelastic constants described by Carleton-Matusita theoretical expressions

are discussed in terms of such structural variations as average polarizability, density, index of refraction, absorption coefficient, molar mass, bond lengths, Lorentz-Lorentz effect, lattice effect and atomic effect. The Lorentz-Lorentz effect was the dominant contribution to the photoelastic constant P_{12}. The lattice effect was found smaller than the atomic effect because it is easier to distort individual atomic sites than the group of atoms. The decrease of the correlation integral related to radial distribution function was attributed to the bond length dilation.

6.1. Eu-SERIES

BLS studies revealed that the EDSMAS glass becomes harder due to doping of Eu^{3+} (ions with largest ionic radius), their high coordination and their enhanced field strength with oxygens. In addition, the overall bonding becomes more ionic because Eu^{3+} ions cause the formation of larger number of NBOs and higher ionicity of Eu-O bonds. Spectral changes in the Raman envelope at (840-1240) cm^{-1} indicate that the number of silica tetrahedra with more than one non-bridging oxygen (NBO) per tetrahedron and the number of silica tetrahedra with one NBO associated with Eu increase with increasing rare-earth concentration, so the overall structure becomes more depolymerized and disordered. The depolymerization was also observed because of the increase in the number of three-member silicate and aluminosilicate rings. ^{29}Si MAS NMR spectra show a single broad peak with maxima at frequencies attributable to a predominance of Q^3 species. ^{27}Al and ^{29}Si NMR spectroscopies show that aluminum and silicon species become less observable as Eu_2O_3 content increases, presumably due to interactions with paramagnetic europium. The ^{27}Al NMR spectra reveal the presence

of only tetrahedrally coordinated Al sites, with a gradual increase in the structural disorder associated with these sites as the concentration of Eu_2O_3 increases. [23]Na sites are affected by paramagnetic effect and depolymerization. The increased ionicity due to rare-earth doping enhances the amplitude of the Boson Raman peak. The enhanced relaxation by the paramagnetic Eu^{3+} ions broadens the width of [29]Si peak more than that of [27]Al.

The increase of the photorefractive grating strength is attributed to the increased number of pumped rare earth ions, the increase in the amount of high-energy phonons liberating light modifiers migrating through the network, the increase in the hardness causing enhancement in the stability of traps for migrating ions. Slow growth of the grating efficiency at higher Eu^{3+} concentration can be due to passive role of introduced rare-earths causing the increase in the light ions activation energy as well as due to the formation of highly depolymerized SiO_4 tetrahedra because of rare earth clustering.

6.2. Al-SERIES

From RLS and ^{29}Si MAS NMR spectra we demonstrate the development of $Q^n(mAl)$ species, i.e. the overall number of BOs increases due to formation of new Si-O-Al bridges and recovering of Si-O-Si bridges by removal of modifying ions from Si-NBO bonds to compensate the charge of $[AlO_4]^-$ sites. Even at highest alumina (14.88 mole %) content our glass connectivity is mostly governed by Si-O-Si linkages. These processes are accompanied by the development of more polymerized network in the form of $(Si,Al)_4$-member rings rather than fragmental structure in the form of $(Si,Al)_3$-member rings with Al in tetrahedral coordination. They are all supported by the

enhancement of the glass hardness measured by BLS and attributed mostly to the capturing of free space by Al replacing Si. Observed by BLS concurrent increase in Poisson ratio and glass polarizability was attributed to the formation of more ionic $[AlO_4]^-M$ bonds compared to those of Si-O$^-$M. Thus, Al concentration-induced transfer of modifying ions from SiO_4 toward AlO_4 tetrahedra plays an important dual role: polarizing the structure of the EDSMAS glass and causing it to be harder. The trend in the enhanced photorefractive efficiency was attributed to the reduced activation energy for forced diffusion of small modifiers bound to AlO_4^- clusters rather than to Si-NBOs and due to increased stability of the traps for migrating light modifiers.

6.3. Na-SERIES

Substitution of soda for silica bringing about a degradation of glass structure is evidenced by the formation of structurally distinct Q^3 and Q^2 species as shown by RLS. Q^3 units remain predominant ones which is also supported by ^{29}Si NMR data. The increased depolymerization of the network is also in tandem with the concurrent formation of more fragmental (three-member) pure silicate and aluminosilicate rings and deshielding of ^{27}Al nuclei. ^{23}Na nuclei are deshielded by the first neighbor network modifier Na ions, which cause the shortening of Na-O bond length and lowering of Na coordination for the probed Na ion. The unique feature about the EDSMAS glass is that the structure becomes less incompressible from bulk modulus point of view, which is explained by the larger volume occupied by Na^+ ions incorporated into the glass compared to that of Si atoms, the increase of density and molar mass. Measured by BLS, the increase in the polarizability of the EDSMAS glass structure is mostly due to

formation of Si-O⁻Na⁺ bonds which are more ionic than Si-O-Si bonds. The non-increasing photorefractive grating strength was observed because of the non-changing concentration of pumped Eu^{3+} ions, the supply of holographically inefficient (strongly bound) Na^+ ions and the decrease of the measured EDSMAS glass hardness contributing to the destabilization of the traps for the hopping of Na^+ ions.

CHAPTER VII

RECOMMENDATIONS FOR FURTHER RESEARCH

RLS is a powerful tool for the analysis of glass structures. No other technique, for instance, is as sensitive for distinguishing between bridging and non-bridging oxygens or for detecting small proportions of specific ring units in the structures of aluminosilicate glasses. However, Raman bands themselves do not constitute unequivocal "fingerprints" of specific structural units in the spectra of EDSMAS glasses. Because of this fact, and also the breadth and weakness of Raman bands in these materials, many controversies have arisen over band assignments. It is only by consideration of all the available data, including Raman band polarization characteristics, relative Raman cross-sections, spectral effects of isotopic and atomic substitutions, comparison with model calculations, comparisons with spectra of crystalline polymorphs including the spectral changes at the melting point, changes in band shape and position with temperature and pressure and supporting data from other analytical techniques such as IR absorption and emission, hyper-Raman scattering, EXAFS, NMR, BLS and Mossbauer spectroscopy, among others – that such controversies may be satisfactorily resolved. It would be nice to have more samples in all three series with larger content of Eu_2O_3, Al_2O_3 and Na_2O in each series, respectively, to study extended effect of glass component concentration on EDSMAS glass structure and properties. Higher resolution solid-state NMR with the large field strengths (> 11 Tesla) is needed to get detailed picture on Al coordination including possible existence of 6- and 5-fold coordinated Al sites. BLS studies from

magnons at low temperatures will shed more light on the paramagnetic nature of EDSMAS glasses.

During the photorefractive process each of the two incident write interfering beams $\overrightarrow{k_1^{inc}}$ and $\overrightarrow{k_2^{inc}}$ induce Brillouin scattered waves $\overrightarrow{k_1^{scat}}$ and $\overrightarrow{k_2^{scat}}$, respectively. The latter ones are Bragg-diffracted from the moving acoustic waves $\overrightarrow{q_1}$ and $\overrightarrow{q_2}$. On the other hand, $\overrightarrow{k_1^{inc}}$ and $\overrightarrow{k_2^{inc}}$ beams interference yields the refractive index grating wave vector $\overrightarrow{k_{grating}}$ proportional to the vector difference between acoustic waves $\overrightarrow{q_1}$ and $\overrightarrow{q_2}$ as follows: $\overrightarrow{k_{grating}} = \overrightarrow{k_1^{inc}} - \overrightarrow{k_2^{inc}} \propto \overrightarrow{q_1} - \overrightarrow{q_2}$. Thus, such simple kinematics wave vector relation implies that there should be structural correlation between holographically light-induced refractive index changes and acoustic wave induced-strain changes due to Brillouin light scattering (BLS) process in isotropic glass. The correlation between a propagating bulk acoustic wave and a stored volume hologram has been achieved in LiNbO$_3$ [152]. For cubic photorefractive piezocrystals the influence of photoelastic constants values on the light diffracted by holographic gratings has already been demonstrated [153]. Further theoretical studies are needed to reveal the detailed physics behind the structural correlation between the holographically light-induced refractive index changes and acoustic wave induced-strain changes due to BLS process in isotropic glass.

BIBLIOGRAPHY

[1] F.M. Durville, *et al.,*, Phys. Rev B 34, 4213, (1986)

[2] F.M. Durville, *et al.,* Phys Rev B, 35(8), p. 4109, (1987)

[3] E.G. Behrens, *et al.,* Applied Optics, 29(11), 1619, (1990)

[4] M.M. Broer, *et al.,*, Phys. Rev. B 45, 7077, (1992)

[5] A.Y. Hamad, J.P.Wicksted, G.S. Dixon, Optical Materials, **12**, 41 (1999)

[6] A.Y. Hamad, J.P Wicksted, R. Ascio, J.J. Martin, C. Hunt and G.S. Dixon, J. Appl. Phys., 92(5), 2235-2241, (2002)

[7] A.Y.Hamad, J.P.Wicksted, M.R. Hogsed, J.J. Martin, C.A. Hunt and G.S. Dixon, Phys Rev B, (2002), **65**, 064204-1

[8] A.Y. Hamad, J.P. Wicksted, Applied Optics, 40(11), 1822-1826, (2001)

[9] G.S. Dixon, A.Y. Hamad and J.P. Wicksted, Phys. Rev. B 58 (1), 200, (1998)

[10] K. Fujita *et al*, J. Opt. Soc. Am. B, 15(11), 2700-2705, (1998)

[11] K. Fujita *et al*, J. Luminescence ,98(1-4), 295-300, (2002)

[12] B.G. Potter Jr. and A.J. Bruce, *"Synthesis and Application of Lanthanide-doped materials"*

[13] J.T. Kohli, Key Engineering Materials, 94-95, 109-124, (1994)

[14] L-G Hwa *et al*, Mater. Res. Bulletin, 35, 1285-1292, (2000)

[15] Delbert E. Day, *Glass Researcher*, p.5, Winter (1995)

[16] E.M. Erbe, D.E. Day, J. Am., Ceram. Soc., 73(9), 2708-13, (1990)

[17] F. Schilling, *et al.,* Contrib. Mineral. Petrol., 141, 297-306, (2001)

[18] G-Q. Shen, Z.N. Utegulov, J.P. Wicksted, Phys. Chem. Glasses, 43(2), 73-9, (2002)

[19] Z.N. Utegulov, M.A. Eastman, S. Prabakar, K. T. Mueller, A.Y. Hamad, J.P. Wicksted and G.S. Dixon, J. Non-Cryst. Solids, 315 (1-2), 43-53, (2003)

[20] J.T. Kohli, *et al.*, Phys. Chem. Glasses, 34(3), 81, (1993)

[21] S-L. Lin, C-S. Hwang, J. Non-Cryst. Solids, 202, p.61, (1996)

[22] T. Schaller, J. F. Stebbins, J. Phys. Chem., B 102, 10690, (1998)

[23] C.H. Hsieh, H.J. Jain, J. Non-Cryst. Solids, 183, p.1, (1995)

[24] A. Rahman, *Master Thesis*, Oklahoma State University (2000).

[25] W-C. Wang, Y. J. Chen, J. Appl. Phys., 79, p. 3477, (1996)

[26] S. Tanabe, *et al.*, J. Am. Ceram., Soc., 73, p. 1733, (1990)

[27] S. Tanabe, *et al*, J. Am. Ceram. Soc. 75(3), 503-506, (1992)

[28] J. T. Kohli and J. E. Shelby, Phys. Chem. Glasses, 32(3), 109, (1991)

[29] C.B. Layne, *et al*, Phys. Rev. B16(1), 10, (1976)

[30] J.T. Kohli, *et al.*, Phys. Chem. Glasses, 33(3), 73, (1992)

[31] N.J. Clayden *et al*, J. Non-Cryst. Solids, 258, p.11-19, (1999)

[32] S. Prabakar *et al.*, Eur. J. Solid State Inorg. Chem. 29, 95-110, (1992)

[33] C. I. Merzbacher, *et al.*, J. Non- Cryst. Solids, 124, 194 – 206, (1990)

[34] P. F. McMillan *et al.*, J. Non- Cryst. Solids, 226, 239 – 248, (1998)

[35] A. Klonkowski, Phys. Chem. Glasses, 24 (6), 166-170, (1983)

[36] A.K. Varshneya *"Fundamentals of inorganic glasses"*, Academic Press, (1994)

[37] J.F. Nye, *Physical properties of Crystals*, (Clarendon, Oxford 1957)

[38] P.K. Das and C.M. DeCusatis, *"Acousto-Optic Signal Processing: Fundamentals & Applications"*, Artech House, Norwood, MA, (1991)

[39] L. Brillouin, Ann. Phys. 17, 88 (1922)

[40] J. Shroeder, *Light Scattering of Glass*, p.212 in"*Treatise on Materials Science and Technology*, Vol.12 (1977), by M. Tomozawa, R. H. Doremus

[41] L. Landau and G. Plaszek, Z. Phys. Sovjetunion 5, 172 (1922)

[42] J. Frenkel, *Kinetic Theory of Liquids,* Dover Publications, NY, (1955)

[43] M. Leontovich, Z. Phys. 72, 247, (1931)

[44] H.Z. Cummins and Schoen P.E. (1972), *"Linear Scattering from Thermal Fluctuations"* in Arecchi and Schultz-DuBois (Eds.), Laser Handbook, Vol.2 (p. 1029-1075), North-Holland Publ. Co., Amsterdam.

[45] P. Benassi, et al., Phys. Rev. B, 48(9), 5987-5996, (1993)

[46] G.H. Gangwere, PhD Thesis, Oklahoma Stat University, (1990)

[47] A.I. Ritus, Tr. Fiz. Inst. Akad. Nauk SSSR, 137, 3 (1982)

[48] I.A. Grishin et al., Sov. J. Quantum Electron., 17(2), 229-230, (1987)

[49] H. R. Carleton, Amorphous Materials, eds. R. W. Douglas and Bryan Ellis (Wiley, Interscience, New York, p.103, (1972); Bull. Am. Phys. Soc. 14, 74 (GF-15), (1969)

[50] K. Matusita *et al*, J. Non-Cryst. Solids, 112, 341-346, (1989)

[51] Sir C.V. Raman and K.S. Krishnan, Ind. J. Phys., 2, 287, (1928a)

[52] G. Placzek, in E. Narx, Ed, Handbook der radiology, 6(2), p.209, (1934)

[53] R. Shuker and R.W. Gammon, Phys. Rev. Lett., 25, 222, (1970)

[54] F. L. Galeener and P.N. Sen, Phys. Rev., B17, 1928, (1978)

[55] E. Lippmaa *et al.,* J. Am. Chem. Soc., 102, 4889, (1980)

[56] P.J. Hore, *Nuclear Magnetic Resonance*, Oxford University Press, (1995)

Reviews in Mineralogy, Vol. 32, Mineral. Soc. America, Washington DC, (1995)

[57] G. Engelhardt and D. Michel *"High – resolution solid – state NMR of silicates and zeolites"*, John Wiley & Sons, (1987)

[58] J. J. Fitzerald, *"Solid – State NMR Spectroscopy of Inorganic materials"*, American Chemical Society, Washington DC, 1999

[59] W.W. Shao *"NMR studies of amorphous silicon and aluminosilicate glass"*, PhD Thesis, Iowa State University

[60] J. F. Stebbins *et al.*, *"Structure, dynamics and properties of silicate melts"*, (1995)

[61] M. D. Bruch, *NMR Spectrosopy Techniques*, Marcel Dekker Inc., NY, 1996

[62] Gan Fuxi, *"Optical and Spectroscopic properties of glass"*, Springer-Verlag, Shanghai, 1992

[63] J. E. Shelby, J. Appl. Phys., 66(5), 1947-1950, (1989)

[64] D. M. Zirl, S. H. Garofalini, J. Am. Ceram. Soc., 73 (10), 2848 – 2856, (1990)

[65] J.E. Shelby *et al.*, Phys. Chem. Glasses, 33, 93-98, (1992)

[66] K. J. Kao, "Structural Chemistry of Glasses", Elsevier Science Ltd, NY, (2002)

[67] A. Elshafie, Mater. Chem Phys., 51, 182, (1997)

[68] B. Bridge, Phys. Stat. Sol (a), 77, 655, (1983)

[69] J.K. Schroeder, *J. Non-Cryst. Solids*, 40, 549-566, (1980)

[70] Y. Vaills *et al.*, Solid State Communications, 87(12), 1097-1100, (1993)

[71] J. Schroeder, *et al*, Materials Science Forum, 19-20, 653-670, (1987)

[72] L-G Hwa, J. Raman Spectroscopy, 29, 269-272, (1998)

[73] E.G. Behrens, *et al*, Phys. Rev. B, 39(9), 6076, (1989)

[74] White W. B. in "Glasses for Electronic Applications", (1990)

[75] Lee M. *et al.*, APS Meeting Bulletin, vol.2, p. 1662, (1999)

[76] R.A. Condrate, Sr, Key Engineering Materials, 94-95, 209-232, (1994)

[77] A.J.G. Ellison, P.C. Hess, J. Geophys. Res. 95 (B10), 15717, (1990)

[78] T. Schaller, *et al*, J. Non-Cryst. Solids, 243, 146 (1999)

[79] D.M. Krol and B.M.J. Smets, Phys. Chem. Glasses, 25 (5), 119-125, (1984)

[80] B. L. Sheriff, H. D. Grundy, Nature 332, 819, (1988)

[81] G. Engelhardt *et al.*, Phys Chem Glasses, 26, 157, (1985)

[82] R. J. Kirkpatrick, *et al.*, Am. Mineral., 70, 106, (1985)

[83] J. B. Murdock et al., Am. Mineralogist, 70, 332, (1985)

[84] S.K. Lee, J. F. Stebbins, Geochim. Cosmochim. Acta, 67(9), 1699-1709, (2003)

[85] R. Oestrike, *et al.*, Geochimica et Cosmochimica Acta, 51, 2199, (1987)

[86] X. Xue, J.F. Stebbins, Phys chem. Minerals, 20, 297-307, (1993)

[87] J.R. Sandercock, *"Operator Manual for Tandem* Interferometer", Sept. (1993)

[88] J. M. Vaughan, *"Fabri-Perot Interferometers"*, p.214

[89] H. Mueller, Proc. Rp. Soc. (London) 166A, (1938), 425

[90]: It has been shown (see for example [19]) that weak excitation of Eu^{3+} ions still occurs due to phonon-assisted energy transfer and/or the breadth of the inhomogeneously broadened absorption band

[91] J. Haase, *et al.*, J. Phys. Chem. 95, p. 6996-7002, (1991)

[92] J. Haase and E. Oldfield J. Mag. Reson. A 101, 30-40, (1993)

[93] P.P. Man, *et al*, Chemical Physics Letters, 151, 143-150, (1988)

[94] K.D. Schmitt, *et al*, Zeolites 14, p. 89-100, (1994)

[95] S.M. Mian, PhD Dissertation, Oklahoma State Unievrsity, (1996)

[96] A. Makishima *et al.*, J. Am. Ceram. Soc., 65, C210, (1982)

[97] E. Husson, *et al*, Studies in Physical and Theoretical Chemistry, 71, 395, (1990).

[98] P.H. Gaskell, *et al*, *Nature*, **350**, 675, (1988)

[99] J. Farnan, et al, *Nature*, **358**, 31, (1992)

[100] D.R. Lide, ed., *Handbook of Chemistry and Physics*, 75ed, (1991)

[101] J.E. Shelby, "Introduction to Glass Science and Technology", Royal Society of Chemistry, p.169, (1997)

[102] J. E. Shelby, Key Engineering Materials, 94-95, p. 43-80, (1994)

[103] Z-D. Pan, and J.P. Wicksted, *Opt. Eng.*, 31, 116, (1992)

[104] J. Schroeder, *et al*, Optical Engineering, 24(4), 697-703, (1985)

[105] S. Tanabe, *J. Non-Cryst. Solids,* 259, 1-9, (1999)

[106] B.O. Mysen, *et al.*, Amer. Mineral., 70, 88, (1985),

[107] Ph. Colomban, J. Mater. Sc., 24, p.3002-3010, (1989)

[108] A. Navrotsky, K.L. *et al.*, Physics and Chemistry of Minerals, 11, p. 284-298

[109] R.A. Murray *et al*, J. Non-Cryst. Solids, 94, 133, (1987)

[110] P.P. McMillan, Am. Mineralogist, 69, 622, (1984)

[111] S. Todoroki, J. Ceram. Soc. Japan, 101(9), 1065-1067, (1993)

[112] H. Kozuka, *et al*, J. Mater. Sci. Lett., 6, p.267-270, (1987)

[113] S.A Brawer. and W.B. White, J. Chem Phys., 63(6), p.2421-2432, (1975).

[114] J. D. Kubicki and D. Sykes, Phys. Chem. Minerals, 19, p.381-391, (1993)

[115] D. Sykes and J.D. Kubicki., Amer. Mineral., 81, 265 – 272, (1996)

[116] F. Durville *et al*, J. Lumin. 36, p.221-229, (1987)

[117] V.K. Tikhomirov *et al*, J. Non-Cryst. Solids, 256 & 257, p.89-94, (1999).

[118] T. Schaller *et al*, J. Non-Cryst. Soilds, 243, p.146-157, (1999)

[119] J. B. Murdock, *et al.*, Am. Mineralogist, 70, 332, (1985)

[120] O. Glock, *et al.*, J. Non-Cryst. Solids, 232-234, p.113 – 118, (1998)

[121] J. Mahler, A. Sebald, Solid State Nuclear Resonance, **5**, p. 63-78, (1995)

[122] T. Maekaua, *et al.*, J. Non-Cryst. Solids, **127**, 53-64, (1991)

[123] S. Shen, J.F. Stebbins, J. Non-Cryst. Solids, 188, 54, (1995)

[124] B.O. Mysen and D. Virgo, Carnegie Institution Washington Year Book, 82, p. 321-325, (1983)

[125] Kushiro, Chapter 3 in: Physics of Magmatic Processes, (edited by R. B. Hargraves). Princeton University Press, p.585. (1980)

[126] C.H. Hsieh, *et al.*, J. Appl. Phys., 80 (3), 1704 – 1712, (1996),

[127] S. Tanabe, et al., *J. Non-Cryst. Solids.*, 113, 178, (1989)

[128] C. H. Hsieh et al., J. Appl. Phys., 80(3), 1704-1712, (1996)

[129] P. McMillan, *et al.*, Geochim. Cosmochim. Acta 46 (2), 2021-2037, (1982),

[130] V.N. Bykov, *et al.*, Geochemistry International, Vol. 34, 4, 296-302, (1996)

[131] R.A. Barrio *et al.*, Phys. Rev. B, 48 (21), p.15672-15689, (1993)

[132] E.R. Lippencott *et al.*, J. Chem. Phys. 20, 536, (1952)

[133] J. Jin *et al.*, J. Non-Cryst. Solids, 262, p.183-190, (2000)

[134] R. Dupree, *et al*, J. Non-Cryst. Solids, 68, 399, (1984).

[135] J. E. Shelby, Key Engineering Materials, 94-95, p. 1-42, (1994)

[136] G. Engelhardt and D. Michel, "High Resolution Solid-State NMR of Silicates and Zeolites", 1987, John Wiley & Sons, p.202-203

[137] Lippmaa E., *et al.*, J. Amer. Chem. Soc., **103**, 4992-4996, (1981)

[138] F. Domine and B. Piriou, Am. Mineral. **71**, 38, (1986)

[139] B. N. Roy, A. Navrotsky, J. Am. Ceram. Soc., **67**, 606, (1984).

[140] B.O. Mysen, *et al.*, Am. Mineral. **65**, 690, (1980)

[141] G.S. Dixon, Phys. Rev. B, 49(1), 257-264, (1994)

[142] C. A. Fyfe, *et al.*, J. Phys. Chem., 86, 1247-1250, (1982)

[143] E. Lippmaa *et al.*, J. Am. Chem. Soc., 108, 1730-1735, (1986)

[144] G.S. Henderson, Amer. Mineral., 70, 946-960, (1985)

[145] A.Y. Hamad, PhD Thesis, Oklahoma State University, (1996)

[146] Z.Utegulov, M. Eastman, G-Q. Shen, S. Prabakar, K. Mueller, J.P. Wicksted, APS Meeting, Austin, TX, March 3-5, (2003)

[147] G. Shen, Z. Utegulov, J. Wicksted, S. Mian, APS March 2001 Meeting, , Seattle, WA, Vol. 46, No.1, Part I, p.104, March 12-16, (2001)

[148] G. Shen, Z. Utegulov, J. Wicksted and A. Rahman, APS Meeting, Seattle, WA, Vol. 46, No.1, Part I, p.326, March 12-16, (2001)

[149] Z.N. Utegulov, M.A. Eastman, J.P.Wicksted, Annual OSU Research Symposium, April, (2000)

[150] Z.N. Utegulov, M.A. Eastman, G. Shen, A.Y. Hamad, J.P. Wicksted, G.S. Dixon, Glass and Optical Materials and Devices Division Meeting, American Ceramic Society, Corning , NY, October 1-4, (2000)

[151] Z.N. Utegulov., A.Y. Hamad, J.P. Wicksted, G.S. Dixon and J.J. Martin, APS Meeting, , Atlanta, Georgia, Vol. 44, No. 1, Part II, p.1661, March 20-26, 1999

[152] H. Lee, D. Psaltis, Optics Letters, 12(7), 459-61, (1987)

[153] V. V. Shepelevich, Proc. SPIE, 1983, 614-15, (1993)

VITA 2

Zhandos Nurpeisovich Utegulov

Candidate for the Degree of

Doctor of Philosophy

Thesis: STRUCTURAL CHARACTERIZATION OF RARE-EARTH DOPED
SODA MAGNESIA ALUMINA SILICA GLASSES FOR HOLOGRAPHIC
STRORAGE: BRILLOUIN, RAMAN AND NMR SPECTROSCOPY
STUDIES

Major Field: Physics

Biographical:

  Personal Data: Born in Almaty, Kazakhstan, On January 16, 1973, the son of Nurpeis
    Utegulov and Iren Muldagalieva.

  Education: Graduated from National School of Physics and Mathematics, Almaty,
    Kazakhstan, in June 1990; received Bachelor degree with honors in Physics
    in June 1996 from Kazakh National University, Almaty, Kazakhstan and
    Master of Science in Photonics in May 1999 from Oklahoma State
    University, Stillwater, Oklahoma. Completed the requirements for PhD
    degree with a major in Physics at Oklahoma State University in August,
    2003.

  Professional Experience: Research Engineer, Department of Physics, Kazakh
    State National University, Almaty, Kazakhstan, 1994-1996; Teaching
    Assistant, Department of Physics, Oklahoma State University, 1996-1997;
    Graduate Research Assistant, Center for Laser and Photonics Research,
    Oklahoma State University, 1997 to present.

  Professional Memberships: American Physical Society, Optical Society of
    America and American Ceramic Society